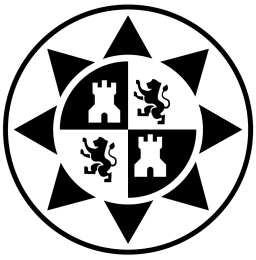

Universidad Politécnica de Cartagena

Departamento de Tecnologías de la Información y las Comunicaciones

New Configurations and Design Techniques for Multimode Microwave Filters for Use in Industrial Microwave Ovens and Other Devices

Francisco Javier Clemente Fernández

Supervisors:

Prof. Juan Monzó Cabrera

Dr. Juan Luis Pedreño Molina

Cartagena, Spain, 2013

Universidad Politécnica de Cartagena

DT-17

CONFORMIDAD DE DEPÓSITO DE TESIS DOCTORAL POR LA COMISIÓN ACADÉMICA DEL PROGRAMA

D. Francisco Alhama López, Presidente de la Comisión Académica del Programa de Doctorado de Tecnologías Industriales

INFORMA:

Que la Tesis Doctoral titulada, "New Configurations and Design Techniques for Multimode Microwave Filters for Use in Industrial Microwave Ovens and Other Devices", ha sido realizada por D. Francisco Javier Clemente Fernández, bajo la dirección y supervisión del Dr. Juan Monzó Cabrera y el Dr. Juan Luis Pedreño Molina.

En reunión de la Comisión Académica de fecha 10 de Junio - 2013 , visto que la mencionada tesis doctoral tiene acreditados los indicios de calidad, requeridos para el depósito de tesis doctorales, regulados en el artículo 32 del Reglamento de Estudios Oficiales de Máster y Doctorado de la UPCT, y la autorización del Director de la misma, se acordó dar la conformidad para que a dicha tesis le sea autorizado, por la Comisión de Doctorado, su depósito.

La Rama de conocimiento por la que esta tesis ha sido desarrollada es:

- ☐ Ciencias
- ☐ Ciencias Sociales y Jurídicas
- ✓ Ingeniería y Arquitectura

En Cartagena, a 17 de Junio de 2013

EL PRESIDENTE DE LA COMISIÓN ACADÉMICA DEL PROGRAMA

Fdo: D. Francisco Alhama López

COMISIÓN DE DOCTORADO

Universidad Politécnica de Cartagena

DT-16

CONFORMIDAD DE SOLICITUD DEAUTORIZACIÓN DE DEPÓSITO DE TESIS DOCTORAL POR LOS DIRECTORES DE LA TESIS

D. Juan Monzó Cabrera, Director y D. Juan Luis Pedreño Molina, Codirector de la Tesis doctoral "New Configurations and Design Techniques for Multimode Microwave Filters for Use in Industrial Microwave Ovens and Other Devices"

INFORMAN:

Que la referida Tesis Doctoral, ha sido realizada por D. Francisco Javier Clemente Fernández, dando mi conformidad para que sea presentada ante la Comisión de Doctorado, para ser autorizado su depósito.

La rama de conocimiento por la que esta tesis ha sido desarrollada es:

- ☐ Ciencias
- ☐ Ciencias Sociales y Jurídicas
- ✓ Ingeniería y Arquitectura

En Cartagena, a 17 de Junio de 2013

EL DIRECTOR DE LA TESIS

[redacted]

Fdo.: D. Juan Monzó Cabrera

EL CODIRECTOR DE LA TESIS

[redacted]

Fdo.: D. Juan Luis Pedreño Molina

COMISIÓN DE DOCTORADO

To my parents, for their endless love, support and encouragement.

To my family, especially those who are not with us.

To my friends, for being always there for me.

Contents

List of Figures

Acknowledgements

First and foremost, I have to thank my parents for their love and support throughout my life. Thank you for giving me strength to reach for the stars and chase my dreams. My sister and rest of beloved family deserve my wholehearted thanks as well. And the most special thanks go to my grandfathers. You are not with me right now, but I can feel you everyday. I am certain that, wherever you are, you are proud of me.

I would like to sincerely thank my supervisors, Juan and Juan Luis, for his guidance and support throught this study, and especially for their confidence in me. Also a big thank you to the rest of the research group, and all the people in the university that I have had the pleasure of sharing this years with. You all have helped me to develop not only as an engineer, but also as a person. If I am sure of something is that I have learnt from the best.

I would also like to thank the Fundación Séneca, Agencia de Ciencia y Tecnología de la Región de Murcia, for their support, not only economic. Their firm commitment to research is very much appreciated these days. The Séneca predoctoral fellowship with reference 12425/FPI/09 has allowed me to successfully complete this research.

To all the staff in the National Centre for Industrial Microwave Processing in general, and to Paula and Prof. Kingman in particular, thank you for your warm welcome, hospitality and advice. My stay there may have been short, but the experience has been invaluable. Thank you.

And last but not least, to all my friends, thank you for your understanding and encouragement in my many, many moments of crisis. Thank you for not letting me give up. Something that I have learnt in the last few years is that people come and go, but you always stay. Sometimes people come into your life and you know right away that they were meant to be there, to serve some sort of purpose, teach you a lesson, or to help you figure out who you are or who you want to become. You never know who these people may be but when you lock eyes with them, you know at that very moment they will affect your life in some profound way. I cannot list all your names here, but you know who you are. And that is enough for me.

This thesis is only the beginning of my journey.

Francisco Javier Clemente Fernández
June 2013

Abstract

Microwave energy is extensively used in many industrial, scientific and medical applications, which frequently require the participation of human beings in direct contact with microwave equipment. Specifically, industrial microwave ovens often employ open-ended waveguide ports in order to allow a continuous flow of the material to be processed. For this reason, safety issues become a main concern in such systems to prevent possible dangerous effects on human tissues due to microwave energy leakage.

Some alternatives to deal with this leakage problem have been proposed in technical literature. One of the most effective choices is based on corrugated reactive filters which reflect back the energy escaping from the applicator. But some limitations have been found in this work for those traditional structures, particularly regarding the dielectric properties of the processed material.

The present thesis addresses the goal of improving these reactive filters when the oven requires a continuous-flow of the material to be processed. In order to do that, new structures are proposed which solve the inconveniences that traditional filters show, along with the use of optimization algorithms that reduce the design time.

Additionally, some innovative calibration and characterization techniques are proposed and applied to waveguide devices.

Keywords: bandstop filter, genetic algorithms, inverse problems, microwave heating, microwave sensor, self-configurable, S-parameters, waveguide transitions

Resumen

La energía de microondas se emplea habitualmente en muchas aplicaciones industriales, científicas y médicas, las cuales requieren frecuentemente la participación de personas en contacto directo con los equipos de microondas. Específicamente, los hornos industriales de microondas suelen emplear puertos abiertos en guía de onda para permitir un flujo continuo del material a procesar. Por esta razón, las cuestiones de seguridad son un aspecto primordial en estos sistemas, con el fin de evitar posibles efectos peligrosos en tejidos humanos debidos a fugas de energía de microondas.

Varias alternativas para lidiar con este problema se han propuesto en la literatura técnica. Una de las elecciones más efectivas está basada en filtros corrugados reactivos, los cuales reflejan hacia atrás la energía que intenta escapar del aplicador. Pero en esta tesis se han encontrado algunas limitaciones de estas estructuras, particularmente en lo que se refiere a las propiedades dieléctricas del material procesado.

La presente tesis aborda el objetivo de mejorar estos filtros reactivos cuando el horno requiere un flujo continuo de material. Para ello, se proponen nuevas estructuras que solucionan los inconvenientes que presentan los filtros tradicionales, así como algoritmos de optimización que reducen el tiempo de diseño.

Adicionalmente, se proponen nuevas técnicas de calibración y caracterización aplicadas a dispositivos en guía de onda.

Palabras clave: filtro elimina-banda, algoritmos genéticos, problemas inversos, calentamiento por microondas, sensor de microondas, auto-configurable, parámetros S, transiciones en guía de onda

1 Introduction and scope

1.1 Background and motivation

Safety issues in industrial ovens must be seriously taken into account since they can cause work-related accidents with serious consequences. In particular, when we are dealing with industrial microwave ovens, apart from the regular mechanical safety issues, the possible radiated energy must be considered.

In order to prevent these energy leakage, which can inflict blindness, serious burns and other consequences related to the excessive heating of the human tissues, and keep it below the levels determined by the corresponding regulations [1], waveguide bandstop filters based on corrugated or doubly corrugated structures are usually employed [2 4].

The main problems that arise in the design of such filters are, among others:

- These filters are multimode waveguide structures, hence all the propagating modes must be properly attenuated. This is an important difference with conventional communication filters that deal with just one propagating mode.
- In general, the processed samples do not have canonical shapes. Therefore, numerical methods need to be employed to obtain a solution.
- This kind of filters are electrically large compared to the wavelength. This fact implies long simulation times, so the need of efficient optimization schemes is mandatory.
- The filter needs to be specifically designed for each processed material, since both the electric permittivity and the shape of the sample affect the behaviour of the filter. In this way, ad hoc designs need to be developed for each kind of material.
- Input and output filters need to be considered separately since the material may experience important structural changes when passing through the oven, therefore changing its dielectric properties.
- The filter has to work properly both with and without the sample. If not, additional concatenated filters may be needed to deal with the unloaded scenario.

Waveguide filter design has been widely studied over the years [5 10]. In general, these studies are related to communications bandpass filters dealing with the funda-

mental mode. There are different structures that are employed as waveguide filters, being the most commonly used:

- Stubs [2]: short-circuited waveguides with $\lambda_g/4$ length. They are only able to deal with TE modes and they have a very narrow bandwidth, making them very sensitive to changes in the frequency of the magnetrons.
- Cavity filters [5 7]: they employ irises to make different cavities in the waveguide, allowing just one mode to resonate. They show high quality factors, although they are oriented to monomode applications.
- Corrugated filters [2 4]: this kind of filters make use of discontinuities (corrugations), usually rectangular ones, in the transverse section of the waveguide and also in the direction of the propagation. The structures found in the literature are usually monomode filters [3, 4] employed either with sheet materials or with no material, which do not model its behaviour in actual working conditions where there are conveyor belts or samples with non-negligible thickness.
- Filters that combine planar circuits and waveguides [8, 9]: in this case waveguides are combined with other technologies such as microstrip or coplanar circuits. This kind of filters are useless for our purpose since they cannot stand high power levels.

With regard to reconfigurable filters, only one patent has been found in which the dimensions of a cavity filter are changed by using motors in order to change its resonance frequency and, therefore, its passband [10].

From this literature review one can draw the following conclusions:

- There are few works [2 4] that study in a rigorous manner the behaviour of waveguide bandstop filters for use in microwave ovens.
- The effect of the geometry of the filter or the permittivity of the sample on the performance of the filter has not been studied so far.
- Although an example of reconfigurable filter has been found [10], it only modifies the cavity dimensions in order to change the resonance frequency. In this thesis it is proposed a new automated corrugated filter that allows a full self-configuration and control of the filter for any possible material.

1.2 Scope of the thesis

The main objective of this thesis is improving the design and performance of the input and output waveguide bandstop filters for industrial microwave ovens when they are required to work with a continuous flow of the processed material. In order to achieve this, new structures and optimization algorithms are studied. In particular, the following objectives are proposed:

- Assessment of conventional techniques: limitations and possible solutions.

- New structures of open waveguide filters combining irises and corrugations.
- Evaluation of different optimization schemes.
- Development of an experimental platform that allows us to reduce the design time and simultaneously validate such design for a fast implementation of the industrial process.
- Applications of bandstop filters: reduction of the crosscoupling and separation into hot and cold compartments in a microwave-heating cavity.

At the same time, some innovative calibration and characterization techniques are proposed and applied to waveguide devices. In particular, the following tasks are carried out:

- Characterization of coaxial-to-waveguide transitions, which are involved in waveguide measurements.
- Simultaneous characterization of coaxial-to-waveguide transitions and a device under test.
- Modelling of printed circuit boards inside a metallic enclosure.

1.3 Organization of the thesis

The following chapters of this manuscript describe the research that has been undertaken to reach the aforementioned goals. The chapters are presented as follows:

- Chapter 2: The first part of the manuscript presents the theoretical background needed for a full understanding of this research. An overview of the simulation and optimization techniques, together with a full description of the coaxial-to-waveguide transitions and bandstop filters employed throughout this thesis are described. The methods related to the analysis and study of this microwave devices are presented as well.
- Chapter 3: Here, all the simulation and measurement scenarios are explained. Firstly, the measurements involved in the characterization of the coaxial-to-waveguide transitions are properly described, along with its applications to the characterization of a device under test and the modelling of printed circuit boards. Then, the simulation and measurements employed in the assessment of traditional corrugated filters are presented, along with some applications. Additionally, a new self-configurable multimode filter, which is the main contribution of this thesis, is also introduced in this chapter.
- Chapter 4: In this chapter both traditional and new waveguide bandstop filters for use in industrial microwave-heating ovens are assessed. Firstly, the limitations of traditional reactive filters are stated. Additionally, some alternatives based on resistive filters are also evaluated. Then, a new proposed filter based

on irises and metallic posts is properly analyzed and validated. Several novel applications of bandstop filters, such as the reduction of the crosscoupling or the separation into hot and cold compartments in a heating cavity, are also studied next. Finally, the results for the new self-configurable multimode filter based on irisis an automatically tunable posts are presented and properly validated.

- Chapter 5: Results regarding the characterization of the coaxial-to-waveguide transitions and its applications are presented in this chapter. Firstly, the characterization of the WR-340 coaxial-to-waveguide transitions is shown and results are compared to different calibration algorithms. Secondly, the results corresponding to the simultaneous evaluation of the transitions and a device under test are presented. Finally, obtained results when applying the proposed technique to the modelling of printed circuit boards inside metallic enclosures are obtained.
- Chapter 6: Finally, conclusions obtained through this thesis are emphasized, including some guidelines for future research lines. A list of published works directly related to this thesis is also given.

Bibliography

[1] IEEE Standard for Safety Levels With Respect to Human Exposure to Radio Frequency Electromagnetic Fields, 3 kHz to 300 GHz, IEEE Std C95.1-2005 (Revision of IEEE Std C95.1-1991).

[2] A. C. Metaxas and R. J. Meredith, Industrial Microwave Heating. Stevenage, U.K.: Peregrinus, 1988.

[3] A. L. Vankoughnett and J. G. Dunn, "Doubly corrugated chokes for microwave heating systems", J. Microwave Power, vol. 8, no. 1, pp. 101 110, Jan. 1973.

[4] P. Soto, V. E. Boria, J. M. Catalá-Civera, N. Chouaib, M. Guglielmi and B. Gimeno, "Analysis, design, and experimental verification of microwave filters for safety issues in open-ended waveguide systems", IEEE Trans. Microw. Theory Tech., vol. 48, no. 11, pp. 2133-2140, Nov. 2010.

[5] A. E. Williams, "A four-cavity elliptic waveguide filter", IEEE Trans. on Microw. Theory Tech., vol. 18, no. 12, pp. 1109-1114, Dec. 1970.

[6] B.L. Blachier and A.R. Champeau, "Plural cavity bandpass filter", U. S. Patent 3697898, Oct. 10, 1972.

[7] H.W. Flieger, "High power waveguide filter", U.S. Patent 4260967, Apr. 7, 1981.

[8] M. Ito, K. Maruhashi, K. Ikuina, T. Hashiguchi, S. Iwanaga and K. Ohata, "A 60-GHz-band planar dielectric waveguide filter for flip-chip modules", IEEE Trans. Microw. Theory Tech., vol. 49, no. 12, pp. 2431-2436, Dec. 2001.

[9] D. Deslandes and W. Ke, "Single-substrate integration technique of planar circuits and waveguide filters", IEEE Trans. Microw. Theory Tech., vol. 51, no. 2, pp. 593-596, Feb. 2003.

[10] E. S. Fayeski and B. W. Carlson, "Remotely adjustable bandpass filter", U. S. Patent 6898419, May 25, 2005.

2 Theoretical background

2.1 Overview

In this chapter, the global framework of the thesis is presented, with an emphasis on waveguide bandstop filters. Theoretical aspects such as the scattering parameters and the simulation and optimization techniques are presented, along with more specific issues regarding coaxial-to-waveguide transitions and waveguide bandstop filters and its applications.

2.2 Scattering parameters

A practical problem exists when trying to measure voltages and currents at microwave frequencies in order to obtain the impedance or admittance matrices of a microwave circuit. The directly measurable quantities are the amplitudes and phase angles of the waves reflected, or scattered, from a junction relative to the incident-wave amplitudes and phase angles. The scattered-wave amplitudes are linearly related to the incident-wave amplitudes. The matrix describing this linear relationship is called the scattering matrix [1].

Consider the N-port junction of Fig. 2.1. If a wave with an associated equivalent voltage V_1^+ is incident on the junction at terminal plane t_1, a reflected wave $S_{11}V_1^+ = V_1^-$ will be produced in line 1, where S_{11} is the reflection coefficient for line 1. Waves will also be transmitted, or scattered, out of the other junctions and will have amplitudes proportional to V_1^+. These amplitudes can be expressed as $V_1^- = S_{n1}V_1^+$, $n = 2, 3, \ldots, N$, where S_{n1} is a transmission coefficient on line n from line 1. When waves are incident in all lines, the scattered wave in each line has contributions arising from all the incident waves. Thus, in general, we can write

$$\begin{bmatrix} V_1^- \\ V_2^- \\ \ldots \\ V_N^- \end{bmatrix} = \begin{bmatrix} S_{11} & S_{12} & S_{13} & \ldots & S_{1N} \\ S_{21} & S_{22} & S_{23} & \ldots & S_{2N} \\ \ldots & \ldots & \ldots & \ldots & \ldots \\ S_{N1} & S_{N2} & S_{N3} & \ldots & S_{NN} \end{bmatrix} \begin{bmatrix} V_1^+ \\ V_2^+ \\ \ldots \\ V_N^+ \end{bmatrix} \tag{2.1}$$

$$\left[V^-\right] = [S]\left[V^+\right] \tag{2.2}$$

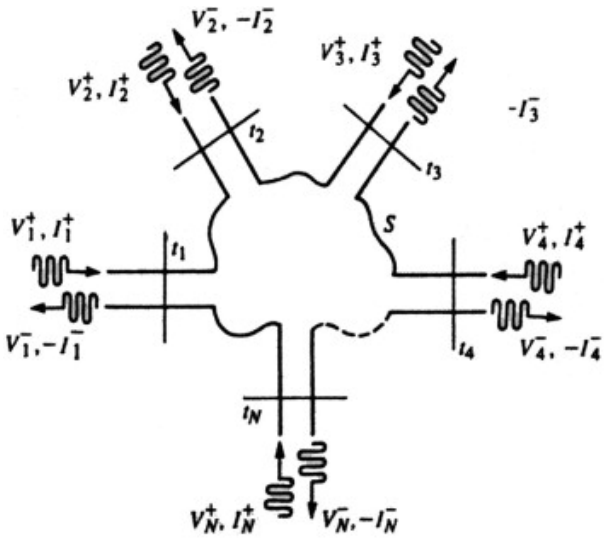

Figure 2.1: An N-port junction illustrating scattered waves.

where $[S]$ is called the scattering matrix.

As it has been seen, in the classic theory the S parameters relate incident and reflected waves at considered ports. For multimode microwave networks such as the ones employed in this thesis, the generalized scattering matrix (GSM) representation is widely used [2]. In the GSM, the S parameters express the ratio between coefficients of the modal expansion, and therefore this ratio will depend on the basis functions used [2].

In general, the GSM of a multimode microwave filter has the following form:

$$[S] = \begin{bmatrix} S_{11}^{11} & S_{11}^{12} & \dots & S_{11}^{1M} & S_{12}^{11} & S_{12}^{12} & \dots & S_{12}^{1M} \\ S_{11}^{21} & S_{11}^{22} & \dots & S_{11}^{2M} & S_{12}^{21} & S_{12}^{22} & \dots & S_{12}^{2M} \\ \dots & \dots & \dots & \dots & \dots & \dots & \dots & \dots \\ S_{11}^{M1} & S_{11}^{M2} & \dots & S_{11}^{MM} & S_{12}^{M1} & S_{12}^{M2} & \dots & S_{12}^{MM} \\ S_{21}^{11} & S_{21}^{12} & \dots & S_{21}^{1M} & S_{22}^{11} & S_{22}^{12} & \dots & S_{22}^{1M} \\ S_{21}^{21} & S_{21}^{22} & \dots & S_{21}^{2M} & S_{22}^{21} & S_{22}^{22} & \dots & S_{22}^{2M} \\ \dots & \dots & \dots & \dots & \dots & \dots & \dots & \dots \\ S_{21}^{M1} & S_{21}^{M2} & \dots & S_{21}^{MM} & S_{22}^{M1} & S_{22}^{M2} & \dots & S_{22}^{MM} \end{bmatrix} = \begin{bmatrix} S_{11} & S_{12} \\ S_{21} & S_{22} \end{bmatrix} \tag{2.3}$$

where S_{ij}^{lp} represents the generalized scattering parameter when p-th mode is excited at port j and mode l-th is measured at port i, and M is the number of propagating modes.

As regards the waveguide bandstop filters studied in this thesis, the scattering parameters of interest are the transmission ones, S_{21}^{lp}, which will determine the attenuation of the filter for each propagating mode.

2.3 The simulation method: the finite integration technique

Throughout this thesis, the 3D EM simulation tool CST STUDIO SUITE™[1] has been employed to perform all the required simulations.

CST STUDIO SUITE™ is a general-purpose electromagnetic simulator based on the Finite Integration Technique (FIT), first proposed by Weiland in 1977 [3] and enhanced continually over the years. The finite integration technique is a spatial discretization scheme to numerically solve electromagnetic field problems in time and frequency domain which preserves basic topological properties of the continuous equations such as conservation of charge and energy. This numerical method provides a universal spatial discretization scheme applicable to various electromagnetic problems ranging from static field calculations to high frequency applications in time or frequency domain.

The basic idea of this approach is to apply the Maxwell equations in integral form to a set of staggered grids, unlike most numerical methods that discretize the differential form:

$$\oint_{\partial A} \mathbf{E} \cdot d\mathbf{s} = -\int_{A} \frac{\partial \mathbf{B}}{\partial t} \cdot \partial \mathbf{A} \tag{2.4}$$

$$\oint_{\partial A} \mathbf{H} \cdot d\mathbf{s} = \int_{A} \left(\frac{\partial \mathbf{D}}{\partial t} + \mathbf{J} \right) \cdot \partial \mathbf{A} \tag{2.5}$$

$$\oint_{\partial V} \mathbf{D} \cdot d\mathbf{A} = \int_{V} \rho \cdot dV \tag{2.6}$$

$$\oint_{\partial V} \mathbf{B} \cdot d\mathbf{A} = 0 \tag{2.7}$$

where $\mathbf{E}$ and $\mathbf{H}$ are the electric and magnetic field intensities, $\mathbf{D}$ and $\mathbf{B}$ are the electric and magnetic flux densities, ρ is the volume charge density and $\mathbf{J}$ is the electric current density.

This method stands out due to its high flexibility in geometric modeling and boundary handling as well as the incorporation of arbitrary material distributions and material properties such as anisotropy, non-linearity and dispersion. Furthermore, the use of a consistent dual orthogonal grid (e.g. Cartesian grid) in conjunction with an explicit time integration scheme (e.g. leap-frog-scheme) leads to compute and

[1] CST STUDIO SUITE and CST MICROWAVE STUDIO are trademarks or registered trademarks of CST Computer Simulation Technology AG (www.cst.com).

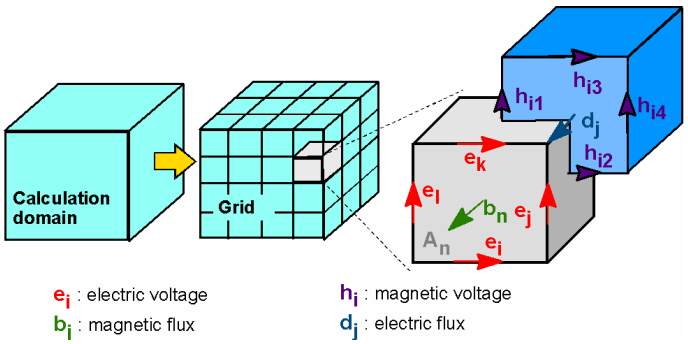

Figure 2.2: Electric and magnetic voltages and fluxes on the primary and dual grids [4].

memory-efficient algorithms, which are especially adapted for transient field analysis in radio frequency and microwave applications.

To numerically solve these equations, one must define a finite calculation domain, enclosing the considered application problem. This domain is split up into many grid cells by creating a suitable mesh. For simplicity, we will restrict the following explanations to an orthogonal hexahedral grid. Then, two meshes are set up: the primary mesh which can be visualized in CST STUDIO SUITE™ and a dual mesh which is set up orthogonally to the first one. Finally, the spatial discretization of Maxwell's equations is performed on these two orthogonal grid systems where the degrees of freedom are introduced as integral values. Referring to Fig. 2.2, the electric grid voltages **e** and magnetic facet fluxes **b** are allocated on the primary grid **G**. In addition, the dielectric facet fluxes **d** as well as the magnetic grid voltages **h** are defined on the dual grid $\tilde{\mathbf{G}}$.

Now Maxwell's equations are formulated for each of the cell facets separately as demonstrated in the following. Considering Faraday's Law in 2.4, the closed integral on the equation's left side can be rewritten as a sum of four grid voltages without introducing any supplementary errors. Consequently, the time derivative of the magnetic flux defined on the enclosed primary cell facet represents the right-hand side of the equation, as illustrated in Fig. 2.3. Repeating this procedure for all available cell facets summarizes the calculation rule in a matrix formulation, introducing the topological matrix **C** as the discrete equivalent of the analytical curl operator.

Applying this scheme to Ampère's law in 2.5 on the dual grid involves the definition of a corresponding dual discrete curl operator $\tilde{\mathbf{C}}$. Similarly the discretization of the remaining divergence equations introduces discrete divergence operators **S** and $\tilde{\mathbf{S}}$, belonging to the primary and dual grids, respectively. As previously indicated, these discrete matrix operators consist of elements '0', '1' and '-1', representing merely topological information. Finally we obtain the complete discretized set of Maxwell's Grid Equations (MGEs):

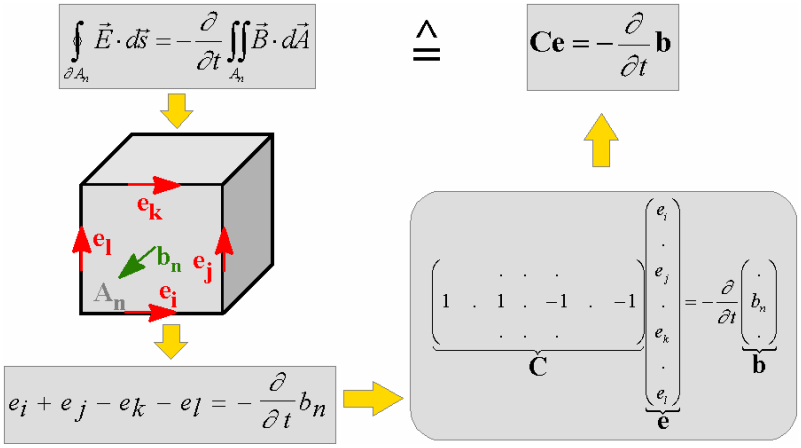

Figure 2.3: Formulation of Maxwell's equations for each of the cell facets [4].

$$\mathbf{Ce} = -\frac{d}{dt}\mathbf{b} \tag{2.8}$$

$$\tilde{\mathbf{C}}\mathbf{h} = \frac{d}{dt}\mathbf{d} + \mathbf{j} \tag{2.9}$$

$$\tilde{\mathbf{S}}\mathbf{d} = \mathbf{q} \tag{2.10}$$

$$\mathbf{Sb} = \mathbf{0} \tag{2.11}$$

where $\mathbf{j}$ denotes the current vector and $\mathbf{q}$ is a vector of space charges.

Compared to the continuous form of Maxwell's equations, the similarity between both descriptions is obvious. Once again it should be mentioned that no discretization error has yet been introduced. A remarkable feature of FIT is that important properties of the continuous gradient, curl and divergence operators are still maintained in grid space:

$$\mathbf{SC} = \tilde{\mathbf{S}}\tilde{\mathbf{C}} = \mathbf{0} \Leftrightarrow \text{div rot} \equiv 0 \tag{2.12}$$

$$\mathbf{C}\tilde{\mathbf{S}}^{\mathrm{T}} = \tilde{\mathbf{C}}\mathbf{S}^{\mathrm{T}} = \mathbf{0} \Leftrightarrow \text{rot grad} \equiv 0 \tag{2.13}$$

At this point it should be mentioned that even the spatial discretization of a numerical algorithm could cause long-term instability. However, based on the presented fundamental relations, it can be shown that the FIT formulation is not affected by such problems since the set of MGEs maintain energy and charge conservation [5]. Finally, the missing material relations introduce inevitable numerical inaccuracy due to spatial discretization. In defining the necessary relations between voltages and fluxes, their integral values have to be approximated over the grid edges and cell areas, respectively. Consequently, the resulting coefficients depend on the averaged material parameters as well as on the spatial resolution of the grid and are summarized again in correspondent matrices:

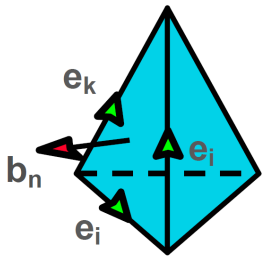

Figure 2.4: Allocation of the electric voltages and magnetic fluxes on a tetrahedral mesh cell [4].

$$\vec{D} = \varepsilon \vec{E} \Rightarrow \mathbf{d} = \mathbf{M}_\varepsilon \mathbf{e} \tag{2.14}$$

$$\vec{B} = \mu \vec{H} \Rightarrow \mathbf{b} = \mathbf{M}_\mu \mathbf{h} \tag{2.15}$$

$$\vec{J} = \sigma \vec{E} + \vec{J}_S \Rightarrow \mathbf{j} = \mathbf{M}_\sigma \mathbf{e} + \mathbf{j}_S \tag{2.16}$$

where $\mathbf{M}_\varepsilon$, $\mathbf{M}_\mu$ and $\mathbf{M}_\sigma$ are the material permittivity, permeability and conductivity matrixes, respectively.

Now all matrix equations are available to solve electromagnetic field problems on the discrete grid space. The fact that the topological and metric information is divided into different equations has important theoretical, numerical and algorithmic consequences [5]. In addition to orthogonal hexahedral grids, FIT can also be applied to more general mesh types such as topologically irregular grids (subgrids) and tetrahedral grids, respectively. Fig. 2.4 shows the allocation of the electric voltages and magnetic fluxes on a tetrahedral mesh cell. The application of FIT to these more general types of meshes can be seen as an extension to the basic method outlined above [6].

In the case of Cartesian grids, the FIT formulation can be rewritten in time domain to yield standard Finite Difference Time Domain methods (FDTD). However, classical FDTD methods are limited to staircase approximations of complex boundaries. In contrast, the Perfect Boundary Approximation® (PBA) technique [7] applied to the FIT algorithm maintains all the advantages of structured Cartesian grids while allowing accurate modeling of curved structures.

As demonstrated, the FIT formulation is a general method and therefore can be applied to all frequency ranges from DC to high frequencies.

2.3.1 Transient solver overview

Three solver types are available in CST STUDIO SUITE™ concerning high frequency electromagnetic field problems: transient, frequency domain and eigenmode solver.

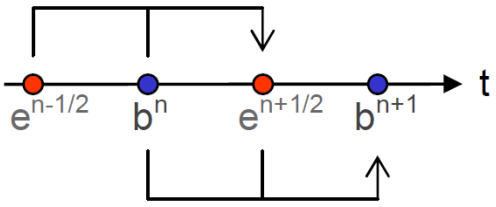

Figure 2.5: Leap-frog scheme for the calculation of the electric voltages and magnetic fluxes [4].

The CST MICROWAVE STUDIO® transient solver allows the simulation of a structure's behavior in a wide frequency range in just a single computation run. Consequently, this is an efficient solver for most driven problems, especially for devices with open boundaries or large dimensions. This is the reason why the transient solver has been chosen to solve the electromagnetic problems proposed in this thesis.

The transient solver is based on the solution of the discretized set of Maxwell's Grid Equations. Substituting the time derivatives by central differences yields explicit update formulation for the loss-free case:

$$\mathbf{e}^{n+1/2} = \mathbf{e}^{n-1/2} + \Delta t \mathbf{M}_{\varepsilon}^{-1} \left[\tilde{\mathbf{C}} \mathbf{M}_{\mu}^{-1} \mathbf{b}^{n} + \mathbf{j}_{S}^{n} \right] \tag{2.17}$$

$$\mathbf{b}^{n+1} = \mathbf{b}^{n} - \Delta t \mathbf{C} \mathbf{e}^{n+1/2} \tag{2.18}$$

where Δt is the time step and n denotes the indices for each time step.

Regarding the relations above, calculation variables are given by electric voltages and magnetic fluxes. Both types of unknowns are located alternately in time, as in the wellknown leap-frog scheme shown in Fig. 2.5.

For example, the magnetic flux at $t = (n+1)\,\Delta t$ is computed from the magnetic flux at the previous time step $t = n\Delta t$ and from the electric voltage at half a time step before, at $t = (n+1/2)\,\Delta t$.

Explicit time integration schemes are conditionally stable. The stability limit for the time step Δt is given by the Courant-Friedrichs-Levy (CFL) criterion which has to be fulfilled in every single mesh cell.

$$\Delta t \leq \frac{\sqrt{\varepsilon \mu}}{\sqrt{\left(\frac{1}{\Delta x}\right)^2 + \left(\frac{1}{\Delta y}\right)^2 + \left(\frac{1}{\Delta z}\right)^2}} \tag{2.19}$$

Here Δx, Δy and Δz define the size of a single mesh cell. The solver implemented in CST MICROWAVE STUDIO® automatically meets this criterion.

2.4 The optimization technique: genetic algorithms

The application of modern electromagnetic theory to radiation and scattering problems often either requires, or at least benefits from, the use of optimization. Electromagnetic optimization problems generally involve a large number of parameters. The parameters can be either continuous, discrete, or both, and often include constraints in allowable values. The goal of the optimization is to find a solution that represents a global maximum or minimum. In addition, the solution domain of electromagnetic optimization problems often has nondifferentiable and/or discontinuous regions, and often utilizes approximations or models of the true electromagnetic phenomena to conserve computational resources. These characteristics sorely test the capabilities of many of the traditional optimization techniques, and often require hybridization of traditional optimization methods, if these methods are to be applied at all.

Genetic Algorithms (GA) are robust, stochastic-based search methods, which can handle the common characteristics of electromagnetic optimization problems that are not readily handled by other traditional optimization methods. As an optimizer, the powerful heuristic of the GA is effective at solving complex, combinatorial and related problems. GA optimizers are particularly effective when the goal is to find an approximate global maximum in a high-dimension, multi-modal function domain, in a near-optimal manner. Consequently, they are a powerful optimization tool whose applicability to complex non-linear electromagnetic problems has been proved [8].

Along this doctoral thesis, the GA will be used solely or together with other optimization methods in order to achieve the proposed goals. Particular optimization strategies will be explained for each case.

2.5 Coaxial to waveguide transitions

Transitions are a key part of most microwave systems and circuits, making possible the interconnection between different types of transmission lines such as waveguides, coaxial, coplanar or microstrip lines, for instance. Hence, it is imperative to have a good characterization of these structures, in order to assess their performance and to provide information that can be used during the design, measurement or optimization processes. Therefore, a large number of contributions can be found in the technical literature regarding the modeling and characterization of various types of transitions, especially coaxial to microstrip [9 18] and coaxial to waveguide transitions [19 22]. Several methods of adapter characterization can be found in [23, 24] paying special attention to the study of uncertainties.

In particular, precise evaluation of coaxial to microstrip transitions is mandatory to obtain accurate measurements of microstrip integrated circuits by means of a vector network analyzer (VNA), since the quality of the measurements is strongly related to the quality of the transitions and repeatability is a critical issue [17]. In fact, many

times it is not possible to directly measure the scattering parameters of a circuit implemented in microstrip or waveguide technology since VNAs work with coaxial connectors and, therefore, their measurements always include the contributions of the necessary in-between transitions.

For instance, test fixtures use coaxial to microstrip transitions in order to measure embedded microstrip circuits. If the scattering parameters of test fixture transitions are known they can be removed from VNA measurements by the so-called de-embedding process [25, 26]. However, the measurement of transition parameters is not straightforward and they must be characterized from measurements made at the VNA reference plane when known standards are embedded in the fixture. This process is referred to as unterminating [26].

There are many possibilities for unterminating depending on the standards types and error minimization procedures. For instance open-short-load, thru-reflect-line [25, 26] standards may be used for unterminating. However, several works based on iterative approaches [26, 27] show that it is possible to use redundant standards in order to increase accuracy versus conventional calibration procedures.

Very important efforts have been made at the National Institute of Standards and Technology (NIST), Boulder, CO, in order to develop software packages for calibration and unterminating processes. For instance, MultiCal and StatistiCAL freeware software packages implement calibration algorithms based on several works such as [25 30] that performs both one-tier and two-tier de-embedding. The two-tier calibration procedure can be used to electrically characterize probe heads or other components such as coaxial-to-waveguide transitions and can handle up to 40 different standard types.

Coaxial lines to waveguide junctions have also been subject of active research in recent years, since they are used in a multitude of microwave applications. This kind of junctions can be divided into two different, though closely related, groups, namely T-junctions and coaxial line to waveguide transitions. Waveguide T-junctions are commonly used in multiplexers and diplexers [31,32] and power dividers [33], whereas transitions, which can also be viewed as a particular case of T-junctions, are used, for example, in the input and output ports of microwave cavity filters [34, 35] and in horn antennas [36].

All the above applications require extracting the scattering parameters of the electrical transitions. Thus, numerous methods and techniques have been developed using different approaches. CAD models of connectors and transitions have been used both in coaxial to microstrip [14] and coaxial-to-waveguide transitions [33]. The main problem of this approach is that full-wave electromagnetic analysis of these structures requires complex frequency-dependent calculations, even if the complexity of the structure is not high. That is why some different characterization methods based on S-parameter measurements have been presented, specifically focused on coaxial probe modeling in waveguides and cavities.

The probe-excited waveguide problem has been studied during the last fifty years.

One of the most important contributions is presented in [19], where a rigorous method to obtain the 2-port scattering matrix of a probe-excited semi-infinite waveguide is shown. This procedure is known as the three cavities moment method and makes use of three cavities and their input reflection coefficients for obtaining three linear equations with which the 2-port scattering matrix can be calculated, by impressing the incident wave in the coaxial line only. The main drawback of this method is a restriction regarding the phases of the reflection coefficient of the short-circuited waveguide sections, which must not have 360^{o} differences at a given frequency. The authors suggest using phase differences of 120^{o} and 240^{o}. Furthermore, this procedure assumes only one propagating mode and cannot compute generalized S-parameters, so an extension is presented in [21]. In that work the authors include the use of the orthogonal expansion method for modeling cylindrical posts in rectangular waveguides. Further research on the three cavities approach can be found in [22], where a coaxial line to a rectangular waveguide junction is analyzed using the five-cavity moment method in combination with network cascading techniques and an interpolation method. All these methods use waveguide short-circuit standards at different electrical lengths from the transition in order to extract its behavior versus frequency.

In this doctoral thesis we will present a new method for obtaining a precise evaluation of coaxial-to-waveguide transitions by means of inverse techniques [37]. In this case, the transition is characterized by estimating its scattering parameters and a cascade procedure is employed in order to compare simulation and measurements. The method will be explained in detail in next section.

2.5.1 Inverse technique used for the two-tier calibration algorithm

An inverse technique [38] provides the estimation of an unknown parameter by comparing the experimental response of the analysed structure to the simulation of the experimental scenario. In this study the two-port scattering matrices of two different coaxial-to-waveguide transitions are simultaneously obtained by means of an inverse procedure. A specific study of a coaxial-waveguide transition has been carried out although the proposed procedure can be readily extended to other transition types. The experimental setup considers up to three waveguide shorts and three waveguide lines with different lengths as calibrating standards placed at the end or in-between the coaxial to waveguide transitions. Therefore, this inverse procedure can be classified as a two-tier calibration problem [39]. In Fig. 2.6 a scheme of the WR-340 transitions under study is depicted. As it can be observed these transitions include several tuning screws in order to obtain good matching levels within the operating bandwidth.

The two-port scattering parameters of each coaxial-to-waveguide transition are modelled through their magnitude and phase representation. This leads to 12 differ-

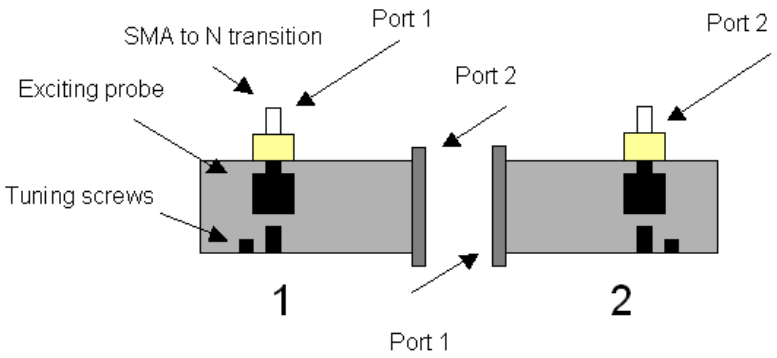

Figure 2.6: coaxial-to-waveguide transitions under study.

ent unknown real parameters when considering both transitions and the fact that $S_{12}^{tr1} = S_{21}^{tr1}$ and $S_{12}^{tr2} = S_{21}^{tr2}$ due to reciprocity. It also must be taken into account that each scattering parameter must be evaluated at different frequency values within the studied bandwidth. The S matrices for each transition are defined as follows in (2.20) and (2.21).

$$\begin{bmatrix} S_{11}^{tr1} & S_{12}^{tr1} \\ S_{21}^{tr1} & S_{22}^{tr1} \end{bmatrix} = \begin{bmatrix} Ae^{j\phi_1} & Be^{j\phi_2} \\ Be^{j\phi_2} & Ce^{j\phi_3} \end{bmatrix} \tag{2.20}$$

$$\begin{bmatrix} S_{11}^{tr2} & S_{12}^{tr2} \\ S_{21}^{tr2} & S_{22}^{tr2} \end{bmatrix} = \begin{bmatrix} De^{j\phi_4} & Ee^{j\phi_5} \\ Ee^{j\phi_5} & Fe^{j\phi_6} \end{bmatrix} \tag{2.21}$$

where $tr1$ and $tr2$ refer to each transition, A, B, C, D, E, $F \in [0, 1]$ represent the magnitude of the parameters and ϕ_1, ϕ_2, ϕ_3, ϕ_4, ϕ_5, $\phi_6 \in [-\pi, \pi]$ are their phase values. Employed coaxial-to-waveguide transitions are slightly different and the proposed method deals with their particular differences providing an accurate set of S-parameters for each one.

From a device point of view, the connection of both standards to the coaxial-to-waveguide transition can be interpreted as a cascade of devices. The defined lines are considered lossless, which is a good approximation for aluminium and short waveguide sections used in this work.

The cascade formulas for S-parameters are well known and can be found in literature [40].

The flowchart of the optimization procedure employed for the characterization of the transitions is shown in Fig. 2.7. The values of S_{ij}^{trn} ($n = 1, 2$ and $i, j = 1, 2$) are sequentially obtained for 1001 frequency points in the range under study with the help of two different optimization techniques. For the first frequency point, the initial solution is obtained with the aid of a genetic algorithms tool implemented in Matlab®. After this stage, a more accurate refinement is obtained with the aid of a

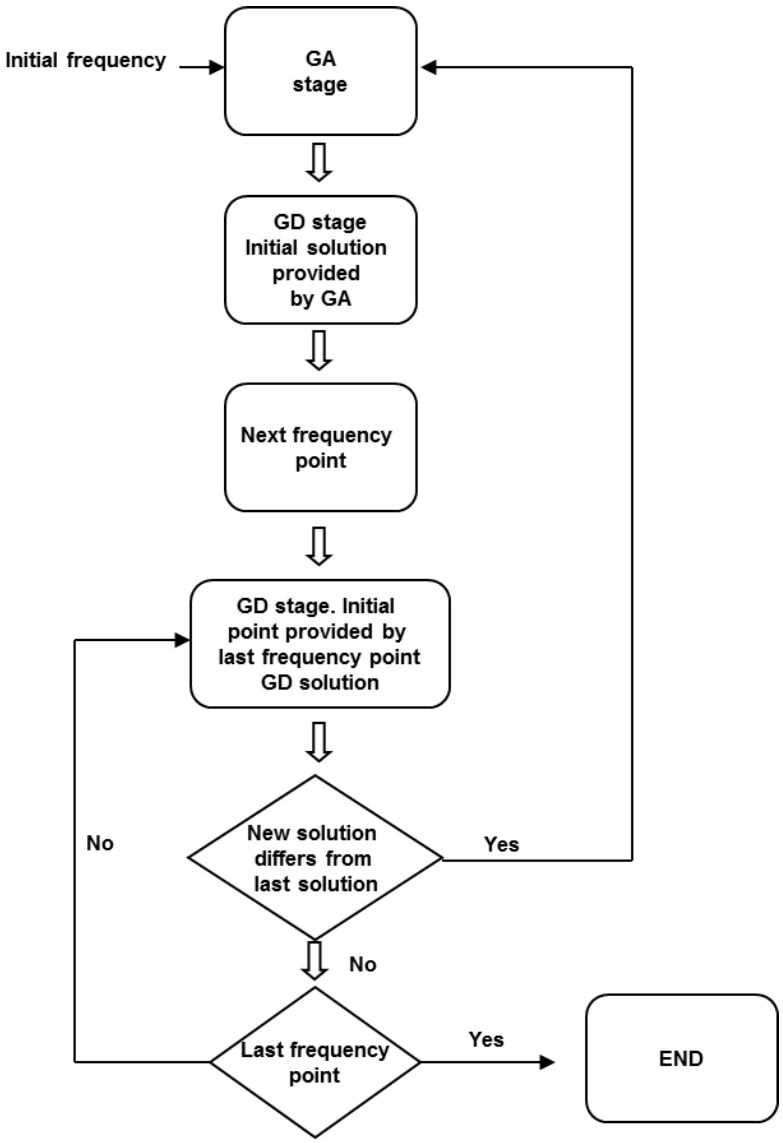

Figure 2.7: Flowchart of the optimization procedure used for the characterization of the transitions. GA: genetic algorithms, GD: gradient descent method.

gradient descent optimization method by using as initial point for the search procedure the best solution obtained in the genetic algorithms' stage. Once the solution for the first frequency point is obtained with the required accuracy, the solution of the following frequency point is calculated with the gradient descent method by using as initial point the solution of the preceding frequency point iteratively. It is assumed then that the solution shows a slow variation; otherwise a sharp deviation may lead to wrong solution values increasing the fitness function evaluation. In this case a genetic algorithms stage is generated again for the wrong last frequency point calculation.

A previous study for deembedding and unterminating symmetrical microwave fix-

tures using genetic algorithms can be found in [41] although the approach is different and only one thru standard is employed.

In this case, an individual of genetic algorithms represents a possible solution of our problem that contains the estimation of 12 different unknown real parameters necessary to characterize the two transitions. In a first stage a random initial population with 100 individuals is evaluated. After this stage, crossover and mutation operations define the following generations evolving towards the optimum individual (our solution). In our case, 12 unknown parameters require a high number of individuals and generations to reach a good approximation. Thus, 200 generations, 100 individuals, 80 crossovers per generation and 5 mutations per generation have been used during the genetic algorithms' stage.

The gradient descent optimization stage uses a multivariable Matlab® function that implements the Quasi-Newton method.

The evaluation function becomes a crucial aspect in both genetic algorithms and gradient descent optimization stages. This evaluation function takes into account the magnitude of the difference between the measured complex scattering parameters (S_{ij}^m) and the simulated ones (S_{ij}^s) for different experimental set-ups.

The expression used to evaluate the error when using the transition connected to a short-circuit standard during the optimization procedure is shown in (2.22). To evaluate a line connection between transitions (2.23) is used. The evaluation function expression including all the error contributions is shown in (2.24). The evaluation is carried out for each frequency point.

$$f_{short} = |S_{11}^m - S_{11}^s|^2 \tag{2.22}$$

$$f_{thru/line} = \sum_{i=1}^{2}\sum_{j=1}^{2}\left|S_{ij}^m - S_{ij}^s\right|^2 \tag{2.23}$$

$$f = \sqrt{f_{thru} + f_{line1} + f_{line2} + f_{short1} + f_{short2} + f_{short3}} \tag{2.24}$$

Different standard load combinations have been considered in order to assess the precision of this unterminating technique versus the number and type of used standards. Therefore, if any of the standards is not used during the optimization process its contribution to function f will be considered null.

2.5.2 Application to the characterization of a device under test

A precise evaluation of any transition becomes essential to characterize a device under test (DUT). The proposed inverse characterization technique can be employed to evaluate the transitions jointly with the DUT [42]. In this case the unterminating procedure is carried out by minimizing the error between calculations of scattering matrix concatenations that contain the transitions and the DUT as unknown

parameters and measurements of several structures that reproduce the calculated scenarios.

The two-port scattering parameters of each coaxial-to-waveguide transition and those of the DUT are modelled through their magnitude and phase representation. This leads to 18 different unknown real parameters when considering the fact that $S_{12} = S_{21}$ due to reciprocity. The S matrices for each transition are those previously shown in (2.20) and (2.21), while the scattering matrix for the DUT is defined as shown in (2.25).

$$\begin{bmatrix} S_{11}^{DUT} & S_{12}^{DUT} \\ S_{21}^{DUT} & S_{22}^{DUT} \end{bmatrix} = \begin{bmatrix} Ge^{j\phi_7} & He^{j\phi_8} \\ He^{j\phi_8} & Ie^{j\phi_9} \end{bmatrix} \tag{2.25}$$

where G, H, $I \in [0, 1]$ represent the magnitude of the parameters and ϕ_7, ϕ_8, $\phi_9 \in [-\pi, \pi]$ are their phase values.

18 unknown parameters require a higher number of individuals and generations to reach a good approximation. Thus, 300 generations, 150 individuals, 120 crossovers per generation and 5 mutations per generation have been used during the genetic algorithms' stage.

2.5.3 Application to the modelling of printed circuit boards inside a metallic enclosure

The electrical behaviour of printed circuit boards (PCBs) inside of a protecting cabinet is a key issue to understand the shielding performance of an enclosure with built-in apertures designed for airing purposes. On the one hand, the electromagnetic (EM) interferences that may lead to an unwanted or uncontrolled behaviour of the device. On the other hand, the presence of the PCB within the protecting cabinet forces a redistribution of the field patterns inside the enclosure shifting the original problem when the case was empty to a different one.

The EM interactions with PCBs have been studied in several works. The simplest approximation to model a PCB in a shielding scenario consists of modelling the tracks and the composite structure of the board with the components attached to it as a perfect electric conductor (PEC) plate with the same dimensions as the PCB. Such approximation assumes a homogeneous ground plane as the main contribution for the model. This simply model has been used in studies with semi-analytical [43] and numerical [44] methods. However, this model does not take into account the losses due to the circuitry on the PCB, neither the ones due to all the materials building up the device.

In [45] it was stated that a populated PCB could be modelled for computational purposes by a homogeneous sheet of a lossy conductor and characterized by its

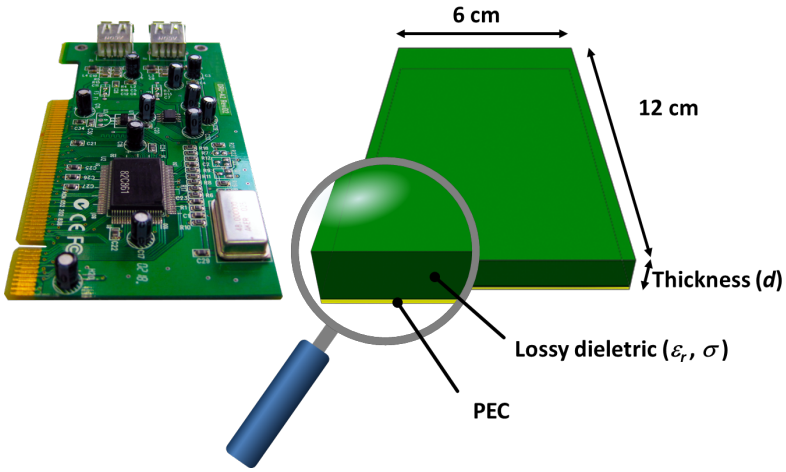

Figure 2.8: PCB equivalent model.

reflection and transmission coefficients, depending on the requirements of the computational algorithm. An accurate EM equivalent model of a PCB without a ground plane was modelled by a slab of homogeneous dielectric material that filled up the cross-section of the waveguide in [46]. The perturbation caused by several types of grounded and floating PCBs within an enclosure was empirically studied in [47] and compared with computational simulations by using the TLM technique. The study concluded that a reasonable equivalent model could be a sheet of a conducting plane plus a lossy dielectric with the same dimensions as the real PCB. Nevertheless, the experimental characterization of such work introduced setup mismatches into the PCB characterization, so the coupling effects where not taken into account.

This thesis goes a step further in such reasonable approximation by applying the inverse technique to the characterization of both transitions and PCB equivalent models for providing accurate results. The damping effect produced by the lossy materials of any PCB can be reproduced computationally by adding a lossy layer to the conducting plane of its EM equivalent model. This model assumes that both the PEC plate and the lossy layer have the same surface area than the original PCB, but it requires the characterization of the thickness (d), dielectric constant (ε_r) and electrical conductivity (σ) of the lossy slab (see Fig. 2.8).

Traditionally, measurements performed in protecting cabinets to assess their shielding features are carried out by using coaxial probes that are inserted into the metallic cavity. These coaxial probes attached to the metallic enclosure are often referred as coaxial-to-waveguide transitions in microwave bibliography, as explained before.

In [48] an efficient analytical tool was presented to evaluate the EM coupling between two wires within an empty metallic cavity. Nevertheless, some issues may affect the accuracy of the results and distort the assessment, such as the mechanical tolerances in manufacturing the enclosure, the soldering quality of the ground line of the coaxial cables or even the inclusion of connectors and/or adaptors. When evaluating the

EM perturbation inside an enclosure when it is loaded with a PCB, those issues must be handled properly, otherwise their influence might be erroneously attributed to the PCB perturbation under study, and consequently, the calculation of the EM equivalent model parameters would be affected as shown in [47].

The method presented in [49] is used to provide accurate results for the PCB equivalent model inside the cavity. However, in this case we go a step further to overcome any other external factors such as the coupling of coaxial probes used in measurements. The method is based on the accurate experimental characterization of the S-parameters of both coaxial probes installed in the enclosure by using the empirical data registered from a rigorous calibration procedure. Once the probes are characterized, their scattering matrices are used during the needed simulations of the inverse procedure to obtain the PCB equivalent model.

In [50] a new proposed definition for the shielding effectiveness measurement of enclosures would require a set of different representative contents (RCs) for loading the protecting cabinets under test. The method presented in this thesis can be used when an accurate model for a representative content is required.

Fig. 2.9 shows the scheme of the new two-step procedure used in this work to obtain the PCB equivalent model [51]. During the first step, the coaxial-to-waveguide transitions used in the experimental measurements are fully characterized and their complex scattering matrices are obtained for all the frequency points under study, as explained before. The procedure has been slightly modified here in order to be able to work with a complete metallic cavity instead of a cavity built up of different assembled parts. In fact, the enclosure was virtually divided into three parts as shown in Fig. 2.10: two coaxial-to-waveguide transitions and a central waveguide part. Each of these virtual parts is characterized by their scattering matrix and then concatenated to obtain the whole response of the enclosure.

Once the coaxial-to-waveguide transitions are characterized by the de-embedding technique, it is possible to obtain the PCB EM equivalent model by comparing the effects measured in the real enclosure loaded by the PCB and the ones computed in the virtual modeling.

The simulated scattering matrix of the whole metallic enclosure was computed as follows. The waveguide containing the PCB EM equivalent model was simulated with CST MICROWAVE STUDIO® and assuming a monomodal excitation. Afterwards, an analytical concatenation of the de-embedded transition 1, the waveguide containing the PCB equivalent model and the de-embedded transition 2 scattering matrices was computed by using Matlab® functions that concatenate a cascade of scattering matrices. CST simulations were controlled by Matlab® under Visual Basic Application (VBA) macro language, which provides an easy implementation of any optimization method.

The genetic algorithm was used in order to minimize the difference between simulated results and the measured data during the computation of the optimized PCB

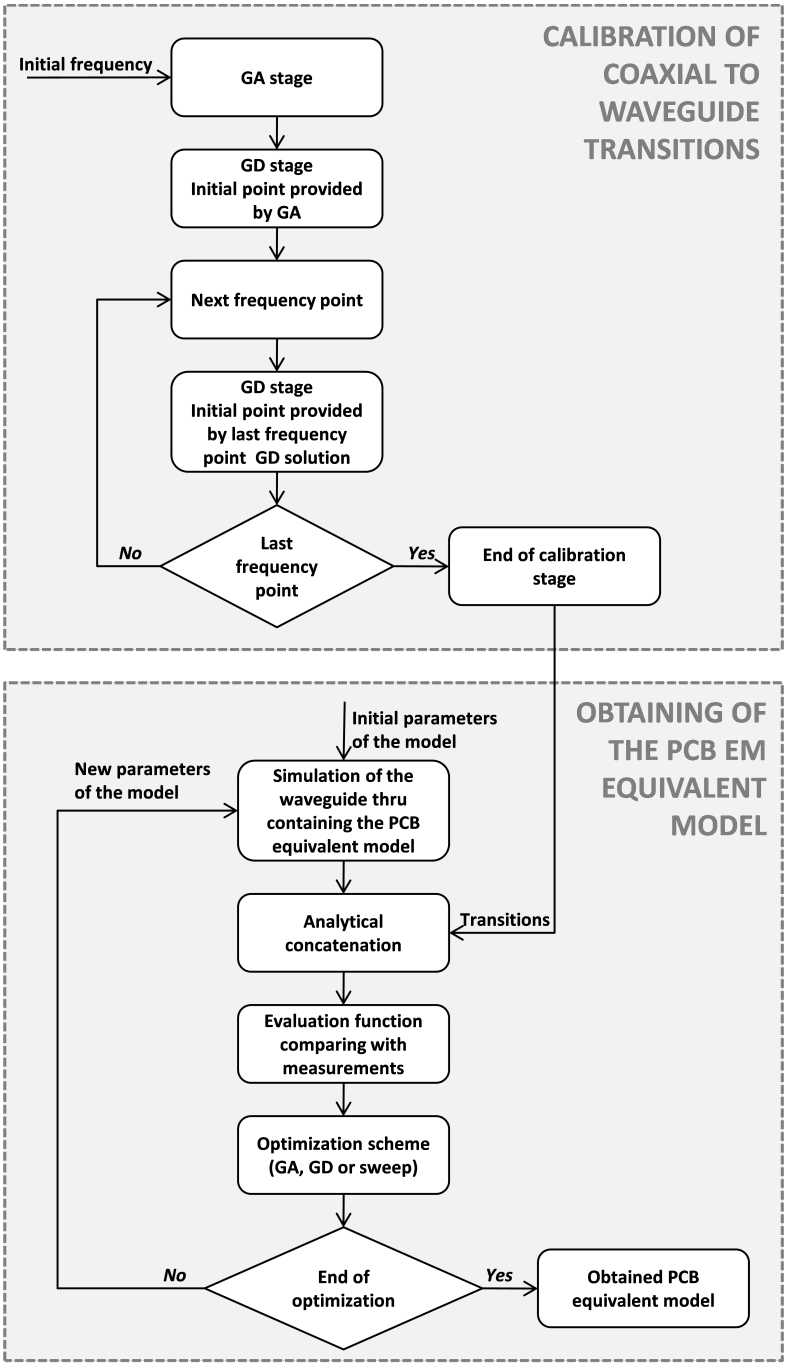

Figure 2.9: Scheme of the two-step procedure for obtaining the PCB equivalent model.

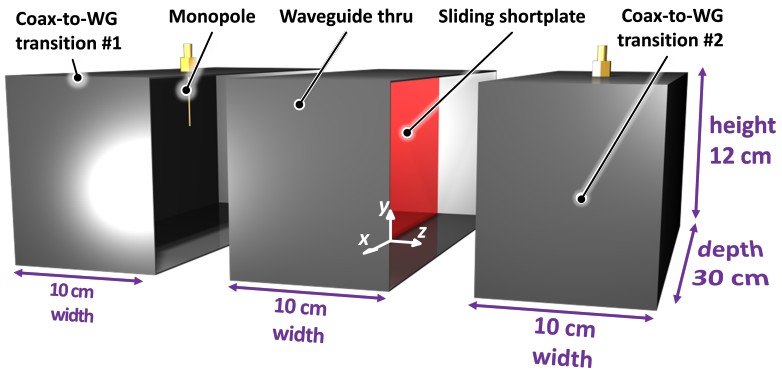

Figure 2.10: Metallic enclosure virtually decomposed in order to characterize coaxial-to-waveguide transitions.

EM equivalent model. An individual from the genetic algorithm represents a possible solution of the problem that contains the estimation of the 3 different unknown parameters (thickness, dielectric constant and electrical conductivity) necessary to characterize the PCB EM equivalent model. The search limits for the optimization algorithms were: [0.5, 30] mm for the dielectric thickness (d), [1, 10] for the dielectric constant (ε_r) and [0, 0.3] S/m for the electrical conductivity (σ). Initially, a random population of 20 individuals was evaluated, while the crossover and mutation operations defined the following 20 generations evolving towards the optimum individual.

The fitting function for obtaining the proposed PCB EM equivalent model is shown in (2.26), where S'^{m}_{ijk} are the scattering parameters of the metallic enclosure containing the PCB measured with the vector network analyzer, S'^{s}_{ijk} are the simulated scattering parameters of the whole enclosure containing the PCB EM model, i and j are the index reference port numbers for the scattering parameters, k is the index for each frequency point and N is the number of frequency points in the range under evaluation.

$$f_{pcb} = \frac{\sqrt{\sum_{i=1}^{2}\sum_{j=1}^{2}\sum_{k=1}^{N}\left|S'^{m}_{ijk} - S'^{s}_{ijk}\right|^2}}{N} \tag{2.26}$$

2.6 Corrugated waveguide bandstop filters

2.6.1 Analysis method

The analysis and design of corrugated filters have traditionally been performed by an approximate method based on monomode equivalent circuits [52,53]. Provided that

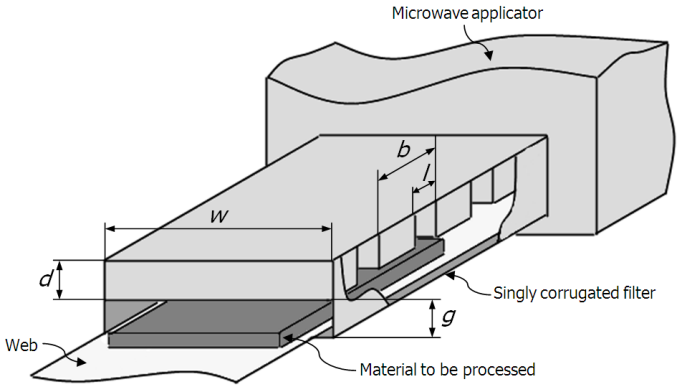

(a) Singly corrugated filter

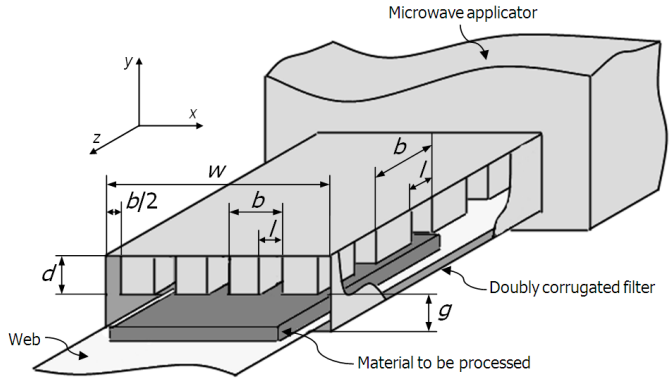

(b) Doubly corrugated filter

Figure 2.11: Singly and doubly corrugated filters under consideration.

the validity restrictions of the monomode representation are satisfied, the method is accurate enough for singly corrugated filters. However, it does not give very precise results for more complex structures, such as the doubly corrugated configurations [55]. In [56], a multimode analysis method based on the generalized admittance matrix (GAM) representation, reported in [57], is proposed for the accurate analysis of singly and doubly corrugated filters. Additionally, a more precise design technique of such structures is also described. This technique exploits the accuracy and efficiency of the new analysis method proposed in order to refine the initial solution provided by the traditional design method.

The structures under consideration are the singly and doubly corrugated filters shown in Figs. 2.11a and 2.11b, respectively.

To analyze these filters, they are decomposed into planar waveguide junctions and sections of uniform waveguide interconnecting them. For the accurate and efficient characterization of these two basic building blocks, the GAM formulation is chosen. Any planar waveguide junction can be easily modeled by a GAM representation following the efficient method proposed in [57]. As a result, the admittance matrix

elements take the following form:

$$Y_{m,n}^{(1,1)} = (-j)\, Y_{0n}^{(1)} \cot\left(\beta_m^{(1)} l_{ref}\right) \delta_{m,n} \tag{2.27}$$

$$Y_{m,n}^{(2,1)} = Y_{m,n}^{(1,2)} = jY_{0n}^{(1)} \csc\left(\beta_n^{(1)} l_{ref}\right) \left\langle \mathbf{h}_n^{(1)}, \mathbf{h}_m^{(2)} \right\rangle \tag{2.28}$$

$$Y_{m,n}^{(2,2)} = (-j) \sum_{r=1}^{\infty} Y_{0r}^{(1)} \cot\left(\beta_r^{(1)} l_{ref}\right) \left\langle \mathbf{e}_r^{(1)}, \mathbf{e}_n^{(2)} \right\rangle \left\langle \mathbf{h}_r^{(1)}, \mathbf{h}_m^{(2)} \right\rangle \tag{2.29}$$

where $\mathbf{e}_p^{(\delta)}$ and $\mathbf{h}_p^{(\delta)}$ are, respectively, the transverse electric and magnetic normalized vector-mode functions of the p-th mode in region δ ($\delta = 1$ for the waveguide with bigger cross section or $\delta = 2$ for the smaller waveguide in the junction), $\beta_p^{(\delta)}$ and $Y_{0p}^{(\delta)}$ represent the propagation constant and characteristic admittance of the pth mode in region δ, l_{ref} is a reference length in the bigger waveguide, and $\delta_{m,n}$ represents the Kronecker delta. All the TE and TM modes in (2.27)-(2.29) are sorted according to their increasing cutoff wavenumber.

From (2.27) to (2.29), it is obvious that the main computational effort comes from the evaluation of the $Y_{m,n}^{(2,2)}$ elements because they involve series to be evaluated at each frequency point. The number of terms to be considered in such series is determined through convergence studies. For the planar waveguide junctions involved in the structures considered in this thesis, practical studies have revealed that 400 terms are required to obtain convergent results. This computational effort can be reduced dramatically following the acceleration technique proposed in [58], which consists on extracting the frequency dependence of the aforementioned series. Using this technique, the frequency computations required to evaluate the elements are essentially reduced to adding, at most, ten terms.

As is evident from (2.27)-(2.29), the proposed analysis technique requires to know the modal spectrum of both waveguides involved in any planar junction, as well as the modal coupling coefficients between these two sets of modes. This modal information can be obtained analytically for waveguides with standard cross section, such as the rectangular ones. Unfortunately, the junctions present in the doubly corrugated filters always imply multiridged waveguides. The modes of such waveguides and the coupling integrals required are obtained efficiently implementing the method fully described in [59] and [60]. This procedure consists essentially of rewriting the Helmholtz equation in a form that gives rise to a linear matrix eigenvalue problem once the Galerkin method is used to obtain the modal solution. After some post-processing of the matrices already used to find the modes, the algorithm then also allows to compute straightforwardly the coupling integrals required. The sections of uniform waveguide connecting the planar waveguide junctions of the structure are also characterized by a GAM representation. According to [1], the admittance parameters are given by the well-known expressions:

$$Y_{m,n}^{(1,1)} = Y_{m,n}^{(2,2)} = (-j)\, Y_{0n}^{(1)} \cot\left(\beta_n^{(1)} l_{wg}\right) \delta_{m,n} \tag{2.30}$$

$$Y_{m,n}^{(2,1)} = Y_{m,n}^{(1,2)} = j Y_{0n}^{(1)} \csc\left(\beta_n^{(1)} l_{wg}\right) \delta_{m,n} \tag{2.31}$$

where l_{wg} now represents the waveguide section length.

After cascading the admittance matrices, which represent the basic building blocks of the structure considered, and applying the corresponding load conditions, a banded linear system is finally obtained. The efficiency of the analysis technique proposed also depends on the number of interacting modes chosen at the waveguides of the structure. Such a number must be determined in order to obtain accurate results, and it is practically derived from convergence studies of the S-parameters of the whole structure.

In this work, however, we will use CST MICROWAVE STUDIO® in order to analyze all the proposed structures due to its complexity.

2.6.2 Design technique

As can be seen in Fig. 2.11a, a singly corrugated filter is a periodic cascade of pure capacitive steps in rectangular waveguide, which allows to eliminate only the radiation of open-ended waveguide systems related to the fundamental mode (i.e., TE_{10}). For the design of these devices, the traditional method described, for instance, in [53], is initially chosen since it provides good results in most practical situations. The traditional design method is based on a monomode equivalent representation of all the elements integrating the structure. Therefore, the E-plane T-junctions of the structure are modeled by the monomode equivalent circuit proposed in [61], whereas the rectangular waveguides interconnecting such T-junctions are represented by a simple transmission line related to the fundamental mode. Exploiting the periodicity of the monomode equivalent circuit of the filter, the image method described in [62] is then used to determine a simple expression for the attenuation response:

$$\alpha\,(\mathrm{dB}) = 8.686\; n\; \mathrm{acosh}\left(\left|\cos\left(\beta l'\right) - \left(\overline{X}_T + m_T^2 \frac{b}{g} \tan\left(\beta d'\right)\right) \cdot \frac{\sin\left(\beta l'\right)}{2}\right|\right) \tag{2.32}$$

where n represents the number of sections (i.e., E-plane T-junctions) of the filter, β is the propagation constant of the fundamental mode, b and g are physical parameters of the filter shown in Fig. 2.11a, and l', $\overline{X}_T$, m_T, and d' are electrical parameters derived from the equivalent circuit of a filter section [54, 61]. In order to maximize the attenuation response given by (2.32), it can be simply deduced that the d- and l-parameters must take the following values:

$$d = \left.\frac{\lambda_{g,\mathrm{TE}^z_{10}}}{4}\right|_{f=f_0} - d_T \tag{2.33}$$

$$l = \left.\frac{\lambda_{g,\mathrm{TE}^z_{10}}}{4}\right|_{f=f_0} + 2l_T \tag{2.34}$$

where f_0 is the central frequency of the stopband and d_T, l_T are again electrical parameters of the monomode equivalent circuit of the T-junctions, whose explicit expressions can be found in [61]. From such expressions, it is concluded that the values of d_T and l_T depend on the physical parameters g, w and b. The g- and w-parameters are fixed by the material dimensions. With regard to the value of the b-parameter, it must be chosen in order to optimize (2.32), but taking care of not violating the validity range of the monomode equivalent circuit (a higher value of b implies a shorter distance between consecutive T-junctions, thus exciting higher order modes not considered in the model). Finally, as can be deduced from (2.32), the number of sections of the filter determines the level of attenuation, and it is, therefore, suitably chosen in order to fulfill the electrical specifications of the filter.

The values of the physical parameters given by the design technique are then inserted into the electromagnetic simulator and the response of the filter is finally refined with regard to specifications. This last step of the design technique can be of paramount importance in those cases where the validity restrictions of the monomode equivalent circuit of the structure are not satisfied.

On the other hand, a doubly corrugated filter has an additional set of longitudinal slots cut through the transverse corrugations, as can be seen in Fig. 2.11b. If the center-to-center spacing of the resulting teeth is small in terms of the free-space wavelength, this structure will be essentially isotropic, and will have nearly the same characteristics for TEM waves propagating through it in any direction parallel to the web [52, 53]. Since any TE^z_{m0} mode can be decomposed into two of such TEM wave components, a doubly corrugated filter designed to reflect back these TEM waves can avoid the leakage of energy related to all TE^z_{m0} modes, which allows wider system ports very useful in many practical applications. Traditionally, the design procedure just explained for singly corrugated filters has also been employed for the doubly corrugated case, once the fundamental mode wavelength ($\lambda_{g,\mathrm{TE}^z_{10}}$) is replaced by the free-space wavelength (λ_0) corresponding to TEM waves [55]. Unfortunately, this design procedure of doubly corrugated filters is based on rough approximations and does not usually provide very accurate results. However, the physical dimensions given by such a design procedure can be used as a good starting point to optimize the geometry of the structure in order to fulfill the electrical specifications.

2.6.3 Application to the reduction of the crosscoupling in multifed multimode cavities

Multimode applicators are widely used in many industrial applications for microwave heating of bulk materials [54]. One important issue in the design of a multimode cavity is the fact of using single or multiple magnetrons. This issue is studied in [63], where some advantages and disadvantages of both alternatives are discussed in order to improve the heating uniformity. With multiple sources it is possible to distribute power so as to obtain a better excitation of the modes, yielding better heating uniformity. Further research on this matter can be found in [64,65], where the position of each feed is selected by using genetic algorithms optimization procedures in order to improve the heating uniformity with reduced levels of crosscoupling between feeds. One of the main drawbacks of using multiple feeds is the mutual coupling, referred to as crosscoupling or intercoupling, which decreases overall system efficiency and can damage the magnetrons. In order to prevent this crosscoupling between feeds and to obtain heating uniformity, each feed should excite an independent set of resonant modes [63,66]. Thus, placing the feeds around the cavity walls becomes a complicated task, particularly when dealing with loaded cavities. Approaches such as orthogonal feed placement may be useful in some cases though they can be used just once per cavity section. Even optimization procedures may be useless in some cases because the simulation of this kind of electromagnetic problems is very time-consuming.

In this thesis we present a new approach for reducing the crosscoupling between feeds based on the use of doubly corrugated reactive filters. In this case the filter is placed inside the cavity, dividing it into independent stages separated by the filter.

2.7 Filters traditionally used in doors for microwave ovens

As it has been explained earlier, the health issue and its solution is of paramount importance in microwave ovens, particularly in a domestic environment. If the oven is totally enclosed in a complete metal chamber, there is no safety problem. But then a door is necessary to place food in the cavity. The first obvious approach would be to use a metallic gasket to seal the door. The problem is that such a gasket can fatigue and fail or may become covered with food spillage and become ineffective. Clearly a noncontacting door or seal becomes essential for a safe and reliable microwave oven.

Nowadays, nearlly all microwave ovens in the world use a serrated choke design first proposed for a slot on the narrow wall of a rectangular waveguide employed in a multichannel scanning radar system for the U.S. Navy [67,68]. This design is shown in Fig. 2.12.

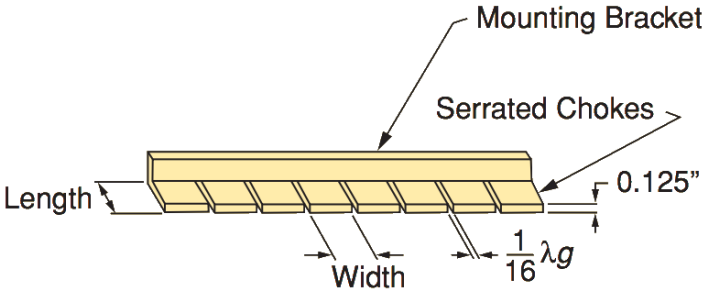

Figure 2.12: Several serrated chokes are combined to form a rectangular cross-section choke [69].

This choke was adopted for oven manufacture since it addressed feasibility, safety issues, and economy. In current microwave ovens, the choke is hidden from view by an opaque plastic strip near the oven cavity periphery. The strip can be easily cleaned to remove food spillage that would inhibit choke effectiveness.

2.7.1 Application to catering microwave ovens with hot and cold compartments

A compact and very flat microwave-heating oven for catering purposes comprising an upper multimode cavity with radiating slots that feed the microwave energy into a lower cavity has been developed in this thesis and patented. The lower cavity provides an electromagnetic separation between the two sides of the cavity by means of a door-like filtering structure in such a way that the microwave energy is confined to one side of the oven, namely, hot department. The applicator is specially designed for catering purposes that require some pieces of food to be heated and some others to remain cool. A metallic horizontal and irregular mode stirrer, which is moved in a non-continous optimized way, and an upper multimode feeding cavity with irregular slots improve the microwave heating uniformity at the hot department. The heat dissipated by the magnetron is used and introduced by a convective airflow into the hot department by means of pipes and proper holes.

A brief summary of microwave ovens containing possible features alike to the new design proposed here for the compact microwave oven is provided below:

- In the patent US4133997 [70] a microwave oven providing for the introduction of microwave energy to a cooking cavity through each of two opposite side walls is described.
- In US4144436 patent [71] a microwave oven with a relatively flat mode stirrer cavity mounted on the outside of one of the cooking cavity wall is described.

Within the mode stirrer cavity is a rotating fan-like mode stirrer. Two aperture elements couple energy from the mode stirrer cavity into the cooking cavity.

- The document US4185181 [72] describes a microwave oven having special form of a microwave energy radiation arrangement. It includes a rotatable conductive rod extending into an oven chamber wall, a rotating conductive arm and a conductive plate having the center thereof coincident with the axis of the rod.
- In US 4301347 patent [73], a feed that radiates rotating elliptically polarized electromagnetic waves improving the heating uniformity is described. Crossed slots, a phase shifter and 3-dB hybrid or turnstile junction are used for this purpose.
- In US4324968 [74] a microwave oven cavity excitation system for promoting time-averaged uniformity of microwave energy distribution by means of a radiating X-slot is described. In this case the radiation of the electric field can be electrically changed by means of ferrites or magnetic materials that can change their properties by means of electrical sources.
- The document US4350859 [75] describes a microwave oven feed system having the output probe of the magnetron inserted directly into the microwave enclosure. A rotating feed structure couples the microwave energy towards the food.
- The US4354083 patent [76] shows a microwave oven which produces efficient and uniform heating by utilizing a plurality of slotted feed apertures through which energy enters the top and bottom walls of the cooking chamber.
- In US4458126 patent [77] authors describe a microwave oven with a dual feed excitation system comprising a rotating antenna supported from the top cavity wall and a slotted radiating chamber from the bottom cavity wall.
- A circularly polarized microwave oven where the microwave energy is coupled from a waveguide above the ceiling to the cavity by a rotatable vertical probe is shown in US4580023 patent [78].
- The US4596915 patent [79] illustrates a circularly polarized microwave oven where the microwave energy is coupled from a waveguide above the ceiling to the cavity by a rotatable vertical probe extending through a circular aperture in the cavity.
- An arrangement for feeding microwave energy from a microwave source to the oven cavity comprising an elongated groove-shaped recess in one of the conductive cavity walls is presented at US4849592 patent [80].
- US5828042 patent [81] displays a uniform heating apparatus for a microwave oven and a method thereof which are capable of more uniformly heating food by generating various resonant modes based on the kind of food.

- An even heating apparatus for converting microwave energy emitted from a magnetron to a plurality of resonant modes in a heating chamber by fixing an antenna array plate having multiple antennas therein spaced from the ceiling of the heating chamber is presented in US5874715 document [82].
- US6097018 patent [83] report a microwave oven includes a magnetron for generating electromagnetic energy, a waveguide for guiding and directing the electromagnetic energy into the cooking chamber, and an antenna for radiating the energy into the waveguide. The waveguide includes two openings for uniformly dispersing the electromagnetic energy into the cooking chamber and a short circuit providing a short surface to the antenna.
- US6169277 [84] informs about an apparatus for the selective heating of foods disposed on a serving tray to serving temperature by means of a microwave oven having a gyrotron as a heat source. Individual guide means are provided for guiding the microwave radiation to particular dishes on the tray. Particularly important is the use of a computer control and heat sensors in order to measure the temperature of each food component and to redirect the microwaves by means of mirrors in order to obtain more uniform heating.
- US6777655 [85] communicates a device and method for ensuring more uniform heating of food by microwaves. The method includes providing food in a portion having a predetermined size and shape, and providing a container adapted for receiving and reheating the portion of food in a microwave oven.
- US 6982401 [86] describes a microwave oven including a cavity for placing food therein, a magnetron, a waveguide having at least two slots with T or L shape for guiding the energy to the cooking cavity, and a stirrer fan rotatably mounted inside the cavity.
- A heating attachment for improving uniformity of microwave heating of food product in a food container is presented at US 20050196491 A1 patent [87]. The attachment has a microwave shield of microwave-reflective material.
- The patent US2008099475 [88] describes a microwave oven with a microwave radiator arrange inside a cooking chamber to re-radiate microwaves supplied by a microwave supplier proximate to the upper side of the cooking chamber. The radiator consists of a slot with a dielectric material.
- The patent DE3310703 [89] describes a microwave oven with dual feeding microwave system consisting of a rotating antenna at the top of the chamber and a microwave chamber at the base of the oven both coupled to the magnetron via a common waveguide.
- US20070215612 [90] describes a leaky mode multimode subcavity that serves as a radiator to improve the uniformity of the microwave applicator. This leaky subcavity consists of a perforated metal plate adjacent to a waveguide launcher.

- US4327266 patent [91] solves the microwave heating uniformity in microwave ovens by using a rotating metallic mode stirrer with an arc-shape slot that partially covers the feeding opening of the cavity.
- EP0049551 patent [92] uses an air-driven metallic slotted disc as feeding system. This disc is set at the bottom of the microwave cavity and is connected to the magnetron by means of a waveguide.
- A different uniformization method is used in US4144436 patent [93]. There, the microwave oven includes a relatively flat mode stirrer cavity mounted on the outside of one of the cooking cavity walls, sharing a common wall therewith. Disposed within the mode stirrer cavity is a rotating fan-like mode stirrer. A waveguide supplies 2450 MHz microwave energy to the mode stirrer cavity. Two aperture elements of generally slot configuration and oriented at right angles to each other in the common wall couple energy from the mode stirrer cavity into the cooking cavity. The configuration and relationship of the aperture elements promote uniformity of energy distribution and readily permit adjustment of the energy distribution by empirically adjusting the precise size and location of each aperture element.
- In US3746823 patent [94], a magnetron is coupled to a waveguide having an open end exciting a transition section which is approximately two wavelengths square. The transition section approximately two box is secured over the microwave cavity which has a circular opening formed in the top wall thereof. A disk having a plurality of apertures or slots is routable supported beneath the upper cavity wall in close proximity thereto so that energy is radiated into the cavity in such a manner as to produce uniform and linear heating throughout the cavity. The apertures in the disk appear electrically at multiples of substantially half-wavelengths from the point of the magnetron coupling when the longer dimension of the apertures are transverse to the longitudinal dimension of the waveguide.

From this revision it can be stated that, although some similar features can be found in some of these designs, none of them consists of an upper multimode feeding cavity with irregular slots, directly coupling to the magnetron, and with irregular mode stirrer in the heating cavity. Additionally, none of the patents include inner filters in order to electromagnetically isolate the compartment with cool food pieces and the cavity where food must be heated. None of the patents show a very flat and compact design as the one proposed here.

Bibliography

[1] R. E. Collin, Foundations for Microwave Engineering, 2nd ed. New York: McGraw-Hill, 1992.

[2] G. Conciauro, M. Guglielmi and R. Sorrentino, Advanced modal analysis, JohnWiley & Sons, Ltd., 2000.

[3] T. Weiland, “A discretization method for the solution of Maxwell’s equations for six-component fields”, Electronics and Communication (AEÜ), vol. 31, pp. 116-120, 1977.

[4] CST STUDIO SUITE™, http://www.cst.com

[5] T. Weiland, “Time domain electromagnetic field computation with finite difference methods”, International Journal of Numerical Modelling, vol. 9, pp. 295-319, 1996.

[6] T. Weiland, “RF & Microwave Simulators - From Component to System Design”, Proc. of the European Microwave Week (EUMW 2003), München, vol. 2, pp. 591-596, Oct. 2003.

[7] B. Krietenstein, R. Schuhmann, P. Thoma, T. Weiland, “The Perfect Boundary Approximation technique facing the challenge of high precision field computation”, Proc. of the XIX International Linear Accelerator Conference (LINAC’98), Chicago, USA, pp. 860-862, 1998.

[8] Y. Rahmat-Samii and E. Michielsen, Electromagnetic Optimization by Genetic Algorithms. New York: John Wiley & Sons, 1999.

[9] M.L. Majewski, R.W. Rose and J.R. Scott, "Modeling and Characterization of Microstrip-to-Coaxial Transitions”, IEEE Trans. Microw. Theory Tech., vol.29, no.8, pp. 799-805, Aug. 1981.

[10] J.R. Souza and E.C. Talboys, “S-parameter characterisation of coaxial to microstrip transition”, IEE Proceedings Microwaves, Optics and Antennas, vol.129, no.1, pp.37-40, Feb. 1982.

[11] S.E. Gourley and A.G Chapman, “Broadband Characterisation of Coaxial to Microstrip Transitions”, 12th European Microwave Conference, pp.622-627, Oct. 1982.

[12] C. Capsalis, C. P. Chronopoulous and N. K. Uzunoglu, “A rigorous analysis of a coaxial to shielded microstrip line transition”, IEEE Trans. Microw. Theory Tech., vol.37, no.7, pp.1091-1098, Jul. 1989.

[13] J. Chramiec and J. K. Piotrowski, “Novel approach to the characterization of coaxial-to-microstrip transitions”, 27th European Microwave Conference, vol. 2, pp. 697-702, Oct. 1997.

[14] J. Chramiec, B. Janiczak, J. Komisarczuk, J. K. Piotrowski and W. Gwarek, “CAD Models of Connectors and Transitions used in Hybrid Microwave Integrated Circuits”, 28th European Microwave Conference, vol.1, pp.457-462, Oct. 1998.

[15] F. Dagang, Z. Dong and S. Yuxuan, “Accurate analysis of the coax-to-microstrip transition by using FDTD method”, International Conference on Computational Electromagnetics and its Applications (ICCEA ’99), pp. 218-221, 1999.

[16] S. A. Wartenberg and Qing Huo Liu, “A coaxial-to-microstrip transition for multilayer substrates”, IEEE Trans. Microw. Theory Tech., vol.52, no.2, pp. 584-588, Feb. 2004.

[17] B. K. O’Neil and J. L. Young, “Evaluation of coplanar waveguide-to-microstrip transitions for precision S-parameter measurements”, Microw. Opt. Technol. Lett., vol.50, no.10, pp. 2667-2671, 2008.

[18] R. Torres-Torres, G. Hernandez-Sosa, G. Romo and A. Sanchez, “Characterization of Electrical Transitions Using Transmission Line Measurements”, IEEE Trans. on Advanced Packaging, vol.32, no.1, pp.45-52, Feb. 2009.

[19] J. F. Liang, H. Chang and K. A. Zaki, “Coaxial probe modeling in waveguides and cavities”, IEEE Trans. Microw. Theory Tech., vol.40, no.12, pp.2172-2180, Dec. 1992.

[20] M. Hajian, D. P. Tran and L. P. Ligthart, “Modeling the transition between a coaxial line and a flat rectangular waveguide”, 9th International Conference on Antennas and Propagation, vol.1, pp. 269-272, Apr. 1995.

[21] Hui-Wen Yao and K. A. Zaki, “Modeling generalized coaxial probes in rectangular waveguides”, IEEE MTT-S International Microwave Symposium Digest, pp. 979-982, vol.2, 16-20, May 1995.

[22] Y. F. Huang, H. David, S. Raymond, and P. Protap, “Modeling of cavity-backed coaxial line to rectangular waveguide junction,” International Journal of RF and Microwave Computer Aided Engineering, vol.8, no.1, pp. 20-26, 1998.

[23] J. Randa, “Comparison of adapter characterization methods”, IEEE Trans. Microwave Theory Tech., vol. 47, no. 12, pp. 2613-2620, Dec. 1999.

[24] J. P. Hoffmann, P. Leuchtman, A. Kretz, J. Rüfenacht, and R. Vahldieck,”Characterization of coaxial adapters for S-parameter measurements”, 38th European Microwave Conference, pp. 313-316, Oct. 2008.

[25] R.F. Bauer and P. Penfield, “De-embedding and unterminating”, IEEE Trans. Microwave Theory Tech., vol. MTT-22, pp. 282-288, Mar. 1974.

[26] D. Williams, “De-embedding and Unterminating Microwave fixtures with Nonlinear Least Squares”, IEEE Trans. Microwave Theory Tech., vol. 38, pp. 787-791, June 1990.

[27] R.B: Marks, “A multiline method of analyzer calibration”, IEEE Trans. Microwave Theory Tech., vol. 39, pp.1205 -1215, July 1991.

[28] R.B. Marks and D.F. Williams, “Characteristic impedance determination using propagation constant measurement”, IEEE Microwave and Guided Wave Letters, vol. 1, pp.141-143, June 1991.

[29] R.B. Marks and D.F. Williams, “Accurate Transmission Line Characterization”, IEEE Microwave and Guided Wave Letters, vol. 3, pp. 247-249, Aug. 1993.

[30] R.B. Marks and D.F. Williams, “Accurate Experimental Characterization of Interconnects”, IEEE Trans. Components, Hybrids and Manufacturing Tech., vol. 15, pp. 601-602, Aug. 1992.

[31] X. P. Liang, K. A. Zaki, and A. E. Atia “A rigorous three plane mode-matching technique for characterizing waveguide T-junctions, and its application in multiplexer design,” IEEE Trans. Microw. Theory Tech., vol.39, no.12, pp.2138-2147, Dec. 1991.

[32] A. A. Kirilenko, S. L. Senkevich, V. I. Tkachenko, and B. G. Tysik, “Waveguide diplexer and multiplexer design,” IEEE Trans. Microw. Theory Tech., vol.42, no.7, pp.1393-1396, Jul. 1994.

[33] F. Arndt, I. Ahrens, U. Papziner, U. Wiechmann, and R. Wilkeit, “Optimized E-Plane T-Junction Series Power Dividers,” IEEE Trans. Microw. Theory Tech., vol.35, no.11, pp. 1052-1059, Nov. 1987.

[34] G. Gerini, and M. Guglielmi, “Full-wave CAD of a rectangular waveguide filter with integrated coaxial excitation,” IEEE Trans. Microw. Theory Tech., vol.49, no.5, pp.986-989, May 2001.

[35] G. Gerini, F. D. Bustamante, and M. Guglielmi, “Triple mode filters with coaxial excitation,” IEEE MTT-S International Microwave Symposium Digest, vol.3, pp.1763-1766, 2000.

[36] Z. Shen; C. Feng, “A new dual-polarized broadband horn antenna”, IEEE Antennas and Wireless Propagation Letters, vol.4, pp. 270-273, 2005.

[37] A. J. Lozano-Guerrero, F. J. Clemente-Fernandez, J. Monzó-Cabrera, J. L. Pedreño-Molina and A. Díaz-Morcillo, "Precise evaluation of coaxial to waveguide transitions by means of inverse techniques”, IEEE Trans. Microw. Theory Tech., vol.58, no.1, pp.229-235, Jan. 2010.

[38] M. E. Requena-Pérez, A. Albero-Ortiz and J. Monzó-Cabrera, “Combined use of genetic algorithms and gradient descent optimization methods for accurate inverse permittivity measurement”, IEEE Trans. Microw. Theory Tech., vol.54, no. 2, pp. 615-624, Feb. 2006.

[39] D.F. Williams, J.C.M. Wang and U. Arz, "An optimal vector-network-analyzer calibration algoritm", IEEE Trans. Microw. Theory Tech., vol.51, no. 12, pp. 2391-2401, Dec. 2003.

[40] K. Rothemund, H. W. Glock and U. van Rienen, "Eigenmode calculation of complex RF-structures using S-parameters", IEEE Trans. Magn., vol.36, no.4, pp.1501-1503, Jul. 2000.

[41] A. S. Adalev, N. V. Korovkin, M. Hayakawa and J. B. Nitsch, "Deembedding and unterminating microwave fixtures with the genetic algorithm", IEEE Trans. Microwave Theory Tech., vol. 54, no. 7, pp. 3131-3140, Jul. 2006.

[42] A. J. Lozano-Guerrero, J. Monzó-Cabrera, F. J. Clemente-Fernández, J. L. Pedreño-Molina and A. Díaz-Morcillo, "Coaxial to waveguide transitions and device under test characterization by means of inverse techniques", Microw. Opt. Technol. Lett., vol. 52, no. 6, pp. 1294-1297, June 2010.

[43] R. Azaro, S. Caorsi, M. Cosso, G. M. Costini, M. Donelli, R. Ene, G. L. Gragnani and M. Pastorino, "A semianalytical approach for the evaluation of radiated immunity on a printed-circuit board in metallic enclosures", Microwave Opt. Technol. Lett., vol. 27, pp. 204-207, Nov. 2000.

[44] W. Wallyn and D. De Zutter, "Modeling the shielding effectiveness and resonances of metallic shielding enclosures loaded with PCBs", IEEE International Symposium on Electromagnetic Compatibility, vol. 2, pp. 691 696, Aug. 2001.

[45] M. P. Robinson, S.J. Porter and P Op gen Oorth, "Reflection and transmission coefficients of printed circuit boards", 4th Eur. Symp. EMC, Brugge, Sep. 2000.

[46] D. W. P. Thomas, A. C. Denton, T. Konefal, T. Benson, C. Christopoulos, J. F. Dawson, A. Marvin and S. J. Porter, "Characterisation of the shielding effectiveness of loaded equipment enclosures", International Conference and Exhibition on Electromagnetic Compatibility, pp. 89 94. Jul. 1999.

[47] D. W. P. Thomas, A. C. Denton, T. Konefal, T. Benson, C. Christopoulos, J. F. Dawson, A. Marvin, S. J. Porter and P. Sewell, "Model of the electromagnetic fields inside a cuboidal enclosure populated with conducting planes o printed circuit boards", IEEE Trans. on Electromagn. Compat., vol. 43, no. 2, pp. 161 169, May 2001.

[48] T. Konefal, J. F. Dawson, A. Denton, T. M. Benson, C. Christopoulos, A. C. Marvin, S. J. Porter and D. W. P. Thomas, "Electromagnetic field predictions inside screened enclosures containing radiators", in Proc. Inst. Elect. Eng. Conf. Electromagnetic Compatibility, vol. 464, pp. 95 100, July 1999.

[49] A. J. Lozano-Guerrero, M. P. Robinson, A. Díaz-Morcillo and J. V. Balbastre-Tejedor, "Evaluation and optimization of an equivalent model for printed circuit boards inside metallic enclosures", General Assembly URSI, Chicago, USA, Aug. 2008.

[50] A. C. Marvin, J. F. Dawson, S. Ward, L. Dawson, J. Clegg and A. Weisenfeld, “A proposed new definition and measurement of the shielding effect of equipment enclosures”, IEEE Trans. on Electromagn. Compat., vol. 46, no. 3, pp. 459 468, Aug. 2004.

[51] A. J. Lozano-Guerrero, J. Monzó-Cabrera, F. J. Clemente-Fernandez, J. Fayos-Fernández, J. L. Pedreño-Molina and A. Díaz-Morcillo, "Electromagnetic equivalent models for printed circuit boards inside a metallic enclosure using a coaxial-to-waveguide transition calibration", IEEE Trans. on Electromagn. Compat., vol. 54, no. 4, pp.931,939, Aug. 2012.

[52] L. Young and B. M. Schiffman, “New and improved types of waffle-iron filters”, Proc. Inst. Elect. Eng., vol. 110, pp. 1191 1198, July 1963.

[53] G. Matthaei, L. Young, and E. M. T. Jones, Microwave Filters, Impedance-Matching Networks, and Coupling Structures. Norwood, MA: Artech House, 1980.

[54] A. C. Metaxas and R. J. Meredith, Industrial Microwave Heating. Stevenage, U.K.: Peregrinus, 1988.

[55] A. L. Vankoughnett and J. G. Dunn, “Doubly corrugated chokes for microwave heating systems”, J. Microwave Power, vol. 8, no. 1, pp. 101 110, Jan. 1973.

[56] P. Soto, V. E. Boria, J. M. Catalá-Civera, N. Chouaib, M. Guglielmi and B. Gimeno, “Analysis, design, and experimental verification of microwave filters for safety issues in open-ended waveguide systems”, IEEE Trans. Microw. Theory Tech., vol. 48, no. 11, pp. 2133-2140, Nov. 2010.

[57] A. Alvarez, G. Connor and M. Guglielmi, “New simple procedure for the computation of the multimode admittance or impedance matrix of planar waveguide junctions”, IEEE Trans. Microwave Theory Tech., vol. 44, pp. 413 418, Mar. 1996.

[58] V. E. Boria and M. Guglielmi, “Accelerated computation of admittance parameters for planar waveguide junctions”, Int. J. Microwave Millimeter-Wave Computer-Aided Eng., vol. 7, no. 3, pp. 195 205, Mar. 1997.

[59] G. Conciauro, M. Bressan and C. Zuffada, “Waveguide modes via an integral equation leading to a linear matrix eigenvalue problem”, IEEE Trans. Microwave Theory Tech., vol. 32, no. 11, pp. 1495 1504, Nov. 1984.

[60] P. Arcioni, “Fast evaluation of modal coupling coefficients of waveguide step discontinuities”, IEEE Microwave Guided Wave Lett., vol. 6, pp. 232 234, June 1996.

[61] N. Marcuvitz, Waveguide Handbook. Stevenage, U.K.: Peregrinus, 1986.

[62] A. F. Harvey, Microwave Engineering. New York: Academic, 1963.

[63] T. V. Chow-Ting-Chan and H. C. Reader, Understanding Microwave Heating, London: Artech House, 2000.

[64] J. M. Catalá-Civera, J. Pitarch, A. J. Canós, F. Peñaranda Foix, J. V. Balbastre and E. de los Reyes, “Improving the heating uniformity in multimode microwave applicators by the optimization of the position of multiple feeds”, Proc. Progress in Electromagnetic Research Symposium Conf., p. 51, 2003.

[65] E. Domínguez-Tortajada, P. Plaza-González, A. Díaz-Morcillo and J.V. Balbastre, “Optimisation of electric field uniformity in microwave heating systems by means of multi-feeding and genetic algorithms”, Int. J. Materials and Product Technology, vol. 29, nos. 1/2/3/4, pp. 149-162, 2007.

[66] T. V. Chow-Ting-Chan and H. C. Reader, “Modelling of modes and perspectives on multiple-feeds in microwave ovens”, J. Microwave Power and Electromagnetic Energy, vol. 31, no. 4, pp. 238-250, 1996.

[67] K. Tomiyasu, “Serrated choke system for electromagnetic waveguide”, U. S. Patent 2772402, Nov. 27, 1956.

[68] K. Tomiyasu and J.J. Bolus, “Characteristics of a new serrated choke”, IRE Trans. Microwave Theory Tech., vol. 4, pp. 33 36, Jan. 1956.

[69] K. Tomiyasu, "Minimizing Radiation Leakage from Microwave Ovens”, IEEE Microwave Magazine, vol. 9, no. 1, pp. 76-78, Feb. 2008.

[70] R. A. Thuleen, “Dual feed, horizontally polarized microwave oven”, U. S. Patent 4133997, Jan. 9, 1979.

[71] H. S. Hauck, “Microwave oven excitation system for promoting uniformity of energy distribution”, U. S. Patent 4144436, Mar. 13, 1979.

[72] T. Funamizu, “Microwave oven”, U. S. Patent 4185181, Jan. 22, 1980.

[73] J. P. Quine, “Feed system for microwave oven”, U. S. Patent 4301347, Nov. 17, 1981.

[74] P. H. Smith, “Microwave oven cavity excitation system providing controlled electric field shape for uniformity of energy distribution”, U. S. Patent 4324968, Apr. 13, 1982.

[75] R. F. Bowen, “Microwave oven feed system”, U. S. Patent 4350859, Jan. 9, 1979.

[76] J. E. Staats, “Microwave oven with novel energy distribution arrangement”, U. S. Patent 4354083, Oct. 12, 1982.

[77] R. L. Dills, L. H. Fitzmayer and R. W, Hunt, “Microwave oven with dual feed excitation system”, U. S. Patent 4458126, Jul. 3, 1984.

[78] J. E. Simpson, “Microwave oven with circular polarization”, U. S. Patent 4580023, Apr. 1, 1986.

[79] J. E. Simpson, “Microwave oven having resonant antenna”, U. S. Patent 4596915, Jun. 24, 1986.

[80] J. S. Claesson and P. O. G. Risman, “Feeding arrangement for a microwave oven”, U. S. Patent 4849592, Jul. 18, 1989.

[81] J. S. Choi and Y. K. Kim, “Uniform heating apparatus for microwave oven and method thereof”, U. S. Patent 5828042, Oct. 27, 1998.

[82] J. S. Choi, “Heating apparatus in the form of an antenna array plate for a microwave oven”, U. S. Patent 5874715, Feb. 23, 1999.

[83] H. J. Kang et al, “Circular polarization generating system for microwave oven”, U. S. Patent 6097018, Aug. 1, 2000.

[84] L. Feher, M. Schnack and S. Schnack, “Apparatus for the selective heating of foods disposed on a tray using a gyrotron for microwave heating of the foods”, U. S. Patent 6169277 B1, Jan. 2, 2001.

[85] H. Zhang et al, “Uniform microwave heating of food in a container”, U. S. Patent 6777655 B2, Aug. 17, 2004.

[86] J. Y. Hu et al, “Microwave oven”, U. S. Patent 6982401 B2, Jan. 3, 2006.

[87] R. Croft et al, “Microwave heating attachment”, U. S. Patent 20050196491, Sep. 8, 2005.

[88] H. Kim and W. Lee, “Cooking apparatus using microwaves”, U. S. Patent 20080099475, May 1, 2008.

[89] D. R. Lindell et al, “Microwave oven with dual feed excitation system”, DE Patent 3310703, Oct. 13, 1983.

[90] I. Ahmad et al, “Apparatus and method for microwave processing of materials”, U. S. Patent 20070215612, Sep. 20, 2007.

[91] B. J. Austin and J. E. Simpson, “Microwave ovens for uniform heating”, U. S. Patent 4327266, Apr. 27, 1982.

[92] P. H. I. Almgren, O. R. Fredriksson and A. M. Nasretdin, “Energy feed system for a microwave oven”, EP Patent 0049551, Jan. 28, 1987.

[93] H. S. Hauck, “Microwave oven excitation system for promoting uniformity of energy distribution”, U. S. Patent 4144436, Mar. 13, 1979.

[94] L. L. Whiteley, “Electronic cooking appliance”, U. S. Patent 3746823, Jul. 17, 1973.

3 Simulation and measurement schemes

3.1 Overview

In this chapter, all the simulation and measurement scenarios are explained. Firstly, the measurements involved in the characterization of the coaxial-to-waveguide transitions are properly described, along with its applications to the characterization of a device under test and the modelling of printed circuit boards. Then, the simulation and measurements employed in the assessment of traditional corrugated filters are presented, along with some applications. Moreover, a new self-configurable multi-mode filter is also presented in this chapter.

3.2 Characterization of coaxial to waveguide transitions

In this thesis we present a new inverse characterization technique in order to evaluate coaxial-to-waveguide transitions [1]. This new unterminating procedure is carried out by minimizing the error between simulations of scattering matrix concatenations that contain the transition as an unknown parameter and measurements of several structures that reproduce the simulated scenarios. Two different standard types such as short-circuits and lines are used and two transitions are simultaneously characterized. The accuracy of the inverse technique is evaluated as a function of the employed standards, and the obtained results are compared to those provided by different well known calibration algorithms.

Fig. 3.1 shows the schemes of different experimental scenarios used to obtain the S parameters of the transition and their identifications. Let $s1$ be a short-circuit placed on the waveguide port of both transitions, and $s2$ and $s3$ short-circuits placed at 1.819 and 5.456 cm from that waveguide port, respectively. Additionally, let t be the thru connection between the two coaxial-to-waveguide transitions, and $l1$ and $l2$, 2 cm and 12.65 cm length WR-340 waveguide lines, respectively.

A Rohde & Schwarz ZVM Vector Network Analyzer has been used to measure the scattering matrix frequency behavior of the coaxial-to-waveguide transitions when

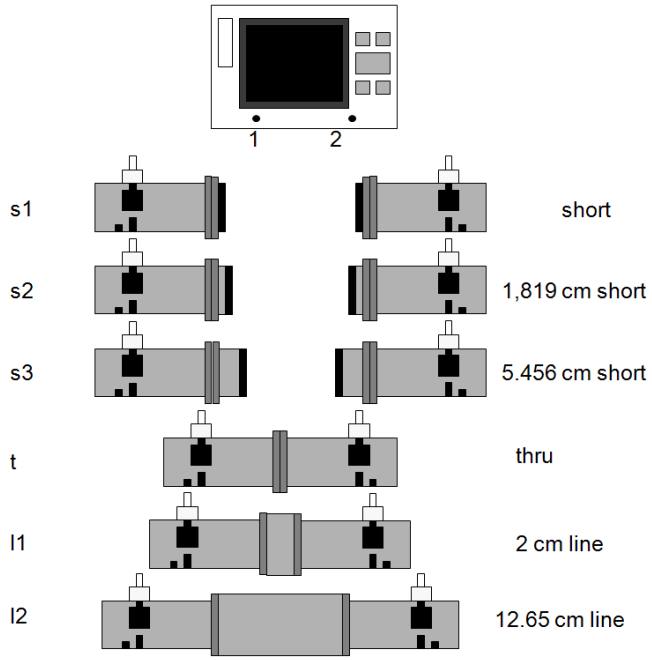

Figure 3.1: Scheme of different calibration standards used for inverse measurements.

using different standards. 1001 frequency points were collected in each measurement in the 2 to 3 GHz frequency range. Therefore, it was ensured that waveguide components worked only with the TE_{10} main mode.

A Rohde & Schwarz ZV-Z32 PC 3.5 fixed matched calibration kit was employed in order to calibrate the VNA at the port 1 of transition 1 and port 2 of transition 2. The coaxial-to-waveguide transitions that were used to carry out the study belong to a Continental Microwave WCK340-HP waveguide calibration kit [2].

3.2.1 Characterization of a device under test

In Fig. 3.2 a scheme of the WR-340 transitions under study and the device under test is depicted. The device under test consists of a 2 cm WR-340 waveguide holder whose cross section is completely filled with a 1.043 cm PTFE slab.

A Rohde & Schwarz ZVM Vector Network Analyzer has been used in order to measure the scattering matrix frequency behavior of the coaxial-to-waveguide transitions when using different standards. 601 frequency points were collected in each measurement in the 2.2-2.8 GHz frequency range. Therefore, it was ensured that WR-340 waveguide components worked only with the TE_{10} main mode. A Rohde & Schwarz ZV-Z32 PC 3.5 fixed matched calibration kit was employed in order to calibrate the VNA at the calibration plane shown in Fig. 3.2.

Several short-circuits and thrus with different lengths have been used in this work

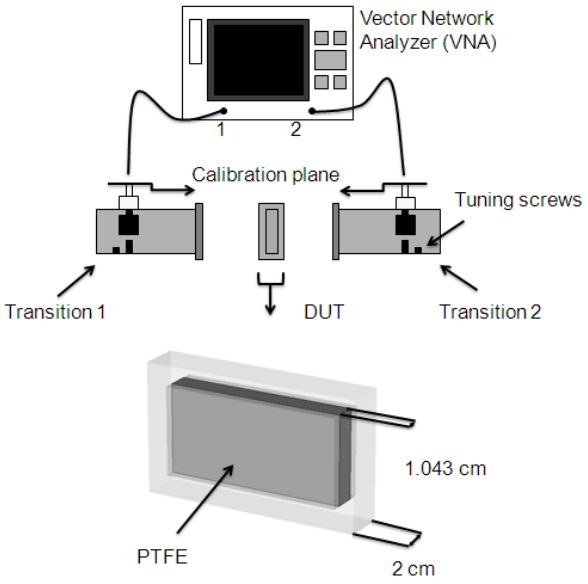

Figure 3.2: Coaxial-to-waveguide transitions and device under test.

during the two-tier calibration process. A diagram of all the employed standards during the extracting process can be seen in Fig. 3.3. Represented shorts for Port 1 have also been measured for Port 2. The connection of both standards' types to the coaxial-to-waveguide transition and to the device under test can be interpreted as a cascade of devices.

3.2.2 Modelling of printed circuit boards inside a metallic enclosure

The calibration measurements for the reflection behavior of each transition were performed by positioning a sliding shortplate at 1.25, 5 and 8.75 cm away from the reference plane of the virtual waveguide port of transition 1. The measurement of the whole empty enclosure, which implies the virtual 10 cm waveguide in between both transitions, was performed to define the thru behavior. The implemented method assumed a TE_{10} propagation mode.

The frequency range to carry out the PCB parameters optimization process was restricted to those frequencies near the first measured resonance since this resonance was found to occur at the monomode range.

A sweep algorithm was also evaluated with a set of 10 x 10 x 10 sampled points equally spaced within the range of [0.5, 30] mm for the thickness, [0, 0.3] S/m for the electrical conductivity and [1, 10] for the dielectric constant.

The employed aluminium enclosure had a $30 \times 12 \times 30$ cm^3 volume, the same used in [3] and [4]. The testing probes were 4 cm long monopoles placed at ± 7.5 cm away from the top centre of the cavity as depicted in Fig. 3.4.

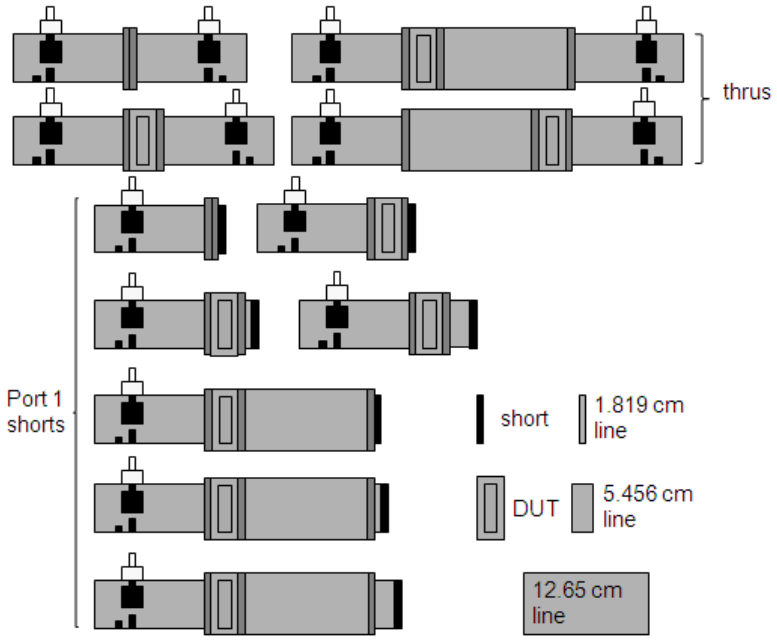

Figure 3.3: Thrus and shorts employed to obtain the coaxial-to-waveguide and DUT S-parameter matrices. Equivalent shorts have been used for port 2.

As said before, the analytic scattering matrix concatenation was implemented considering only monomode propagation. The first appearing mode for a 30×12 cm^2 waveguide cross section is the TE_{10} mode, which has a cut-off frequency of 500 MHz. The TE_{20} is the following mode that could be propagated through the waveguide once its evanescent condition is overcome, that is, for frequencies above 1GHz. Higher modes might appear starting from 1.249 GHz, which is the TE_{01} cut-off frequency. Therefore, by placing the monopoles just in the minimum of the TE_{20} E-field pattern, which means an alignment to the $x = 0$ plane, it was ensured a wide monomode bandwidth up to 1.249 GHz.

A commercial PCB was placed inside the enclosure in order to obtain $S_{ij}^{\prime m}$ as a function of frequency. The real PCB was introduced at the central part of the metallic enclosure with three different representative orientations as depicted in Fig. 3.5. The recorded measurements were used together with the corresponding simulation results $S_{ij}^{\prime s}$ for computing the evaluation fitting function in (2.26).

The real PCB dimensions were 12×6 cm^2 approximately (Fig. 2.8). The PCB was double layered with grounding planes and tracks on both sides of the PCB while the electronic components were soldered to just one side. It has to be remarked that the PCB was lightly populated. The PCB was unpowered thus acting as a passive load. It was considered that the geometrical centre of the PEC layer of the EM equivalent model had to be aligned with the y-axis in the centre of the enclosure. The same consideration was taken in the experimental setups having the PCB board substrate

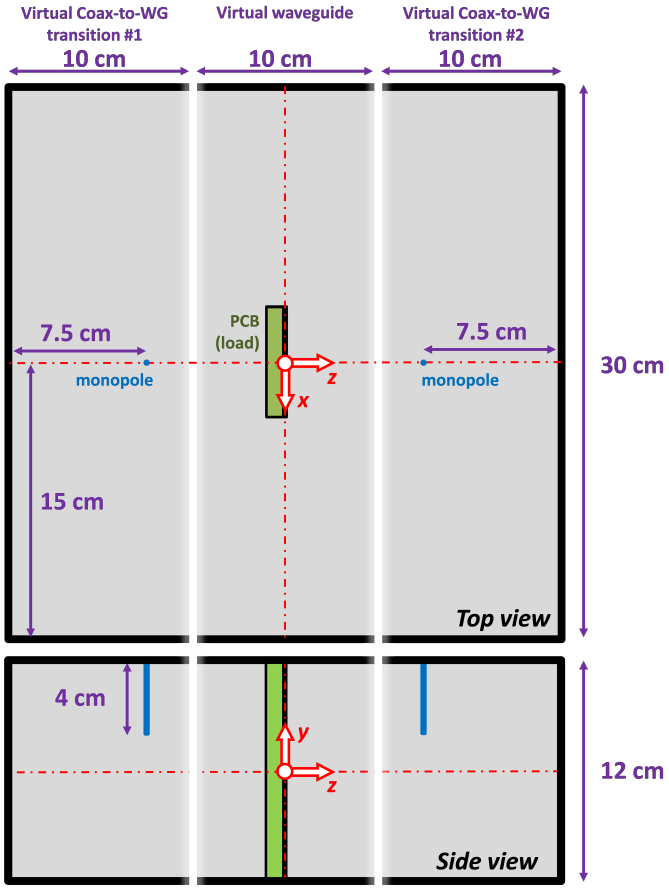

Figure 3.4: Schematic views of the virtual decomposition detailing the monopoles locations and the PCB positioning corresponding to the scenario (b).

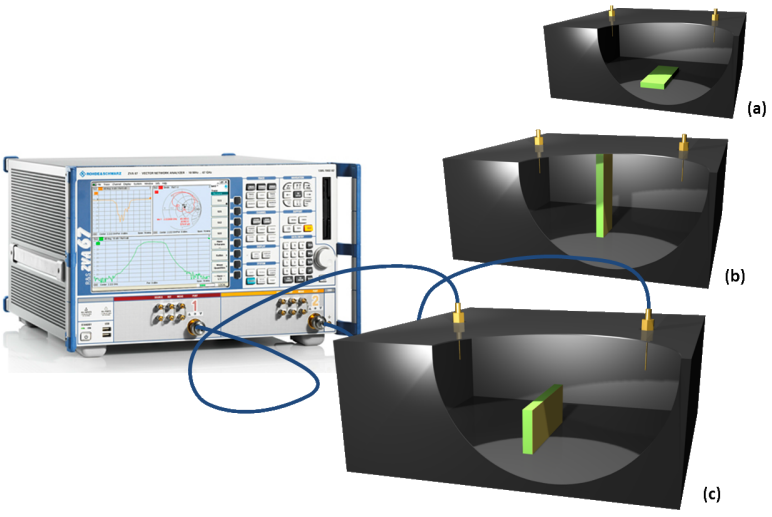

Figure 3.5: Measurement setup for the different PCB configurations evaluated within the enclosure.

as the alignment reference.

The scattering parameters were obtained by using a vector network analyser Rohde & Schwarz ZVA67. The frequency range for the experimental study ranged from 30 MHz to 2000 MHz. The amount of sampled frequency points was set to 1001; therefore a frequency resolution of 1.97 MHz was used during measurements.

3.3 Monomode filters

To begin with, the two different structures shown in Fig. 2.11 have been fully analyzed by using CST MICROWAVE STUDIO® software. First of all, some results have been obtained by varying the geometry and considering the filter without any material inside. Then, the following part is focused on studying these two structures when a piece of a material goes through the filter. The influence of the geometry of the filter and the relative electric permittivity of the material is studied by performing several parametric sweeps carried out by means of the simulation tool. In this way, it can be seen whether these corrugated bandstop filters are valid for any possible scenario, or there are limitations regarding the geometry or the dielectric properties of the sample. In addition, an optimization technique based on genetic algorithms has been applied in order to improve, if possible, the bandstop response of the filter in several problematic scenarios. Finally, the effect of combining the filter with a larger waveguide, representing a microwave heating cavity, is studied for different materials.

Once the limitations of traditional filters have been shown in simulation, some measurements have been carried out for both the doubly corrugated filter and a new proposed filter that solves these inconveniences.

3.3.1 Simulation procedures

The bandstop response of the filter is determined by both its geometry and the dielectric properties of the processed material. Therefore, these two features have been modified in order to extract their influence on the transmission coefficient of the filter. Regarding the characteristics of the filter, especially important are the height (sum of the height of the corrugations, d, and the height of the part where the material goes through, g), the width, w, and the number of sections of the filter. The rest of filter parameters can be seen in Fig. 2.11. The dielectric properties of the material are taken into account by means of the dielectric constant, ε', and the loss tangent, $\tan\delta$, as follows in (3.1), where the relative complex permittivity of the material, ε_r, is expressed in terms of these two parameters.

$$\varepsilon_r = \varepsilon' \left(1 - j \tan\delta\right) \tag{3.1}$$

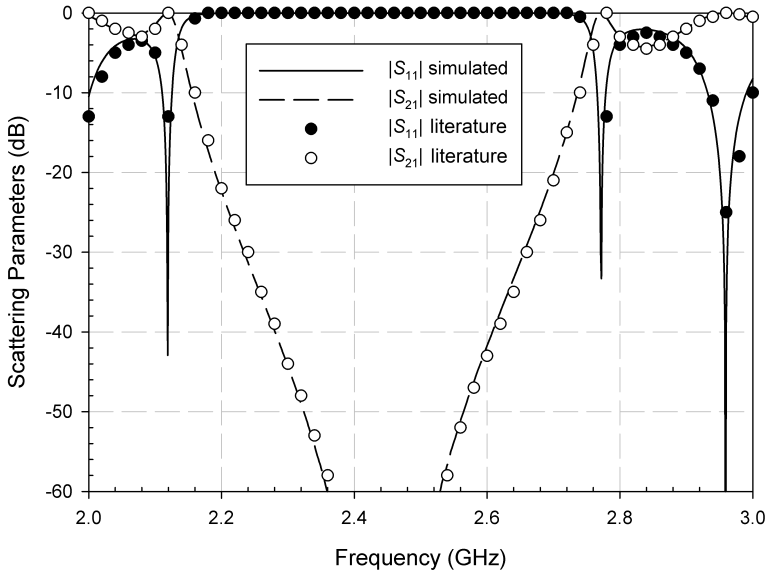

Figure 3.6: Comparison between simulation and results from [5] for the empty singly corrugated filter chosen as reference.

Singly corrugated filter		Doubly corrugated filter	
Sections	3	Blocks	3×4
g (cm)	2	g (cm)	2
d (cm)	4.164	d (cm)	2.839
w (cm)	8.636	w (cm)	8.636
l (cm)	4.846	l (cm)	2.879
b (cm)	2.4	b (cm)	1.6

Table 3.1: Geometry of the corrugated filters chosen as reference.

As it was explained before, waveguide bandstop filters for use in industrial microwave ovens are usually multimode structures with rectangular section. The cut-off frequency of a given mode is determined by both the open port dimensions and the dielectric properties of the materials placed inside the filter, and therefore the influence of these parameters is studied.

In order to verify the accuracy of the simulator results, exactly the same structures analyzed in [5] have been simulated, and results are shown in Fig. 3.6 and Fig. 3.7. The geometry of these structures is shown in Tab. 3.1 according to the parameters defined in Fig. 2.11. From these two figures it can be seen that the results offered by the simulator are fully reliable when analyzing this kind of waveguide bandstop filters, showing a good agreement between simulation and measurements.

Once the simulator has been properly validated, some modifications have been made

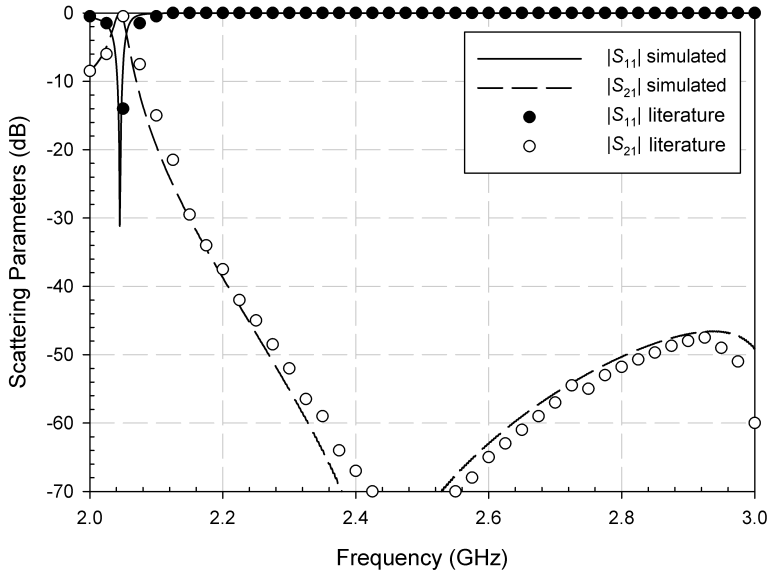

Figure 3.7: Comparison between simulation and results from [5] for the empty doubly corrugated filter chosen as reference.

on these reference structures regarding both the geometry and the dielectric properties of the processed sample. The performed work is divided into two parts: considering the filter independently and combining the filter with two larger waveguides placed at the filter ports. When simulating the filter independently two scenarios are considered: with and without a piece of material inside the filter. For the empty filter, the geometry has been modified in two different ways: by changing the width of the filter w, or the parameter g which determines the total height of the filter. In all these cases, the modifications have been made maintaining the symmetry and the periodicity of the structure. For example, the width of the doubly corrugated filter can only be increased in steps of b in order to allow the introduction of an entire metallic post.

On the other hand, the influence of the dielectric properties of the sample is obtained by varying both ε' and $\tan\delta$, as used in (3.1). When simulating the filter with a sample inside of it, this sample is placed as shown in Fig. 3.8. The width and height of the sample are w and g 3 mm respectively, leaving a small gap between the sample and the corrugations and completely filling the rest of the filter, which is a reasonably realistic scenario. When the filter is considered independently, it is not possible to simulate modes which are below cutoff according to the port dimensions but are propagating in the microwave heating cavity which the filter is connected to. In order to study if the filter is able to suppress these modes, two oversized waveguides are placed at the open ports as seen in Fig. 3.9. In this case, the oversized waveguide in port 2 is necessary to compute the propagation of higher order modes through the filter. This oversized port could represent other microwave-heating

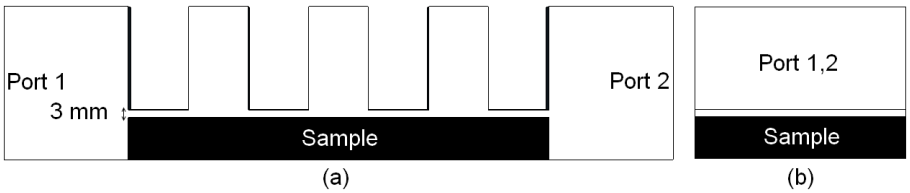

Figure 3.8: Singly corrugated filter design for simulation when a material is placed inside the filter. (a) Side view and (b) front view.

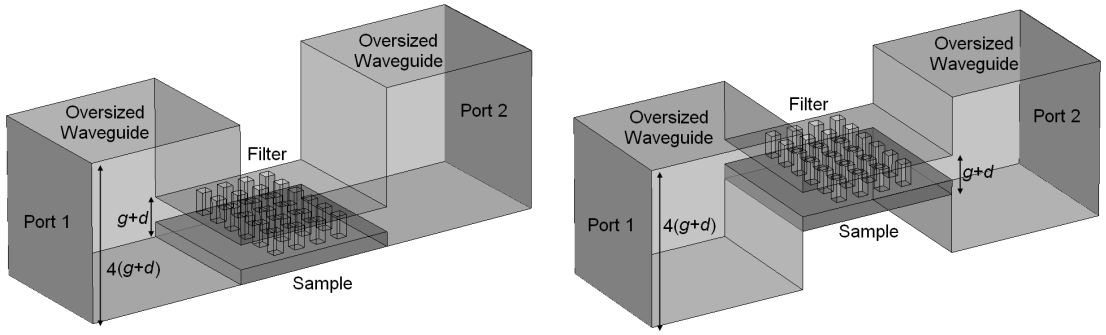

(a) Filter in the bottom **(b)** Filter in the middle

Figure 3.9: Combination of the doubly corrugated filter with the two oversized waveguides.

cavity module or even an estimation of how the filter would radiate these modes outside the oven. Simulations for several materials have been carried out for two different configurations, placing the filter in the bottom and in the middle of the oversized waveguides. In this way, two different incident electric field distributions are tested. For instance, the contribution of the incident TE_{01} mode is much bigger when the filter is located in the middle of the oversized waveguides.

All the simulations have been made by using the time domain solver on a frequency range from 2 to 3 GHz, pursuing to center the stopband at 2.45 GHz, where typical industrial magnetrons work. It must be pointed out that a perfect electric conductor background is considered. Since the considered filters are multimode structures, the magnitude of S_{21}^{ii} parameter is calculated for each propagating mode i with itself. Safe levels of radiation are guaranteed only if all the propagating modes are properly filtered. Attenuations around 60 dB are usually enough to ensure this. S_{21}^{ij} $(i \neq j)$ are not considered since most of them show attenuation values much higher than S_{21}^{ii}.

3.3.2 Optimization technique

Genetic algorithms have been employed to modify some design parameters in order to achieve, if possible, the goal of centering the stopband at 2.45 GHz, since modifi-

cations of the geometry of the filter or the dielectric properties of the sample might force a readjustment of some parameters of the filter.

Thus, an evaluation function F_i is defined for each mode i as the sum of differences between a given value of the S_{21}^{ii} parameter (if greater than -60 dB) and the value of -60 dB over a frequency range from 2.4 to 2.5 GHz.

$$F_i = \sum_j \left[\left| S_{21}^{ii}(f_j) \right| - (-60\text{dB}) \right], \ \forall j | \left| S_{21}^{ii}(f_j) \right| > -60\text{dB} \tag{3.2}$$

where $|S_{21}^{ii}|$ is the magnitude in dB of the forward transmission coefficient for the mode i with itself and j is the index for each frequency point within the optimized frequency range.

The final goal is to minimize the evaluation function F expressed as the sum of all the F_i corresponding to all the propagating modes.

$$F = \sum_i F_i \tag{3.3}$$

where i is the index of the considered mode. In this work the i index is ordered as a function of increasing cut-off frequencies, being $i = 1$ the index for the fundamental mode.

In this thesis the genetic algorithms tool implemented in Matlab® has been used. Regarding the genetic algorithms parameters, in this case 30 generations and 10 individuals per generation have been employed. Good convergence results have been obtained with this configuration, although depending on the number of optimized parameters these configuration parameters might be different. The mutation function adds a random number taken from a Gaussian distribution with mean 0 to each entry of the parent vector. The algorithm shrinks the variance in each coordinate linearly until it reaches 0 at the last generation.

3.3.3 Experimental setup

The structures under consideration are the doubly corrugated filter and the new proposed filter shown in Fig. 2.11b and Fig. 3.10, respectively. Both filters have been manufactured by using a WR-340 waveguide with a 8.64 cm × 4.32 cm cross section.

As it can be seen, there are many design parameters which determine the bandstop response. For instance, for the doubly corrugated filter shown in 2.11b the main design parameters are m and n, which represent the number of total posts, b and

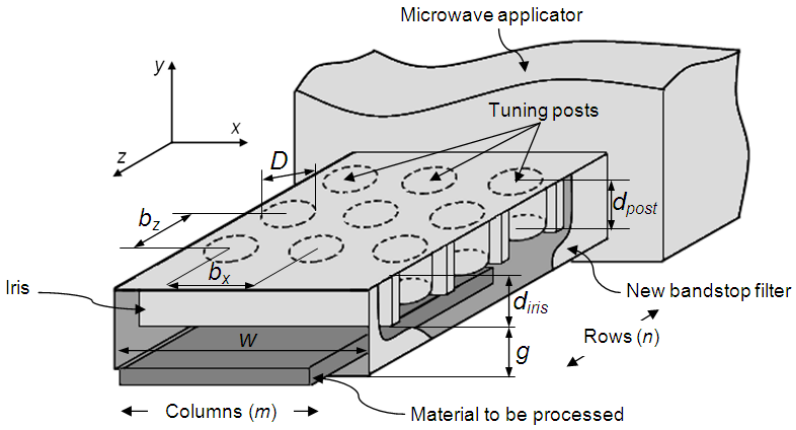

Figure 3.10: New proposed bandstop filter with irises and posts.

Parameter	Value
Posts ($m \times n$)	3×4
g (cm)	3.3069
d_{iris}(cm)	2.3
w (cm)	8.636
d_{post}(cm)	Tunable
D (cm)	1.2
b_x (cm)	2.867
b_z(cm)	3.225

Table 3.2: Optimized parameters for the manufactured filter with irises and posts when no material is inside.

l, which determine the size of the corrugations, d, which controls the height of the posts, g, which determines the height of the aperture where the material goes through, and w, which represents the width of the open port. Regarding the new filter shown in Fig. 3.10, the main design parameters are b_x and b_z, which control the separation between posts in the two directions x and z, D, the diameter of the posts, d_{post}, the height of each post, d_{iris}, the height of the metallic irises, and m, n, g and w as explained earlier. The thickness of the irises is 2 mm and they are placed exactly in the middle between the rows of posts. When optimizing this filter the parameters which are adjusted are g, D, d_{post} and d_{iris}.

In order to be able to measure the filter response easily, two monomode prototypes, which are shown in Fig. 3.11, have been manufactured. The geometry of both the doubly corrugated filter and the new filter is shown in Tab. 3.1 and Tab. 3.2, respectively, according to the parameters depicted in 2.11b and Fig. 3.10.

These prototypes are connected to a Rohde & Schwarz ZVA67 vector network analyzer by using a Continental Microwave WR-340 coaxial-to-waveguide transition as shown in Fig. 3.12. In this way, the S_{21} parameter is obtained, which according

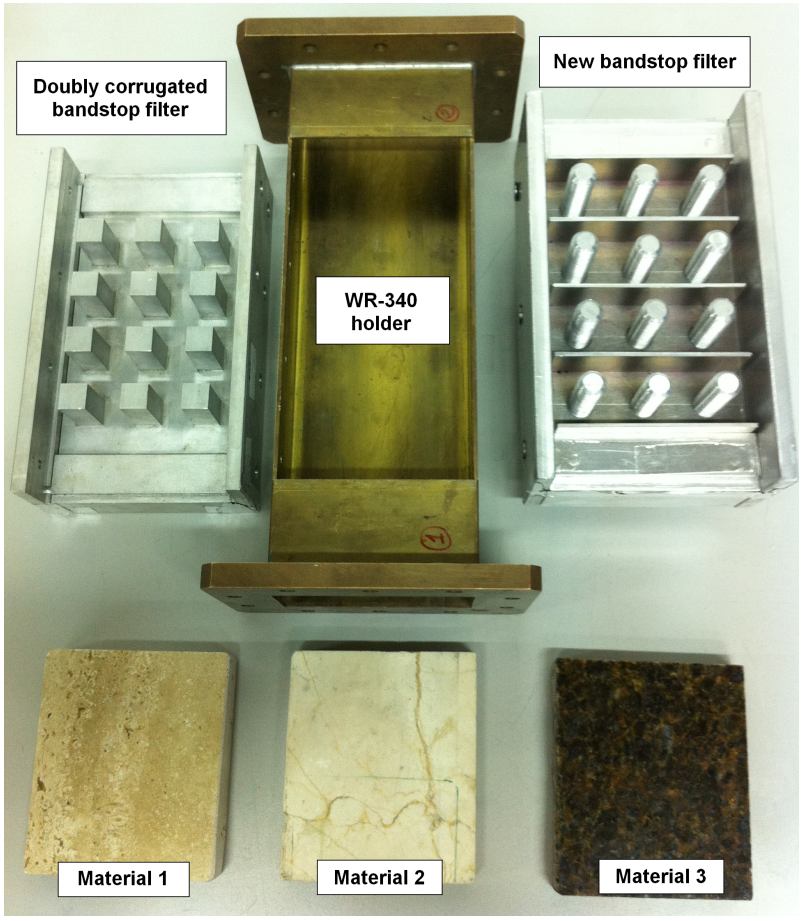

Figure 3.11: Manufactured prototypes and materials under test.

Material	Dielectric constant	Loss tangent	Dimensions (mm)
Material 1	$\varepsilon_1' = 7.90$	$\tan\delta_1 = 0.0440$	$86.1 \times 98.4 \times 19.7$
Material 2	$\varepsilon_2' = 8.18$	$\tan\delta_2 = 0.0196$	$85.9 \times 98.3 \times 19.9$
Material 3	$\varepsilon_3' = 5.49$	$\tan\delta_3 = 0.0581$	$85.8 \times 100.9 \times 20.1$

Table 3.3: Dielectric properties and dimensions of the three employed materials.

to [5] agrees with the filter response under open load conditions. The measurement has been performed by taking 1001 points from 2 to 3 GHz.

The behavior of the filters is also tested when a piece of a material is placed inside of them. Thus, three different pieces of marble and granite (see Fig. 3.11) with different dielectric properties are employed. The dielectric properties at 2.45 GHz and dimensions of these three materials are shown in Tab. 3.3.

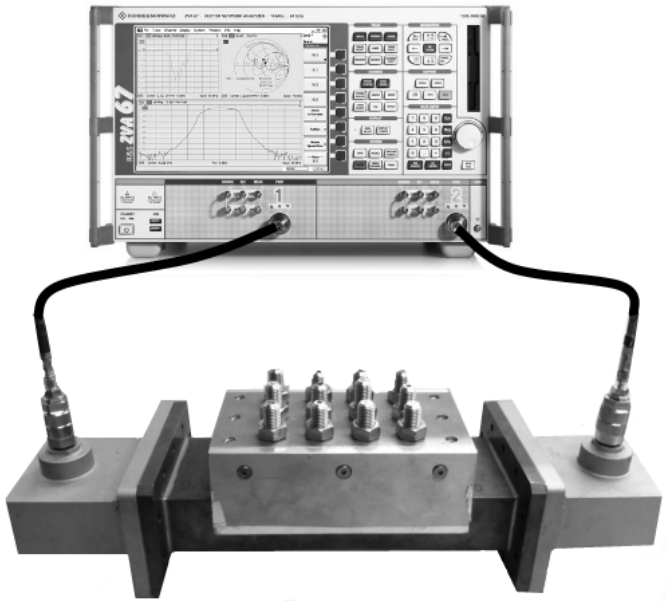

Figure 3.12: Experimental setup for S_{21} measurements.

3.4 Reduction of the crosscoupling in multifed multimode cavities

A multimode cavity with four waveguide feeds, arranged in two different ways, is analyzed by using CST MICROWAVE STUDIO® for different materials. The size of the simulated cavity is 33 cm × 33 cm × 65 cm which includes the metallic walls of 0.5 cm thickness as depicted in Fig. 3.13. The doubly corrugated filter, whose geometry is shown in Fig. 3.14, is designed as a bandstop filter centered at 2.45 GHz.

When the filter is used, it is placed in the middle of the cavity held by a metallic plate of 0.5 cm thickness. Four WR-340 waveguide feeds are placed in the upper side of the cavity according to the two different configurations shown in Fig. 3.13. It must be pointed out that these configurations are considered worst cases scenarios since there are ports that excite the same set of resonant modes due to the symmetry of the structures. Both the cavity and the filter are made of perfect electric conductor in order to simplify the model. Nevertheless, this is a good approximation for the materials commonly used in this kind of microwave applicators.

The sample is placed completely filling the bottom of the cavity with a height of 1.7 cm, leaving a small gap of 0.3 cm between the sample and the filter corrugations, which is a reasonably realistic scenario. The bandstop response of the doubly corrugated filter is influenced by the relative electric permittivity of the material to be processed, so three different values of dielectric constant, ε', and loss tangent, $\tan\delta$, have been used in simulations. These values, shown in Tab. 3.4, have been chosen according to some generic materials commonly treated with microwave energy, i.e.,

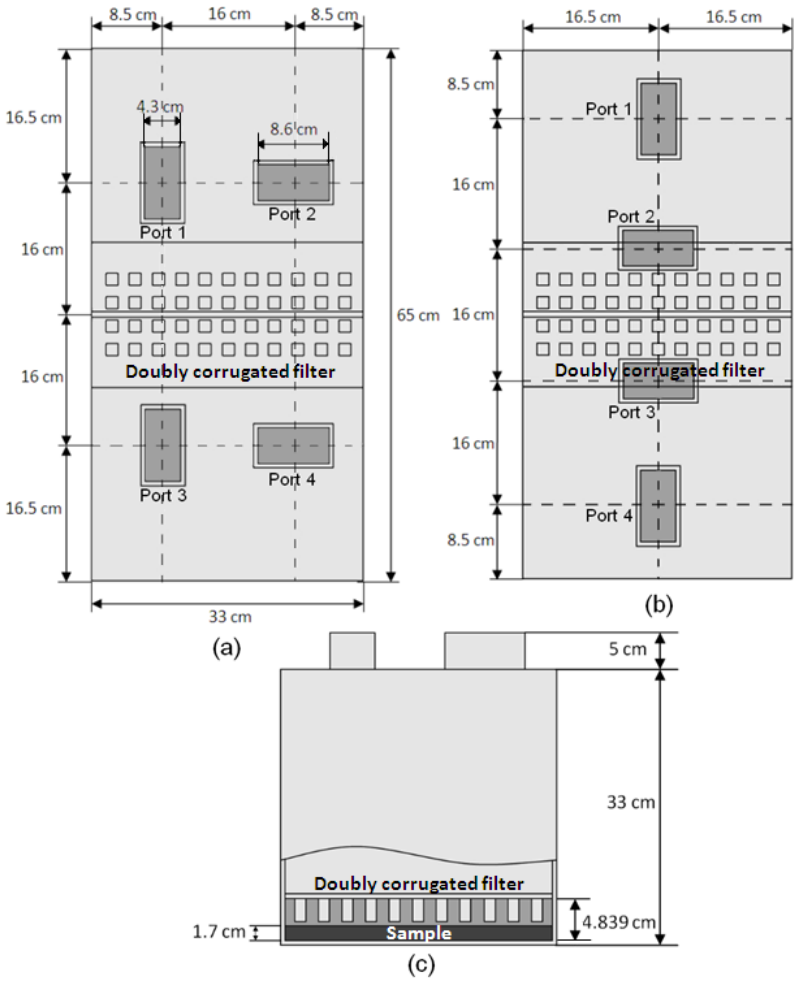

Figure 3.13: Simulated cavity. (a) Top view of the cavity for configuration no. 1. (b) Top view of the cavity for configuration no. 2. (c) Front view of the cavity with filter and sample details.

Dielectric properties	Material
$\varepsilon_1' = 2$, $\tan\delta_1 = 0.01$	Plastic
$\varepsilon_2' = 8.6$, $\tan\delta_2 = 6 \times 10^{-4}$	Marble
$\varepsilon_3' = 29.5$, $\tan\delta_3 = 0.2654$	Wet clay

Table 3.4: Dielectric properties of the three simulated materials.

plastic, marble or wet clay. All the simulations have been made by using the CST MICROWAVE STUDIO® time domain solver on a frequency range from 2 to 3 GHz. Only ports 1 and 2 need to be stimulated due to the symmetry of the structures. The scattering parameters have been obtained at 2.45 GHz, where typical industrial magnetrons work.

Finally, in order to quantify the total crosscoupling of a given configuration, two

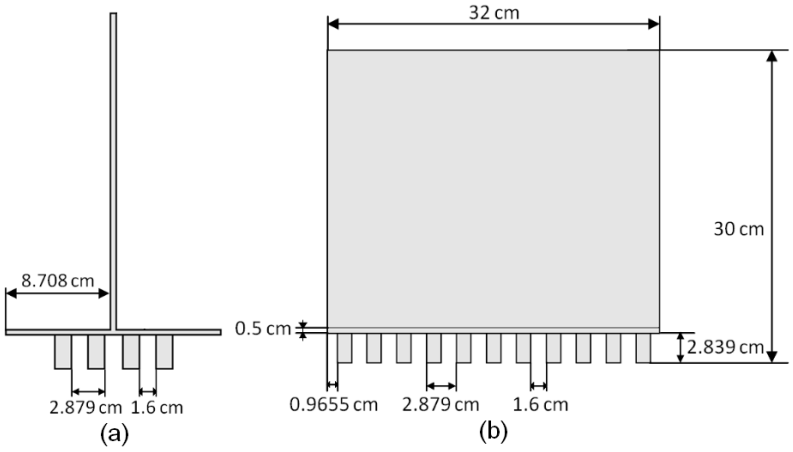

Figure 3.14: (a) Side view and (b) front view of the doubly corrugated filter which divides the cavity.

different functions f_1 and f_2 have been employed.

$$f_1 = |S_{21}|^2 + |S_{31}|^2 + |S_{41}|^2 \tag{3.4}$$

$$f_2 = |S_{12}|^2 + |S_{32}|^2 + |S_{42}|^2 \tag{3.5}$$

where S_{ij} represents the crosscoupling between the ports i and j and is expressed in linear units.

3.5 New self-configurable multimode filter

The manufactured prototype, which can be seen in Fig. 3.15 and Fig. 3.16, is a rectangular waveguide with cross section of 50 cm × 6 cm and length of 50 cm, which are plausible values for this kind of devices that deal with thin materials at the frequency of 2.45 GHz. This manufactured filter employs ten rows of metallic screws with diameter of 19.5 mm and ten screws per row. Attached to these metallic screws, ten stepper motors are used to screw on and off the metallic posts in a single row to the structure of the filter automatically. Fig. 3.17 shows the actual manufactured prototype along with a detailed view of the tunable screws. In addition, eleven metallic irises with width of 2.4 cm and thickness of 2 mm are placed in between the rows of posts. It must be remarked that with this configuration, only a row as a whole could be moved at each optimization step. The nomenclature of the rows (Rxy) and columns (Cxy) can be found in Fig. 3.16.

Thus, the parameters we are optimizing are the penetration of each post in the waveguide, which control the bandstop response of the filter for each scenario. Each post is optimized independently when optimizing a row configuration during genetic

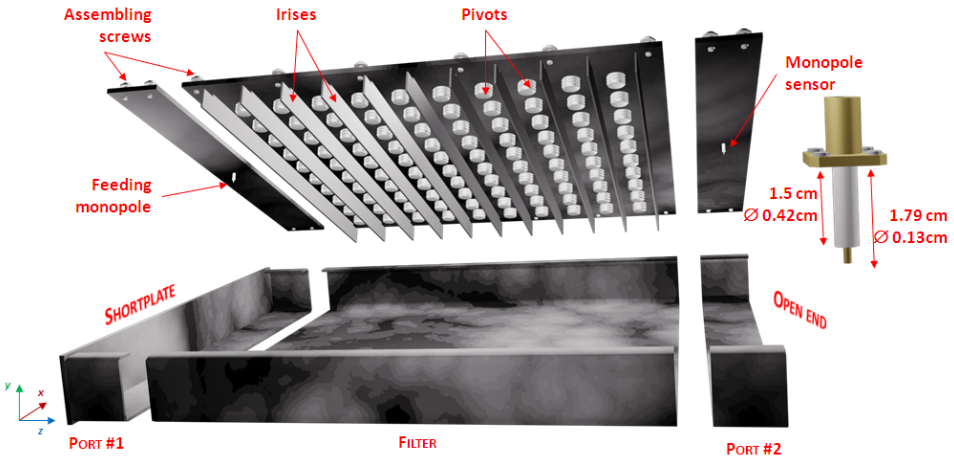

Figure 3.15: Exploded view of the new bandstop filter prototype with the monopole antenna used for excitation and sensing purposes.

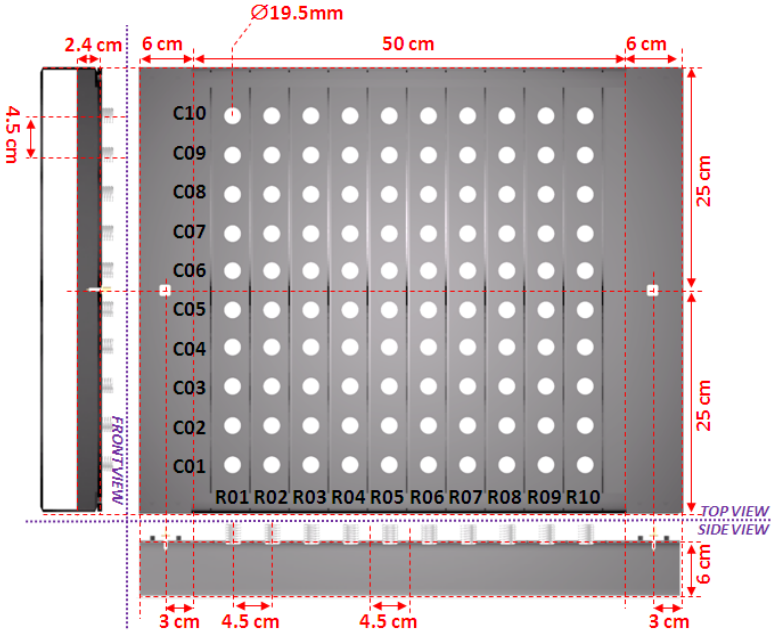

Figure 3.16: Dimensions of the new bandstop filter prototype.

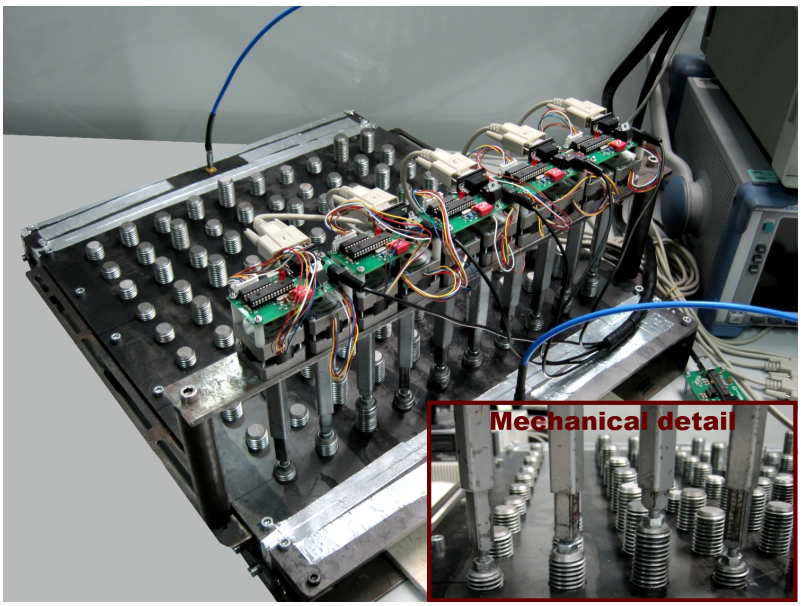

Figure 3.17: Actual manufactured prototype and mechanical detail of the tunable screws.

algorithms procedures. However, in the case of using a parametric sweep optimization strategy the penetration of all posts is the same within each row. Further details on this self-configuration and optimization process can be found in sec. 3.5.3.

3.5.1 Sensing and excitation systems

In order to obtain the performance of the filter it is necessary to measure the power level at the output port of the filter so that each configuration of the posts can be evaluated. Furthermore, in order to perform tests in a laboratory without using an actual industrial oven, it is necessary to feed the microwave power into the filter. In this way, a coaxial monopole antenna is employed for both purposes. Firstly, for the excitation of the filter a back-short waveguide with length of 6 cm and the same cross section as the filter is attached to the input port of the filter. The coaxial antenna is centered at the x-dimension of the filter on the top wall of the waveguide and 3 cm away from the shortplate, as depicted in Fig. 3.16, which corresponds to the position in which the generated progressive and regressive waves are in phase for the TE_{10} mode. Furthermore, placing the monopole in this position ensures that the TE_{10}, TE_{30}, TE_{50} and TE_{70} modes are excited since the antenna is placed at the maximum of the electric field distribution of these propagation modes. Fig. 3.18 shows the simulation scheme of the excitation system consisting of a multimode coaxial-to-waveguide transition. In this case, port one is placed at the coaxial probe connector whereas port two is placed at the waveguide cross-section that connects to the filter. According to the well-known cut-off frequency of a rectangular waveguide, only 8 modes could propagate at 2.45 GHz: TE_{10}, TE_{20}, TE_{30}, TE_{40}, TE_{50}, TE_{60},

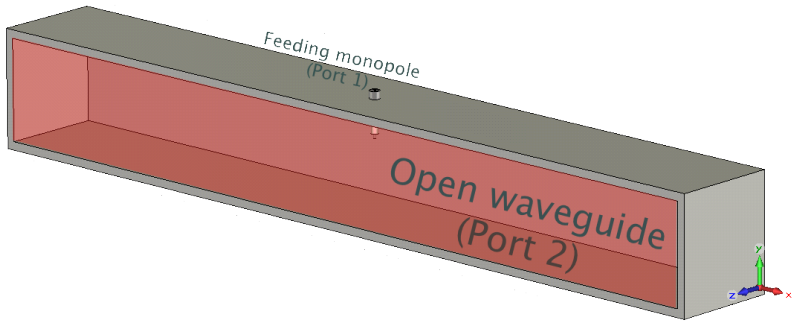

Figure 3.18: Simulation scheme of the coaxial-to-waveguide transition functioning as excitation system.

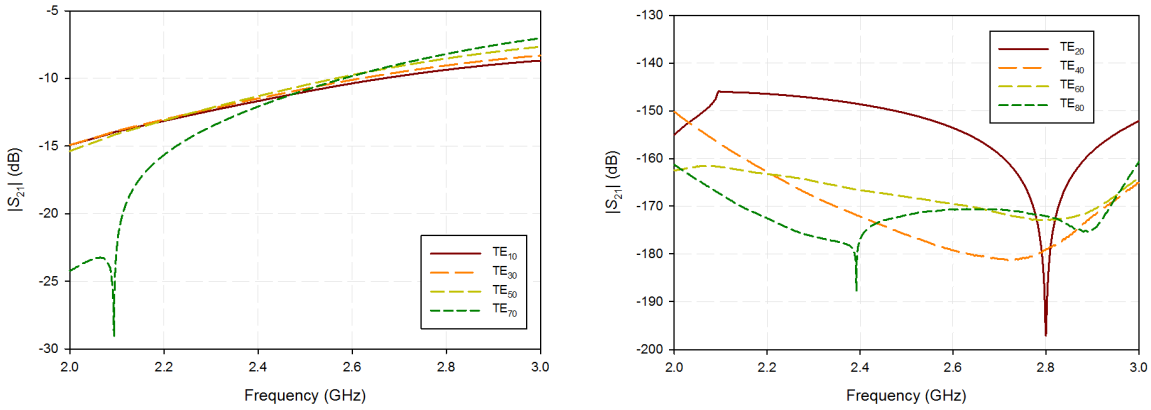

(a) Excited modes **(b)** Non-excited modes

Figure 3.19: Transmission coefficient in dB for all the modes above cut-off in the excitation transition.

TE_{70} and TE_{80}. Fig. 3.19 shows the transmission coefficient obtained for each mode when simulating the back-short waveguide excited by the coaxial monopole by means of CST MICROWAVE STUDIO® software. This transmission coefficient represents the power loss from the coaxial connector to the waveguide port of the transition for each mode. It is shown that all the excited modes, namely TE_{10}, TE_{30}, TE_{50} and TE_{70}, show similar amplitudes at the frequency of 2.45 GHz since the transmission coefficient is very similar for all of them. As expected, the TE modes with even indices TE_{20}, TE_{40}, TE_{60} and TE_{80} are not excited which is proven by the low transmission coefficient values provided by simulations.

For the laboratory tests an Agilent 8648C signal generator has been employed in order to feed the filter with a 2.45 GHz sine wave with power of 14.5 dBm. Since the filter under study is a passive device, its behavior will be quite similar when high power levels at industrial scale are employed. Nevertheless, it is true that several

phenomena such as arcing might occur [6] but this is something common to this kind of high power devices and not a particular issue of the proposed filter. Similarly, another 6 cm waveguide is placed at the output port of the filter. In this case the waveguide remains open, as in actual working conditions. The coaxial monopole, which in this case works as a sensor measuring the leaked power, is again centered on the top wall of the waveguide at a position which would correspond to the maximum of the electric field distribution of the TE_{10}, TE_{30}, TE_{50} and TE_{70} modes, as seen in Fig. 3.16. In this way, the filter will be able to deal with modes that have a maximum at that position ($TE_{(2k-1)0}$ modes, $k > 0$), but not with the rest of the modes. The value of the power at the output port of the filter obtained by the monopole is measured by means of a Rohde & Schwarz FSP7 spectrum analyzer.

3.5.2 Experimental setup

A general view of the whole system is depicted in Fig. 3.20a. The signal generator introduces the microwave energy in the filter through the coaxial monopole placed at its input port. Then, the microwave power travels through the filter to its output port, where it is measured by means of the coaxial monopole connected to the spectrum analyzer, which is plugged into a PC via GPIB. Thus, the computer has a measure of the performance of the filter configuration under evaluation, and will reconfigure the posts by using the stepper motors according to a given optimization scheme, which is discussed in the next section. This work flow is summarized in Fig. 3.20b. MATLAB® has been employed to control the whole process. The main objective of this sort of bandstop filters is to minimize the microwave power measured at the output port of the filter, or, what is the same thing, to maximize the attenuation (α) of the microwave power travelling through it. In order to calculate this attenuation, two different measurements have been performed. Firstly, the received power at the output port is measured (P_0) when using a hollow waveguide with the same length as the filter instead of using the filter. This value is compared to the received power measured when the filter is employed (P_{filter}), so the attenuation can be obtained according to the expression shown in (3.6).

$$\alpha\,(\text{dB}) = P_0\,(\text{dBm}) - P_{\text{filter}}\,(\text{dBm}) \tag{3.6}$$

When optimizing the filter, the power values are obtained at the single frequency of 2.45 GHz. Once the optimization procedure has been performed, a frequency sweep from 2.4 to 2.5 GHz has been carried out for the parametric sweep scenario in order to obtain the bandwidth of the filter.

3.5.3 Reconfiguration and optimization procedures

In order to reduce the microwave leakage when using these filters, two different procedures have been assessed: an optimization scheme based on genetic algorithms and an optimization procedure by using parametric sweeps.

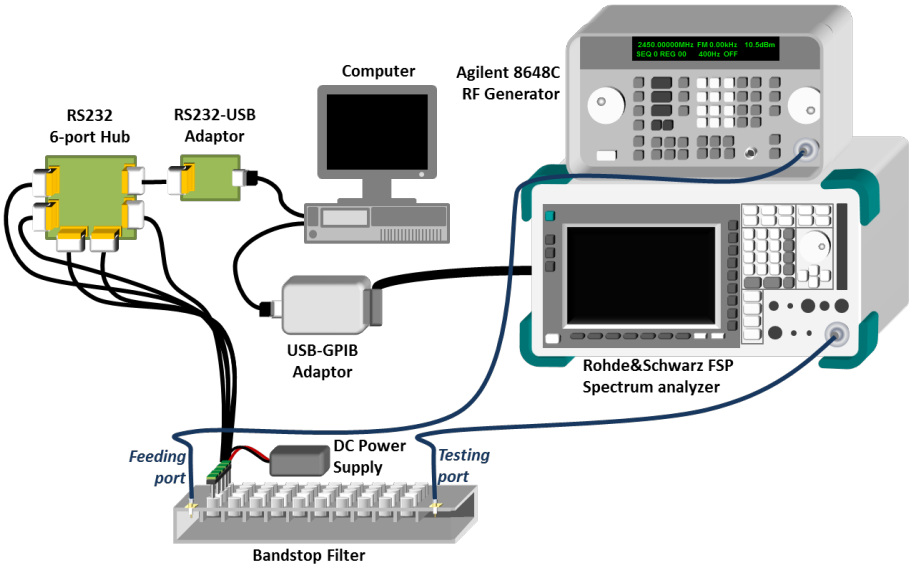

(a) General diagram

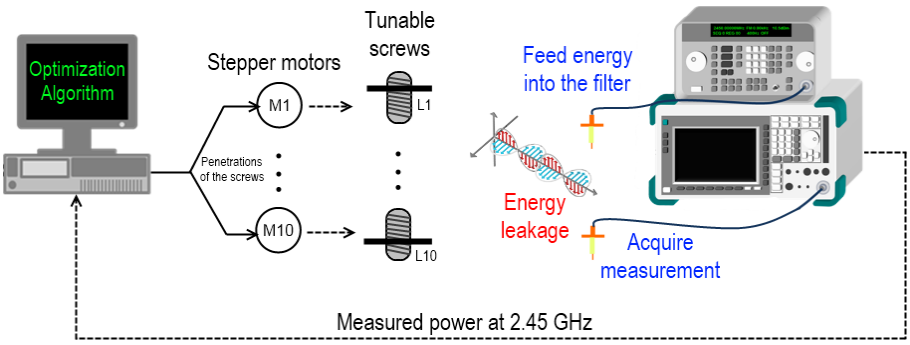

(b) Work flow

Figure 3.20: Experimental setup for measuring (a) and work flow for optimizing (b) the self-configurable bandstop filter.

3.5.3.1 Genetic algorithms

The optimization process when using GA is shown in Fig. 3.21. The process starts by placing the stepper motors at the first row. Then, the first individual generated by the GA is evaluated by measuring the received power at 2.45 GHz by the monopole antenna placed at the output port. It must be pointed out that each individual is represented by the different depths of the ten posts, i.e. a vector of ten values $\{p_1, \ldots, p_{10}\}$. Then, the performance of this individual is evaluated according to the fitness function in (3.7), which the algorithm tries to minimize, as follows:

$$f\left(p_1, \ldots, p_{10}\right) = P_{\text{measured}}\left(2.45\ \text{GHz}\right)\left[\text{W}\right] \tag{3.7}$$

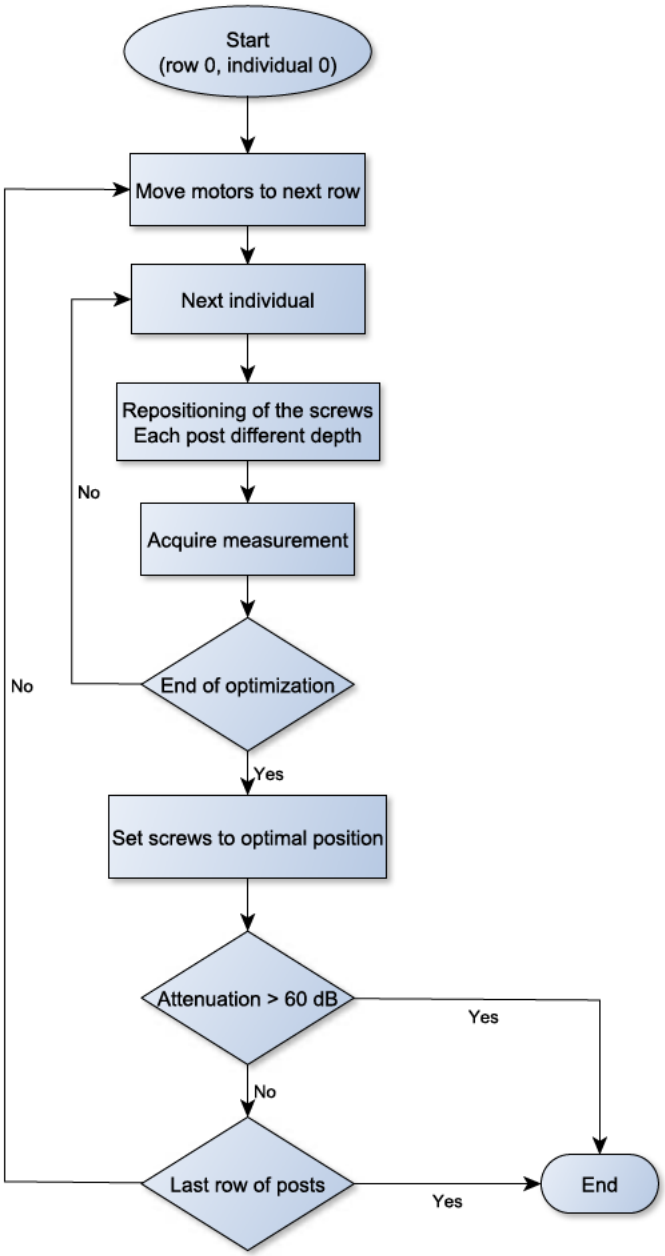

Figure 3.21: Flowchart of the genetic algorithm optimization.

where P_{measured} is the power in watts measured by the spectrum analyzer through the coaxial monopole at 2.45 GHz. This power is provided by the leakage of TE_{10}, TE_{30}, TE_{50} and TE_{70} modes at the output port as explained before. Thus, minimizing this power value ensures the reduction of the leakage of these modes.

In this case 10 generations and 10 individuals per generation have been employed. These values for the number of generations and the number of individuals per generation have been chosen after several trials as a trade-off between a good convergence

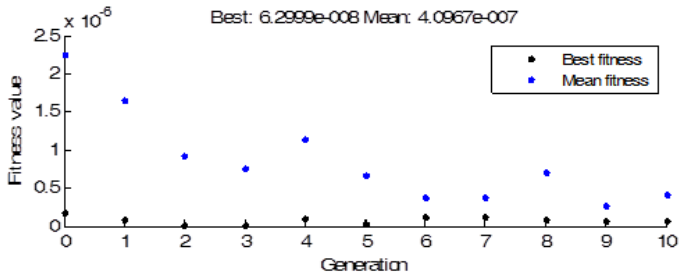

Figure 3.22: Example of optimization of one row by using genetic algorithms.

and a reasonable optimization time. Then, the rest of the individuals in a generation are evaluated and those that minimize the fitness function are taken into account to obtain the next generation by applying the crossover and mutation functions [7]. In order to provide genetic diversity from one generation to the next, especially in the first ones, the mutation function adds a random number taken from a Gaussian distribution with mean 0 to each entry of the parent vector. The algorithm shrinks the variance in each coordinate linearly until it reaches 0 at the last generation. In this way it is ensured a proper search for the solution during the first stages of the optimization and a refinement of the solution during the last stages of the process. The process goes on until the last generation is completed and the best individual is chosen. After this, the screws are set to the optimum position manually and the stepper motors are moved to the next row of posts. The optimization procedure is carried out again for this following row. The achieved attenuation is checked after the optimization of each row and the process is stopped if its value is greater than 60 dB, which is a good threshold value taking into account that values over 60 dB usually ensure a proper reduction of the leakage and guarantee a safe usage of the microwave oven. Fig. 3.22 represents an example of optimization of one row showing the best fitness and the mean fitness for each generation. It is shown how the algorithm converges to an optimum value in terms of minimum received power.

Moreover, two different initial alternatives when using GA have been assessed, i.e. starting the optimization process from the row nearest to the input port with all posts totally unscrewed (depth = 0 mm) or starting this optimization process with all posts almost totally screwed (depth = 28 mm), and then applying a complete GA optimization stage.

3.5.3.2 Parametric sweep

Secondly, once GA optimization has been evaluated, a procedure based on parametric sweeps has been applied. This procedure, whose flowchart is depicted in Fig. 3.23, is quite similar to the GA optimization although some important differences need to be considered. Again, the process is started by placing the stepper motors at the first row. In this case, and this is where the main difference lies in, all the posts in a given row are introduced the same depth in the filter. In this way, the depth of

Dielectric properties	Material
$\varepsilon'_1 = 2.55$, $\tan\delta_1 = 0.0063$	1
$\varepsilon'_2 = 9$, $\tan\delta_2 = 0.0244$	2
$\varepsilon'_3 = 40$, $\tan\delta_3 = 0.3$	3

Table 3.5: Dielectric properties of the three employed materials.

the posts is swept from 0 to 28 mm in steps of 0.5 mm and the best configuration in terms of minimum received power is chosen. Then, the stepper motors are moved to the next row and the process is repeated. Again, the process is stopped if the attenuation value is greater than 60 dB. As it can be easily deduced, the number of degrees of freedom when using the parametric sweep approach is less than the case when using GA, since all the post have the same depth. Therefore, in order to refine the results several consecutive parametric sweeps have been applied. The first one is started with all post unscrewed, whereas the following ones are started from the best solution obtained by the previous sweep.

3.6 Other analyzed structures

Apart from the reactive filters, several configurations for resistive filters implemented with water has been simulated with CST MICROWAVE STUDIO® [8]. This type of filters is generally employed to reduce the energy leakage by means of high dielectric losses when the attenuation achieved with the corrugated structures is not high enough.

3.6.1 Resistive filter with water cylinders

This type of filter is based on the use of cylinders made of a lossy material. In this case, distilled water has been employed, with a dielectric constant of 81 and an electric conductivity of 0.0001 S/m. The design parameters are the separation between cylinders, l, the diameter of the cylinders, D, and the distance from the top of the filter to the center of the cylinders, d, as depicted in Fig. 3.24. An optimization procedure of the empty filter has also been used to find the best configuration by varying l, d, D and the number of cylinders.

Results have been obtained for three different values of electric permittivity of the sample in order to assess the behavior of the filter when different materials usually treated by microwave energy are placed inside. These values are depicted in Tab. 3.5.

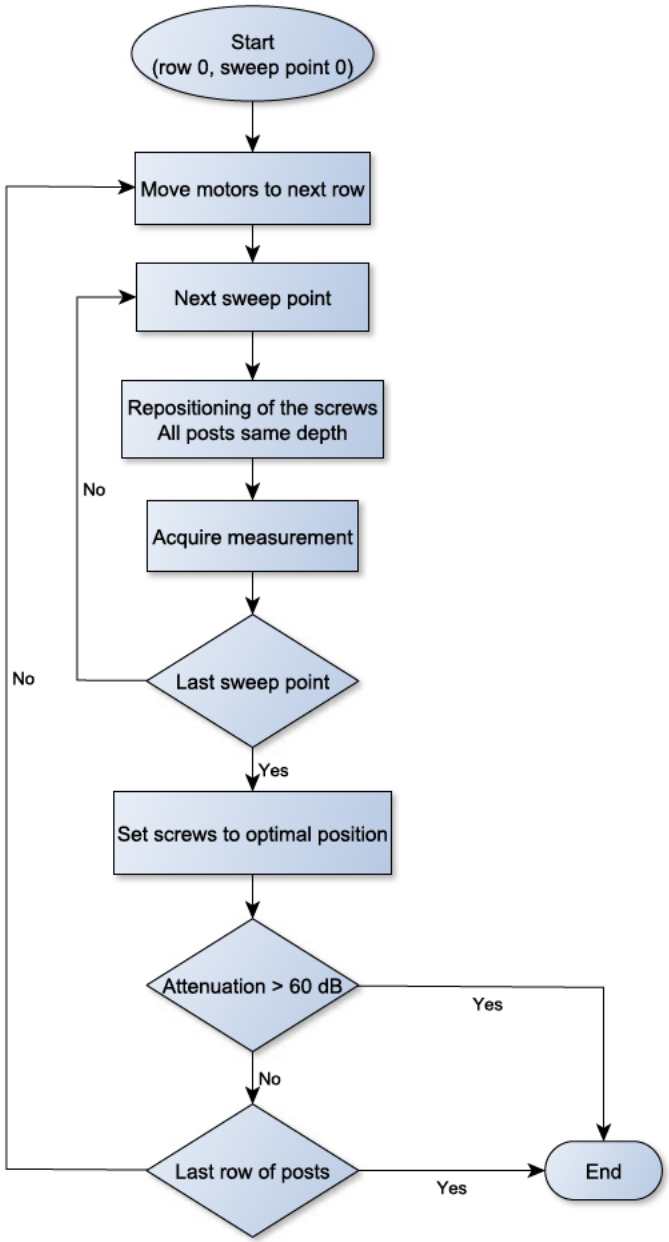

Figure 3.23: Flowchart of the parametric sweep stage.

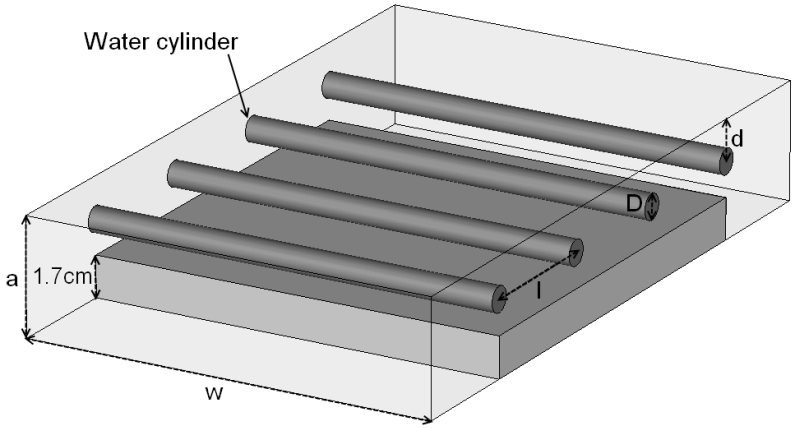

Figure 3.24: Resistive filter with water cylinders.

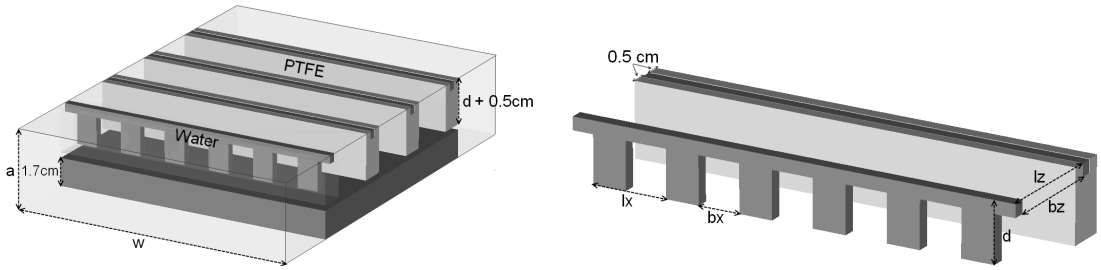

(a) Complete filter **(b)** Corrugations detail

Figure 3.25: Resistive filter with water and PTFE corrugations.

3.6.2 Resistive filter with water and PTFE corrugations

The other simulated configuration is based on a combination of water and PTFE corrugations as depicted in Fig. 3.25. As it can be seen from this figure, several PTFE simple corrugations are filled with distilled water posts. In this case the geometric parameters to be optimized are lz and bz, which determine the width of the corrugations and the separation between them, and d, the length of the water posts.

Also in this case, results have been obtained for the three different samples depicted in Tab. 3.5.

3.7 Mutual influence between cavity and filter

In general, when designing this kind of filtering structures, they are usually designed and validated without taking into account the influence of connecting the filter to the microwave applicator. The performance of the filter might be changed in that

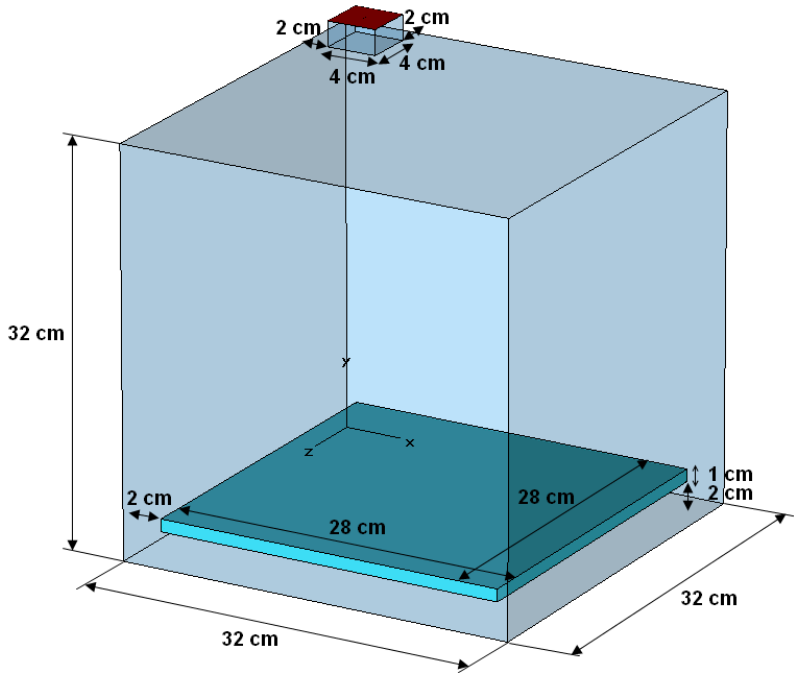

Figure 3.26: Model of the simulated heating cavity.

case, so there is a need for studying this effect. Therefore, in this thesis a doubly corrugated filter is analyzed and then connected to a microwave heating cavity with different materials inside of it. Several simulations by means of CST MICROWAVE STUDIO have been carried out to evaluate both the filter and the cavity together and separately for different processed materials.

The simulated multimode microwave cavity is shown in Fig. 3.26. It contains the processed material near the bottom wall. The doubly corrugated filter employed in this work is based on the device proposed in [5] but increasing the width of the open port and the length of the waveguide in order to adapt it to the dimensions of the studied heating cavity. A scheme of the doubly corrugated filter is shown in Fig. 3.27. Finally, the third simulation scheme consists of connecting the filter to one of the side walls of the cavity as shown in Fig. 3.28.

The scattering parameters of interest are the S_{11}^{11} parameter when simulating the heating cavity separately; and the S_{21}^{ij} parameter when simulating only the filter, which determines its attenuation. In this last case i represents the mode considered at the output port and j the mode excited at port 1 of the filter.

When simulating the whole system the scattering parameters which need to be taken into account are again the S_{11}^{11} parameter and the S_{21}^{i1} parameter which in this case determines the attenuation from the excitation port on the top of the cavity to the open port of the filter. Again in this case, i represents the different propagating modes at port 2, ordered as a function of increasing cut-off frequencies.

All the simulations have been performed on a frequency range from 2 to 3 GHz.

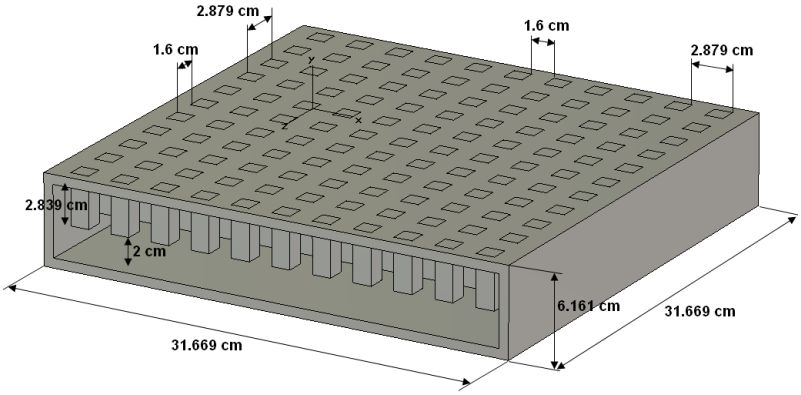

Figure 3.27: Model of the simulated doubly corrugated filter.

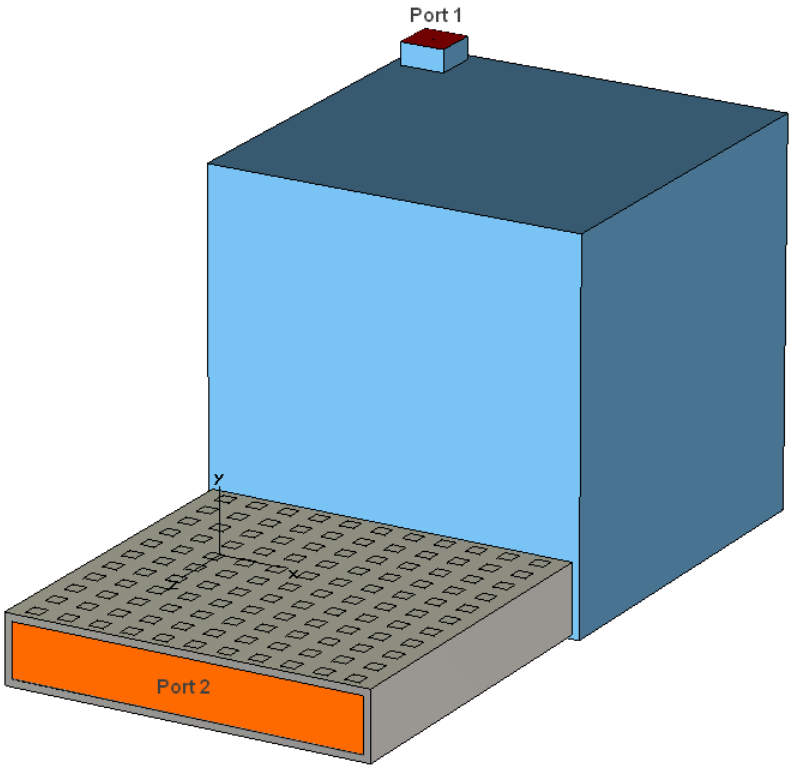

Figure 3.28: Model of the simulated whole system with cavity and filter.

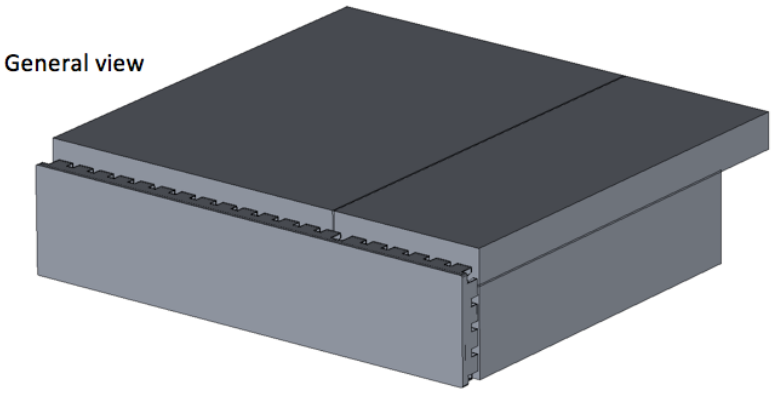

Figure 3.29: General view of the compact microwave oven for catering purposes.

3.8 Compact microwave oven with hot and cold compartments

As it was stated in sec. 2.7.1, a compact and very flat microwave-heating oven for catering purposes comprising an upper multimode cavity with radiating slots that feed the microwave energy into a lower cavity has been developed in this thesis and patented.

The invention concerns a compact microwave oven for selectively heating of meals. More particularly, it concerns a microwave oven provided with a cavity, enclosed by walls wherein a dish with food, such as for catering services, can be inserted and wherein the space between the dish and the walls is substantially limited. Furthermore, the device enables selectively heating a part of the dish. The microwave oven comprises a warm and cold compartment and means to manage efficiently the microwaves in the hot compartment in respect with the food compounds.

Some images representing the final design of the oven are shown in Fig. 3.29 to Fig. 3.33. In particular, Fig. 3.30 shows 3 tuning screws which have been included to slightly modify the matching of the cavity if necessary in order to obtain good power efficiency at 2.45 GHz. Fig. 3.31 shows a view of the interior of the cavity, with the 'door-like' filter that divides the cavity into the two compartments, and a mode stirrer which rotates in order to modify the electric field distribution and improve the heating uniformity. In Fig. 3.32 it is depicted a detail of the microwave door, very similar to a domestic one, but taking into account the two different compartments. And finally, in Fig. 3.33 the feeding system based on radiating slots is shown along with the position of the magnetron antenna. The dimensions and positions of the slots have been optimized in order to obtain both good matching and uniform heating. No further specific details are given due to confidentiality issues. In Fig. 3.34 to Fig. 3.36 several pictures of the manufactured prototype, which is currently under development and testing, are shown.

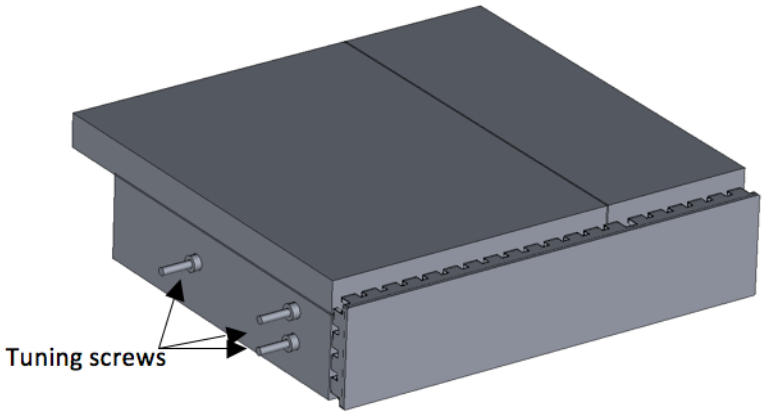

Figure 3.30: Tuning screws to control the matching.

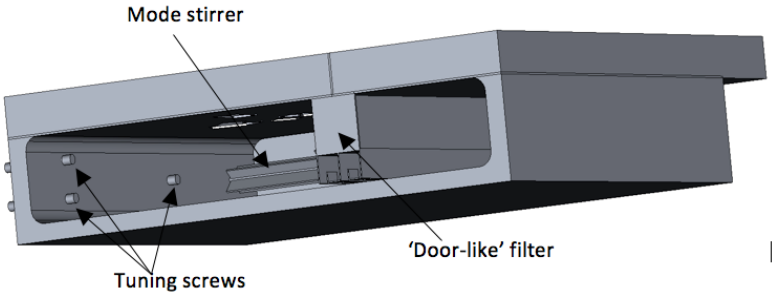

Figure 3.31: Interior view of the compact microwave oven for catering purposes.

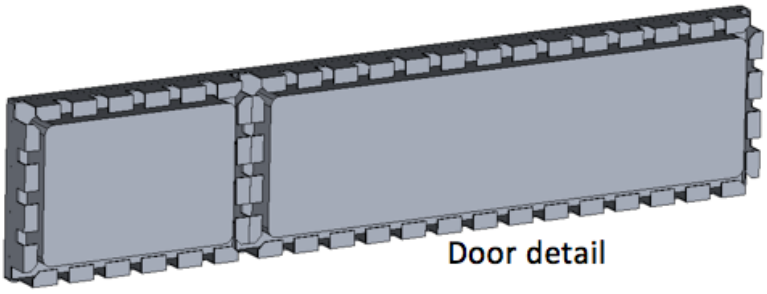

Figure 3.32: Detail of the door for the compact microwave oven.

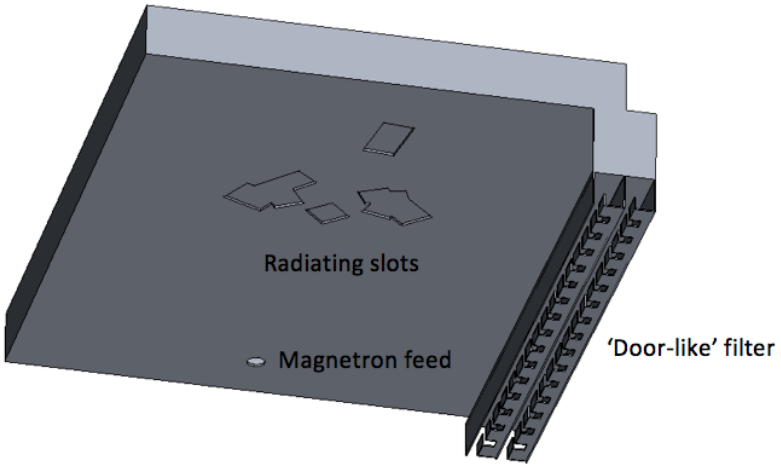

Figure 3.33: Feeding system and detail of the 'door-like' filter.

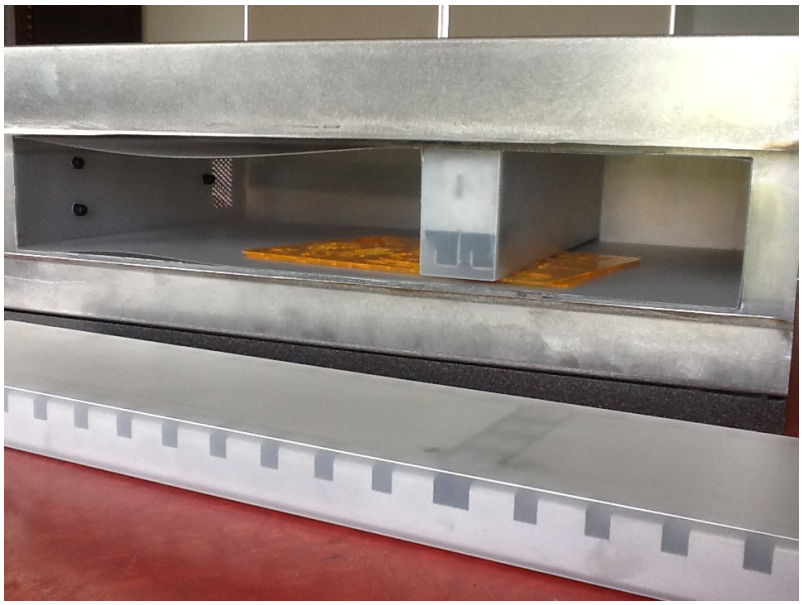

Figure 3.34: Interior view of the manufactured prototype.

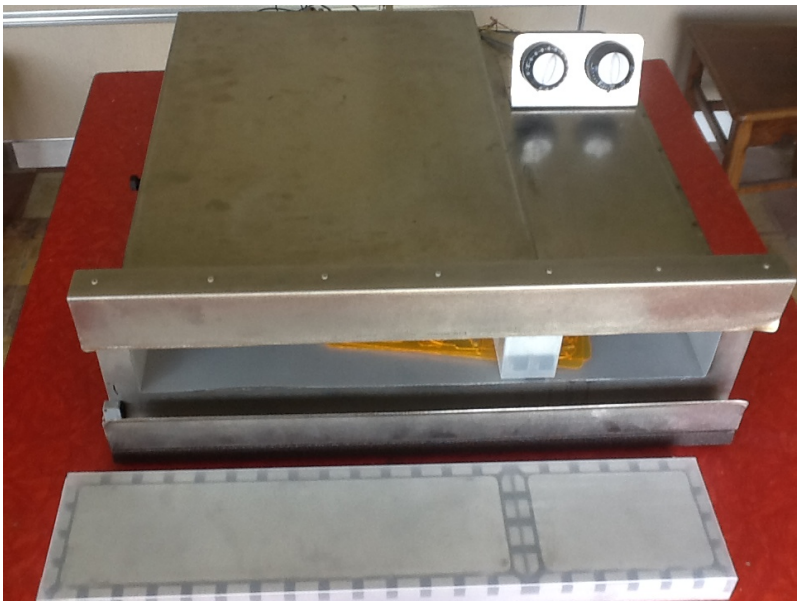

Figure 3.35: General view of the manufactured prototype, with detail of the door.

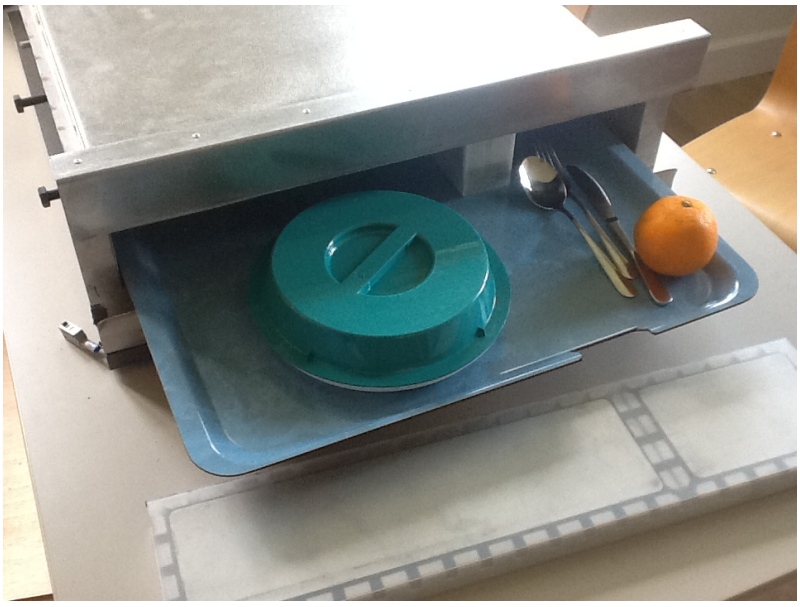

Figure 3.36: General view of the manufactured prototype, with a food tray.

Bibliography

[1] A. J. Lozano-Guerrero, F. J. Clemente-Fernandez, J. Monzó-Cabrera, J. L. Pedreño-Molina and A. Díaz-Morcillo, "Precise evaluation of coaxial to waveguide transitions by means of inverse techniques", IEEE Trans. Microw. Theory Tech., vol.58, no.1, pp.229-235, Jan. 2010.

[2] Waveguide Component Specifications and Design Handbook. Edition #7. Continental Microwave Division.

[3] D. W. P. Thomas, A. C. Denton, T. Konefal, T. Benson, C. Christopoulos, J. F. Dawson, A. Marvin and S. J. Porter, "Characterisation of the shielding effectiveness of loaded equipment enclosures", International Conference and Exhibition on Electromagnetic Compatibility, pp. 89 94. July 1999.

[4] D. W. P. Thomas, A. C. Denton, T. Konefal, T. Benson, C. Christopoulos, J. F. Dawson, A. Marvin, S. J. Porter, and P. Sewell, "Model of the electromagnetic fields inside a cuboidal enclosure populated with conducting planes o printed circuit boards", IEEE Trans. on Electromagn. Compat., vol. 43, no. 2, pp. 161 169, May 2001.

[5] P. Soto, V. E. Boria, J. M. Catalá-Civera, N. Chouaib, M. Guglielmi and B. Gimeno, "Analysis, design, and experimental verification of microwave filters for safety issues in open-ended waveguide systems", IEEE Trans. Microw. Theory Tech., vol. 48, no. 11, pp. 2133-2140, Nov. 2010.

[6] V. Bilik and J. Bezek, "High power limits of waveguide stub tuners", J. Microw. Power Electromagn. Energy, vol. 44, no. 4, pp. 178-86, 2010.

[7] Y. Rahmat-Samii and E. Michielsen, Electromagnetic Optimization by Genetic Algorithms. New York: John Wiley & Sons, 1999.

[8] F. J. Clemente-Fernández, J. Monzó-Cabrera, J. L. Pedreño-Molina, A. J. Lozano-Guerrero and A. Díaz-Morcillo, "Analysis of reactive and resistive open waveguide filters for use in microwave-heating applicators", COMPEL: The International Journal for Computation and Mathematics in Electrical and Electronic Engineering, vol. 30, no. 5, pp. 1606-1615, Oct. 2011.

4 Evaluation of waveguide bandstop filters for microwave-heating ovens

4.1 Overview

In this chapter, both traditional and new waveguide bandstop filters for use in industrial microwave-heating ovens are assessed.

Firstly, the limitations of traditional reactive filters, i.e. singly and doubly corrugated filters, are shown, regarding both the geometry and the dielectric properties of the processed material. These constraints are confirmed with simulations and measurements. Additionally, some alternatives based on resistive filters are also evaluated. Then, a new proposed filter based on irises and metallic posts is properly analyzed and validated. Several applications of waveguide bandstop filters, such as the reduction of the crosscoupling or the separation into hot and cold compartments in a heating cavity, are studied next, along with an important issue such as the mutual influence between cavity and filter. Finally, a new self-configurable multimode filter based on irises an automatically tunable posts is presented and properly validated.

4.2 Limitations of traditional filters

4.2.1 Singly corrugated filters

In sec. 3.3 it was described the procedure to assess the behaviour of the singly corrugated filter introduced in sec. 2.6.

First of all, a sweep for different values of the width of the filter, w, is carried out when considering an empty filter such as the one depicted in 2.11a. The rest of parameters in Tab. 3.1 are not modified. Obtained results are depicted in Fig. 4.1, showing the attenuation of the filter at 2.45 GHz for each propagating mode. Modes different from the fundamental mode TE_{10} are depicted from where they actually begin to propagate at 2.45 GHz according to the cutoff frequency of the open waveguide port.

From these results it can be observed that these singly corrugated structures properly filter one mode at the same time, either the TE_{10} mode when simulating the

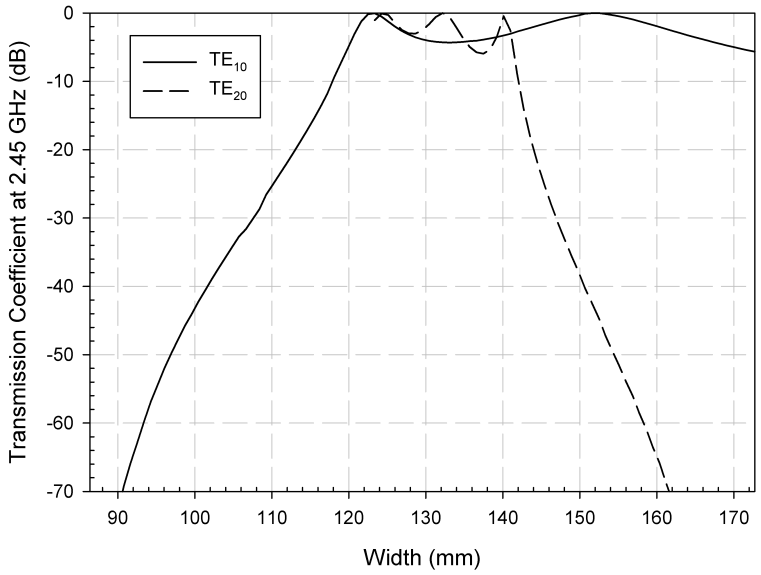

Figure 4.1: Transmission coefficient in dB at 2.45 GHz when varying the width of the singly corrugated filter for TE_{10} and TE_{20} modes.

reference filter or the TE_{20} mode when the width is doubled. Further non-parametric simulations have been performed, for example quadrupling the width of the filter. In that case, only the TE_{40} mode is suppressed. Therefore, one can deduce that singly corrugated filters can only eliminate one mode. This fact is an important limitation of these filters, since typical industrial applications usually require multimode structures due to the size of the sample to be treated.

Regarding modifications of the filter height, a new parametric sweep is performed by varying the parameter g of the reference singly corrugated filter. Results for the magnitude of the transmission coefficient at 2.45 GHz are shown in Fig. 4.2. It can be seen that increasing the height of the port causes a similar attenuation decrease of both TE_{10} and TE_{01} modes. The main difference is that the magnitude of the transmission coefficient for the TE_{01} mode starts from lower levels than those for the TE_{10} mode due to the higher cutoff frequency of the TE_{01} mode in this case. Moreover, TE_{11} and TM_{11} modes, which appear from a height of around 87 mm, are not properly filtered either.

Finally, the last simulation for the singly corrugated filters analyses the influence of the dielectric properties of the sample on the bandstop response of the filter. Thus, three different values of the relative permittivity of the sample have been simulated and its results for the TE_{10} mode are depicted in Fig. 4.3. The sample has been placed inside the reference singly corrugated filter according to the geometry shown in Fig. 3.8.

Results show that a sample of $\varepsilon_{r1} = 2 - j0.05$, representing plastic, does not have an

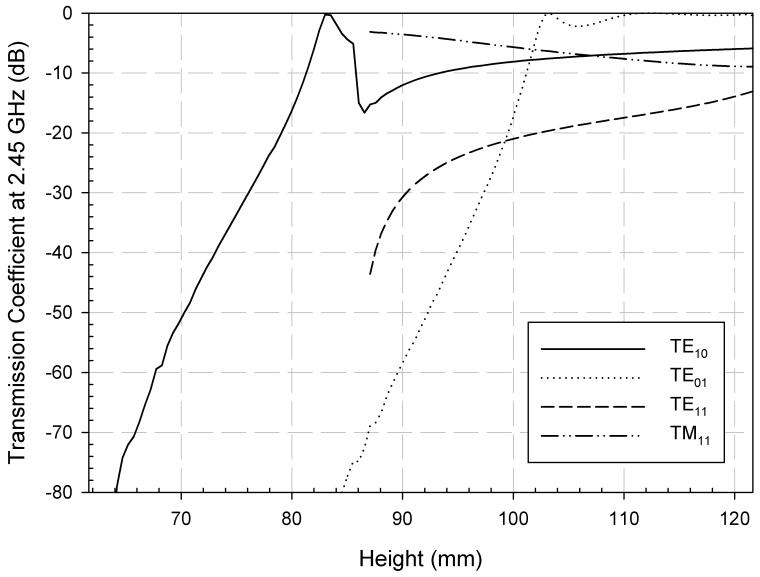

Figure 4.2: Transmission coefficient in dB at 2.45 GHz when varying the height of the doubly corrugated filter for different modes.

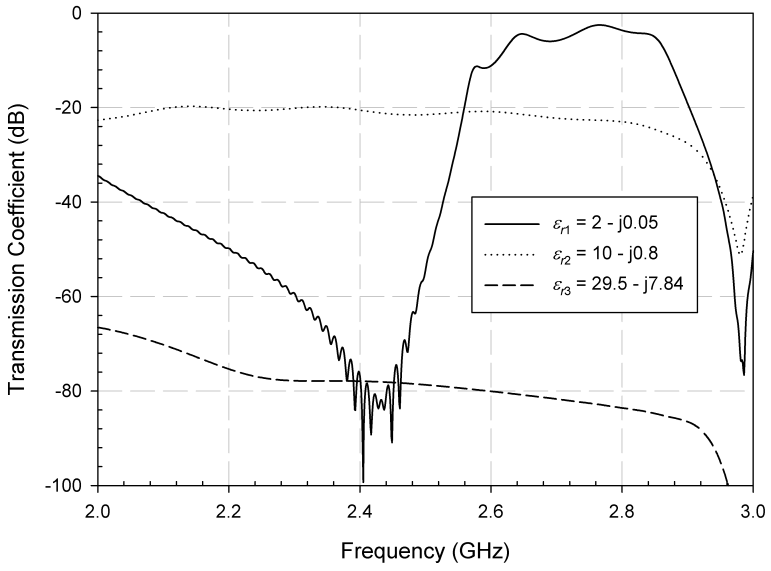

Figure 4.3: Transmission coefficient in dB at 2.45 GHz for three different values of the relative permittivity of the sample for the singly corrugated filter and the TE_{10} mode.

Width (mm) / Mode	TE_{10}	TE_{20}	TE_{30}	TE_{40}	TE_{50}
86.36	-83.48	-	-	-	-
115.15	-71.78	-	-	-	-
143.94	-65.96	-60.75	-	-	-
172.73	-60.93	-71.40	-	-	-
201.52	-59.64	-67.75	-70.65	-	-
230.31	-58.74	-65.39	-82.05	-	-
259.10	-58.14	-63.68	-71.32	-66.50	-
287.89	-58.23	-62.58	-68.77	-72.76	-
316.68	-57.78	-61.57	-66.93	-83.56	-70.28
345.47	-57.32	-60.77	-65.50	-70.99	-62.42

Table 4.1: $|S_{21}|$ in dB at 2.45 GHz when varying the width of the empty doubly corrugated filter. Rest of parameters are shown in Tab. 3.1.

important influence on the response of the filter and therefore this mode is properly filtered. When the permittivity is $\varepsilon_{r2} = 10 - j0.8$, a value near marble and some ceramic permittivities, the mode shows a plain attenuation of around 20 dB, not suitable for a safe use. The third value of permittivity, $\varepsilon_{r3} = 29.5 - j7.84$, corresponding to wet clay, shows a good attenuation, due to high dielectric losses. A much more detailed study of the influence of the relative permittivity of the sample is performed for the doubly corrugated filter, which is the filter used in practical applications due to its advantages compared to singly corrugated filters.

4.2.2 Doubly corrugated filters

Similarly to the case of singly corrugated filters, in sec. 3.3 it was described the procedure to assess the behaviour of the doubly corrugated filters presented in sec. 2.6, by using both simulations and measurements.

4.2.2.1 Simulations

A similar study to that performed for singly corrugated filters is shown for the doubly corrugated filters. In this case the influence of the width of the filter is studied by performing several simulations in which the width of the filter is varied in steps of b. Consequently, we introduce one new metallic post in each iteration in order to maintain the symmetry and periodicity of the structure. Tab. 4.1 shows the attenuation values at 2.45 GHz for each propagating mode.

Results show that all modes show acceptable attenuations for the empty doubly corrugated filter. Thus, doubly corrugated filters are able to deal with multimode problems, at least those in which only TE_{m0} modes are propagating. Additionally, it can be observed that increasing the width of the filter implies varying the attenuation

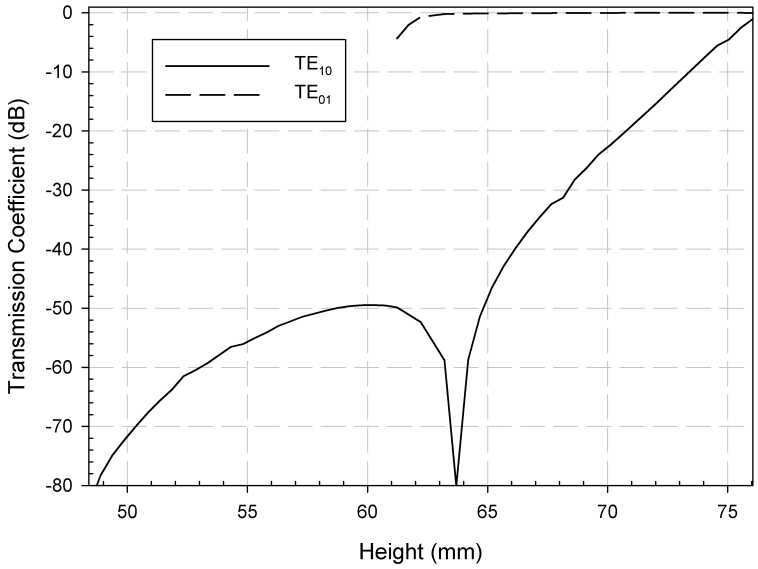

Figure 4.4: Transmission coefficient in dB at 2.45 GHz when varying the height of the doubly corrugated filter. Rest of parameters are shown in Tab. 3.1.

of all modes as a general trend. This is due to resonant frequency changes when changing the filter width.

In order to obtain the influence of the filter height and the capability of filtering non-TE_{m0} modes when no sample is inside, a parametric sweep varying the parameter g is carried out, keeping the rest of parameters fixed. The results of this sweep for the magnitude of S_{21} at 2.45 GHz are shown in Fig. 4.4. There, it can be seen that there are values of height around 61 mm that allow the propagation of the TE_{01} mode at 2.45 GHz with almost no attenuation while the TE_{10} mode is still properly filtered. Nevertheless, none of the modes are eliminated when increasing the height.

Thus, the conclusion from Tab. 4.1 and Fig. 4.4 is that empty doubly corrugated filters are suitable for multimode applications where only TE_{m0} modes are propagating. Increasing the height leads to the appearance of TE_{0n}, TE_{mn} $(m, n > 0)$ and TM_{mn} modes which cannot be properly filtered. Fortunately, usual industrial applications where corrugated filters are employed are oriented to the processing of thin materials and therefore only TE_{m0} modes will be propagating.

The influence of the dielectric properties of the processed material is much more important due to the vast number of materials that can be processed. In order to obtain this influence, a 2-D parametric sweep has been performed by varying both the dielectric constant and the loss tangent of the sample. The geometry of the simulated structure is the reference one for the doubly corrugated filter as indicated in Tab. 3.1, where only the TE_{10} mode is propagating. The sample thickness is g - 3 mm, and it is placed as depicted in Fig. 3.8.

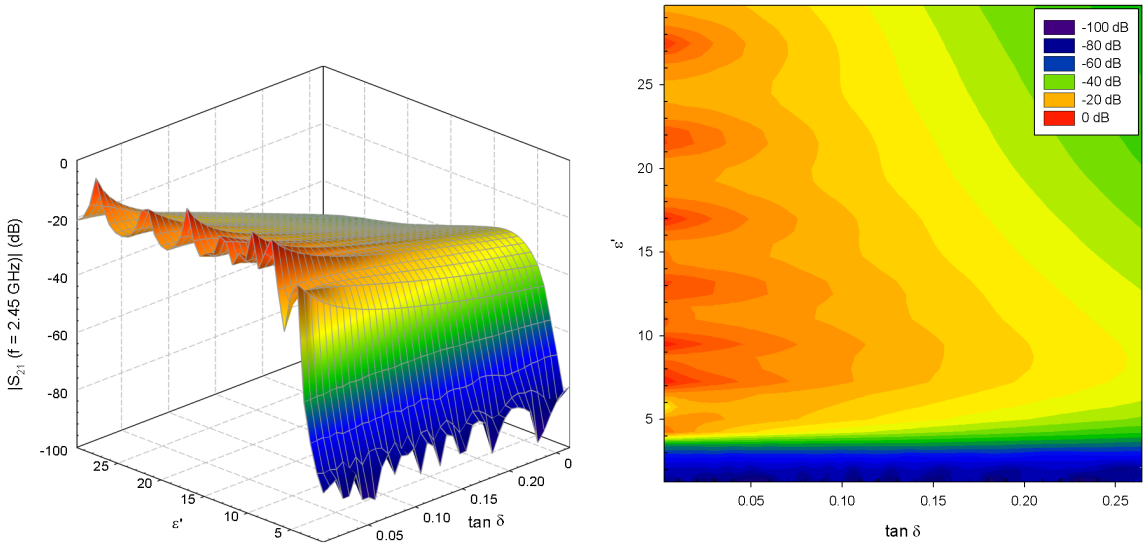

(a) 3-D plot **(b)** Contour plot

Figure 4.5: Magnitude in dB of transmission coefficient of TE_{10} mode for different values of dielectric constant and loss tangent of the processed material.

Results of the transmission coefficient for the TE_{10} mode at 2.45 GHz are shown in Fig. 4.5. It can be observed that ε' values under 4 show valid results, regardless the value of $\tan\delta$. However, over this value of ε' the attenuation decreases to unacceptable levels. Only when both the loss tangent and the dielectric constant reach high levels the attenuation becomes acceptable again. Therefore, there is a wide range of $(\varepsilon', \tan\delta)$ pairs where the filter cannot be used with safety. It is true that increasing the number of sections of the filter and therefore the total length of the sample, the attenuation increases because the electric field has to travel a longer distance through the material. Nevertheless the improvement is not enough to consider the results as acceptable when dealing with those problematic materials.

In order to fully understand these results, three pairs of $(\varepsilon', \tan\delta)$ values have been chosen as representative values of the three possible situations explained earlier. The magnitude of the electric field distribution along the filter for each case is depicted in Fig. 4.6 on a cutting plane located in the middle of the sample ($y = 0.85$ cm). In the first case ($\varepsilon'_1 = 3$, $\tan\delta_1 = 0.0184$), the results are quite similar to those obtained when the filter is empty, since both the dielectric constant and the loss tangent are not high enough to completely change the bandstop response in the vacuum case and therefore the electric field is attenuated before leaving the waveguide. The second value ($\varepsilon'_2 = 10$, $\tan\delta_2 = 0.0828$) corresponds to a scenario where most of the radiation is propagated along the sample due to the appearance of new modes which are not properly filtered. These new modes appear as a result of the decrease of the cutoff frequency of the propagating modes when increasing the electric permittivity

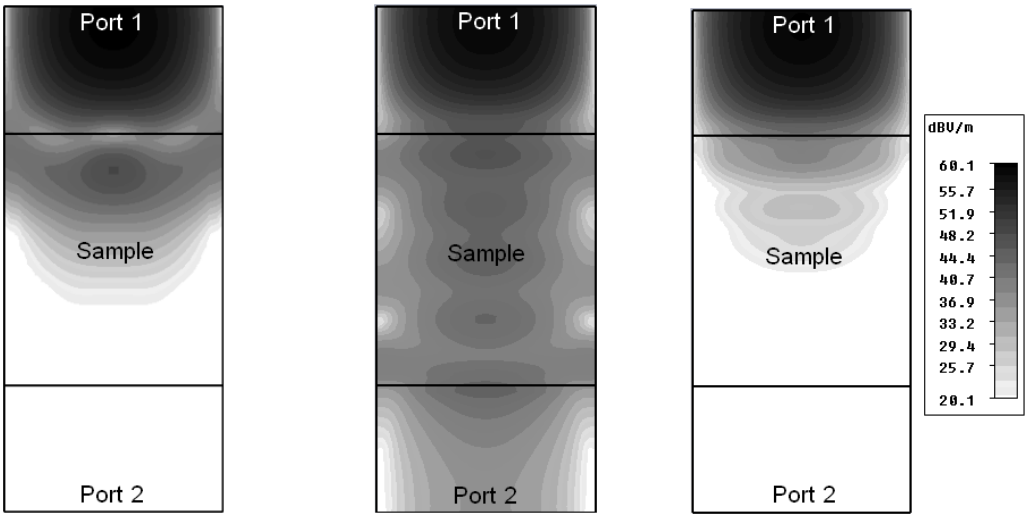

(a) $\varepsilon'_1 = 3$, $\tan\delta_1 = 0.0184$ **(b)** $\varepsilon'_2 = 10$, $\tan\delta_2 = 0.0828$ **(c)** $\varepsilon'_3 = 30$, $\tan\delta_3 = 0.2668$

Figure 4.6: Top view of the doubly corrugated filter showing the magnitude of the electric field distribution along the filter for different values of the electric permittivity of the sample on a cutting plane located in the middle of the sample ($y = 0.85$ cm).

of the sample. Finally, the third chosen pair ($\varepsilon'_3 = 30$, $\tan\delta_3 = 0.2668$) represents a case where the electric field is attenuated by means of high dielectric losses, not because of the filter design.

In order to develop a rule of thumb that predicts the approximate attenuation when materials are inserted in the waveguide, a polynomial that fits the data from Fig. 4.5 in a least-squares sense has been obtained considering materials with no losses, which is the worst case. In particular, a good fitting has been obtained with a polynomial of degree 4. This polynomial is expressed in terms of the dielectric constant ε' and therefore it can be expressed in terms of the cutoff frequency of the fundamental mode $f_c^{\mathrm{TE}_{10}}$ as follows in (4.1) and (4.2), where $\omega = 2\pi f$, being $f = 2.45$ GHz, and μ_0 and ε_0 are the magnetic permeability and the electric permittivity of the vacuum, respectively.

$$\left|\hat{S}_{21}\right|(\mathrm{dB}) = -0.0015(\varepsilon')^4 + 0.1126(\varepsilon')^3 - 2.9517(\varepsilon')^2 + 31.4312(\varepsilon') - 123.4267 \tag{4.1}$$

$$\varepsilon' = \frac{1}{\left(2\omega f_c^{\mathrm{TE}_{10}}\right)^2 \mu_0 \varepsilon_0} \tag{4.2}$$

In Fig. 4.7 it is shown this polynomial as a function of the dielectric constant and the normalized cutoff frequency. This normalized cutoff frequency is defined as the cutoff frequency of the fundamental mode divided by the value of 2.45 GHz. As it

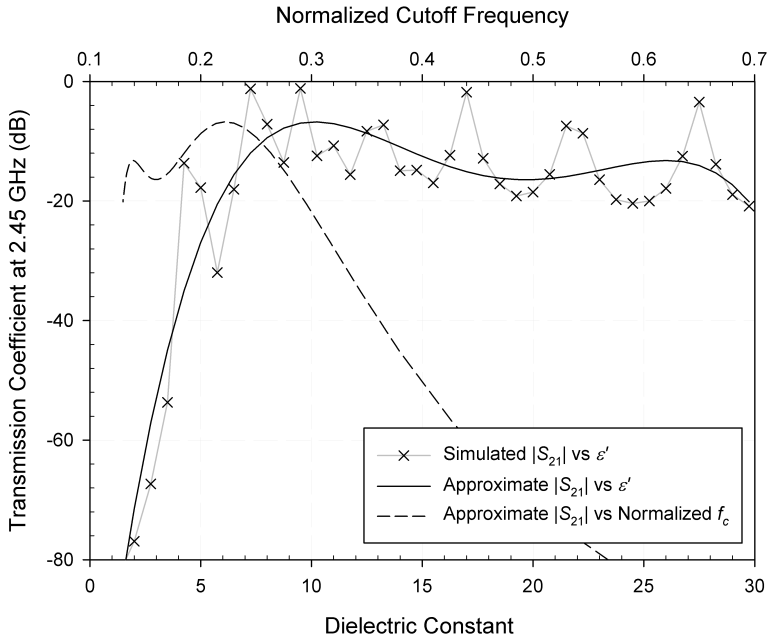

Figure 4.7: Estimate of the magnitude of the transmission coefficient in dB at 2.45 GHz as a function of the dielectric constant of the sample and the normalized cutoff frequency of the fundamental mode.

Scenario	Simulated $\|S_{21}\|$(dB)	Estimated $\|S_{21}\|$(dB)
Reference filter ($\varepsilon' = 10$)	-9.93	-6.77
Reference filter ($\varepsilon' = 20$)	-18.46	-16.43
Double width ($\varepsilon' = 10$)	-12.29	-6.77
Double width ($\varepsilon' = 20$)	-13.68	-16.43

Table 4.2: Comparison between simulated and approximate transmission coefficient for the TE_{10} mode and differente scenarios.

can be seen, when the dielectric constant increases the cutoff frequency decreases and the attenuation levels become unacceptable.

Finally, in order to assess the validity of this estimate, in Tab. 4.2 some results from simulations are compared to the approximate value given by the polynomial in (4.1) for different structures and several materials.

As it can be seen, the attenuation value obtained with the polynomial can provide a quick estimate with an acceptable accuracy of the actual attenuation of the fundamental mode. It must be pointed out that this estimate is valid for the TE_{m0} modes, which show a similar behavior. Therefore, this estimate can be applied only to find out if a given material cannot be processed with safety and this can be useful in the early stages of design.

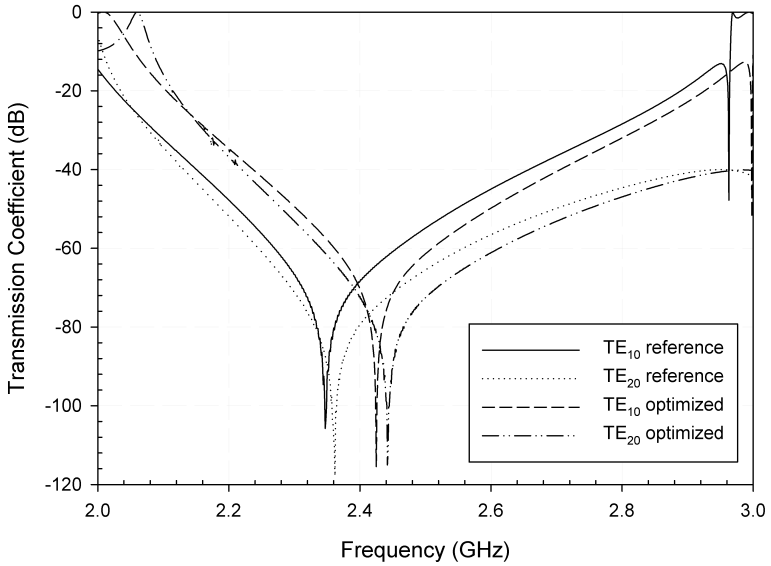

Figure 4.8: Comparison between results before and after the optimization process for the empty doubly corrugated filter when the width is doubled.

4.2.2.2 Optimization of doubly corrugated filters

The possibilities of applying genetic algorithms when some of the design parameters of the filter are optimized in order to improve the frequency response of the structure have been assessed as well. In this way, two different optimization scenarios have been studied, both using genetic algorithms.

Firstly, it was observed that when increasing the width of the empty doubly corrugated filter the center frequency of the eliminated band decreases. For example, if the center frequency for the TE_{10} mode is 2.43 GHz in the case of the reference filter, this frequency decreases to 2.35 GHz when the width is doubled. A similar reduction is observed for the rest of propagating modes. Therefore, an optimization procedure by means of genetic algorithms was applied by optimizing the parameter d of the filter, i.e. the height of the posts, according to the evaluation function defined in (3.2) and (3.3). Regarding the genetic algorithms parameters, 10 generations and 10 individuals per generation have been employed. Good convergence results have been obtained with this configuration, although depending on the number of optimized parameters these configuration parameters might be different. At the end of this optimization procedure, the center frequency was successfully repositioned at the reference value, as seen in Fig. 4.8, by means of decreasing the parameter d from 2.839 to 2.7324.

Thus, results from Tab. 4.1 can be improved even more by optimizing the parameter d. This adjustment could have been done with a regular parametric sweep. However, using genetic algorithms in this problem is useful to validate the optimization

Parameter	Value
Posts ($m \times n$)	8×9
w (cm)	31
$g + d$ (cm)	4.839
l_x (cm)	3.875
b_x (cm)	0.8213
l_z (cm)	6.3408
b_z (cm)	0.2889
d (cm)	2.3652

Table 4.3: Optimum parameters for the doubly corrugated filter when a sample of permittivity $\varepsilon_r = 10 - j0.1$ is placed inside.

procedure. In this way, results when applying the procedure to a more complex scenario, as the following one, will be reliable.

In this more complex scenario, the objective is trying to filter all the propagating modes when a sample of permittivity $\varepsilon_r = 10 - j0.1$, which is a problematic value according to Fig. 4.5, is placed inside the doubly corrugated filter. Thus, a filter with an open port dimensions of 31 cm width and 4.839 cm height has been employed, optimizing the rest of geometric parameters: number of metallic posts, m in x and n in y, the separation between them in both dimensions, b_x and b_z, the width of the posts in z, l_z, and its length, d. The width of the posts in x is given by m and b_x, since the width of the waveguide port is fixed. The open ports dimensions have been fixed because these dimensions are determined by the size of the microwave applicator and the sample, and they are usually not a design parameter. In this case, 30 generations and 10 individuals per generation have been employed. Again, the evaluation function is the one defined in (3.2) and (3.3). The final parameters after the optimization process are shown in Tab. 4.3. Results for all propagating modes using these parameters are depicted in Fig. 15. From these results, the main conclusion is that it is not possible to obtain a doubly corrugated filter with metallic posts which works properly with this material.

Therefore, it can be concluded that genetic algorithms are a powerful tool when some readjustments are necessary, but when the filter fails in a specific task, there is nothing optimization can do.

As explained earlier, some simulations with the filter and oversized waveguides have been carried out in order to study the behavior of the filter when dealing with a greater number of modes coming from the microwave heating cavity. In particular, according to the new port dimensions depicted in Fig. 3.9, 13 modes are simulated. The filter dimensions are shown in Tab. 4.4, corresponding to a doubly corrugated filter. The parameter d has been optimized to 2.7324 cm as seen earlier since the filter width has been doubled versus the reference geometry in Tab. 3.1.

Results are shown in Tab. 4.5 and Tab. 4.6 for the two configurations under study

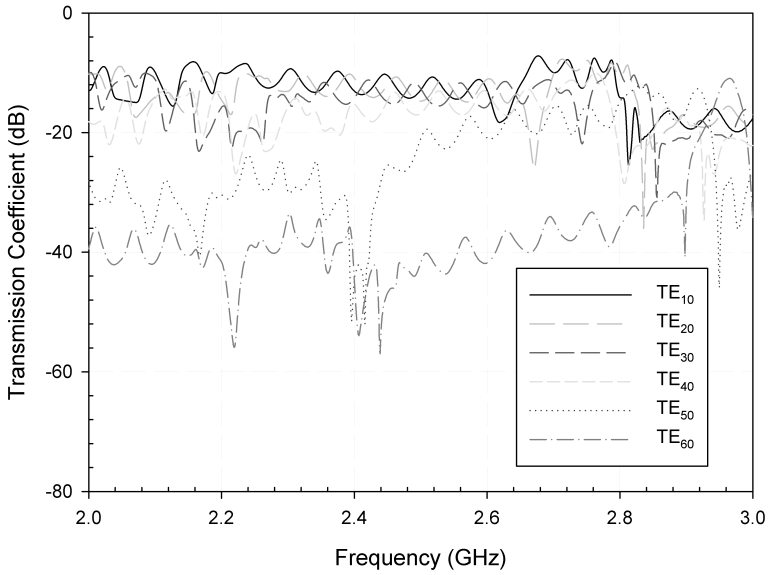

Figure 4.9: Results for the optimum filter when a sample of permittivity $\varepsilon_r = 10 - j0.1$ is placed inside the doubly corrugated filter.

Parameter	Value
Posts ($m \times n$)	6×4
g (cm)	2.1066
d (cm)	2.7324
w (cm)	17.272
l (cm)	2.879
b (cm)	1.6

Table 4.4: Geometry of the doubly corrugated filter connected to the oversized waveguides.

and for different materials including the case of an empty filter. The three chosen values of electric permittivity are those used before.

As expected, good results are obtained for the empty filter. It has been shown in this work that the filter works well with TE_{m0} modes, which are the only ones propagating through the filter since the rest of the modes are below cutoff according to the filter dimensions. However, for the materials 1 and 2 the filter does not work properly. The modes which were below cutoff for the empty filter are now able to propagate due to the reduction of the cutoff frequency as a result of the introduction of the sample. Especially significant is the low attenuation of the TE_{0n} modes, which varies depending on the filter position due to field distribution of each mode but it is still unacceptable in both cases.

Mode / Material	Vacuum	$\varepsilon'_1 = 3$ $\tan\delta_1 = 0.0184$	$\varepsilon'_2 = 10$ $\tan\delta_2 = 0.0828$	$\varepsilon'_3 = 30$ $\tan\delta_3 = 0.2668$
TE_{01}	-81.11	-25.78	-39.72	-108.79
TE_{10}	-89.39	-22.47	-34.08	-93.96
TE_{11}	-82.64	-28.05	-33.92	-95.26
TM_{11}	-117.86	-19.41	-34.89	-93.01
TE_{02}	-73.98	-17.61	-31.23	-100.05
TE_{20}	-88.78	-56.13	-35.60	-104.75
TE_{12}	-79.40	-24.44	-33.98	-100.62
TM_{12}	-90.27	-19.41	-34.13	-91.33
TE_{21}	-87.50	-53.04	-35.38	-102.91
TM_{21}	-91.69	-53.20	-34.69	-99.58
TE_{03}	-78.75	-21.49	-34.53	-102.87
TE_{22}	-104.87	-63.79	-41.02	-109.00
TM_{22}	-87.81	-41.32	-30.07	-87.85

Table 4.5: $|S_{21}|$ in dB at 2.45 GHz when oversized waveguides are placed at the filter ports, keeping the filter in the bottom.

Mode / Material	Vacuum	$\varepsilon'_1 = 3$ $\tan\delta_1 = 0.0184$	$\varepsilon'_2 = 10$ $\tan\delta_2 = 0.0828$	$\varepsilon'_3 = 30$ $\tan\delta_3 = 0.2668$
TE_{01}	-69.29	-8.70	-21.16	-86.96
TE_{10}	-82.26	-27.94	-31.25	-92.31
TE_{11}	-83.24	-19.79	-27.44	-93.40
TM_{11}	-78.76	-16.20	-25.83	-91.71
TE_{02}	-152.55	-64.52	-55.15	-112.57
TE_{20}	-86.34	-56.82	-41.37	-99.95
TE_{12}	-93.25	-38.54	-42.13	-101.07
TM_{12}	-77.59	-22.37	-26.41	-88.66
TE_{21}	-126.39	-66.15	-43.22	-102.63
TM_{21}	-87.30	-44.13	-23.12	-87.46
TE_{03}	-79.97	-20.11	-32.85	-99.15
TE_{22}	-94.13	-64.99	-45.60	-105.34
TM_{22}	-76.21	-46.15	-31.79	-93.85

Table 4.6: $|S_{21}|$ in dB at 2.45 GHz when oversized waveguides are placed at the filter ports, keeping the filter in the middle.

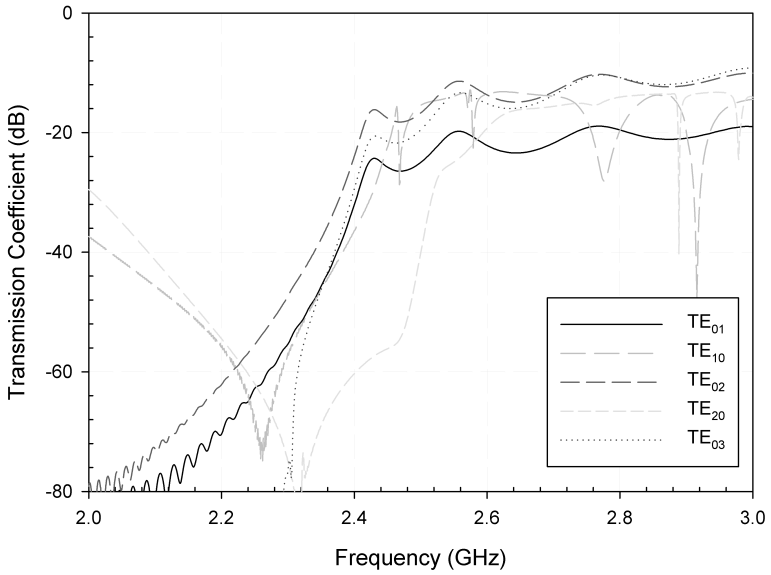

Figure 4.10: Results for the doubly corrugated filter placed in the bottom of the oversized waveguides with a sample of dielectric properties $\varepsilon_1' = 3$, $\tan\delta_1 = 0.0184$.

It might seem that the results for these two materials are very similar, although they are not. In Fig. 4.10 and Fig. 4.11 the TE_{m0} and TE_{0n} modes are shown for material 1 and 2 respectively when the filter is set in the bottom. From these figures it can be noticed that the two TE_{m0} modes show a bandstop response at a lower frequency for the first material. Therefore, this stopband can be repositioned at 2.45 GHz by modifying the length of the metallic posts as seen before, using 10 generations and 10 individuals per generation. In this way, the results when decreasing d to 2.391 cm are depicted in Fig. 4.12 showing acceptable levels for the TE_{10} and TE_{20} modes at the frequency of interest. Nevertheless, the rest of the modes are not properly filtered and therefore a safe use cannot be guaranteed. It must be pointed out that the TE_{0n} modes do not show a bandstop response, but a quite flat response from the frequency where the mode is not below cutoff. This fact can be seen clearly in Fig. 4.10 and Fig. 4.11. In Fig. 4.10 the cutoff frequency of these modes is bigger than in Fig. 4.11 due to the lower dielectric constant of the sample. For the second material it is not possible to improve the filter response even for the TE_{m0} modes. Finally, for the third material all the modes are attenuated due to the high dielectric losses as explained before.

4.2.2.3 Measurements

Once it has been shown by simulations the severe limitations of this type of filters, the three materials shown in Tab. 3.3 have been experimentally tested by placing them inside the doubly corrugated filter prototype. The transmission coefficient for

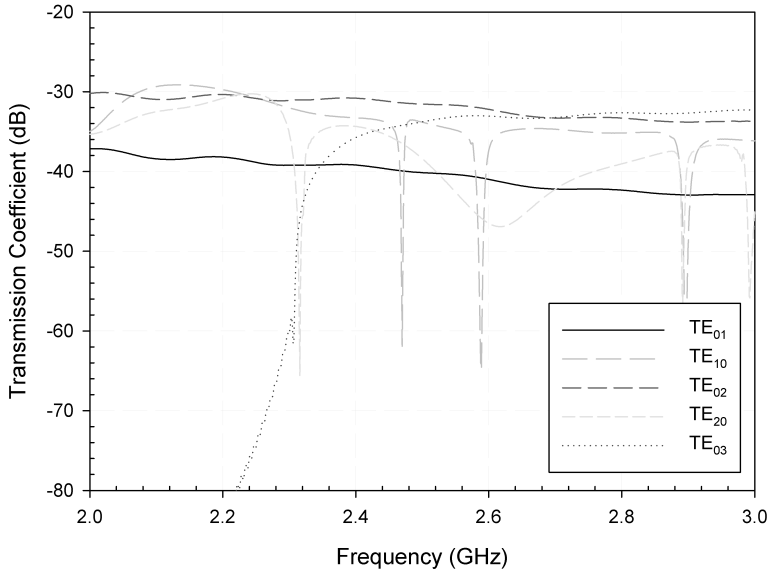

Figure 4.11: Results for the doubly corrugated filter placed in the bottom of the oversized waveguides with a sample of dielectric properties $\varepsilon_2' = 10$, $\tan\delta_2 = 0.0828$.

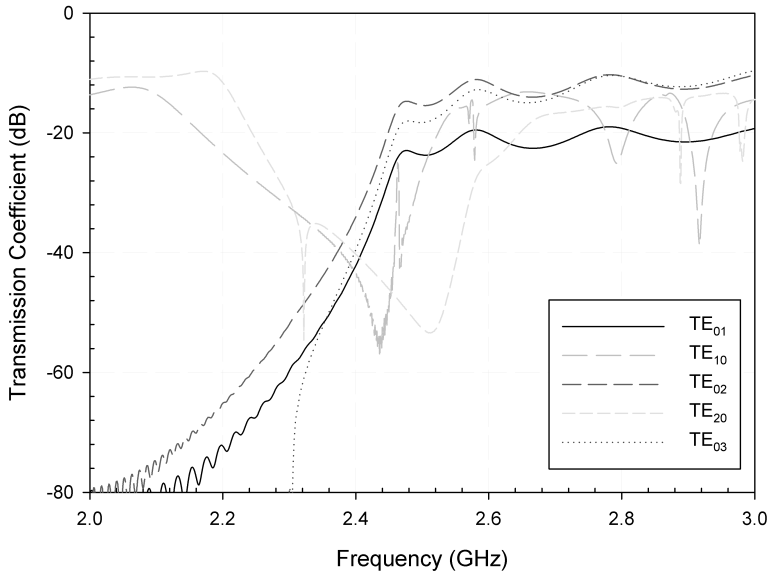

Figure 4.12: Results for the doubly corrugated filter placed in the bottom of the oversized waveguides with a sample of dielectric properties $\varepsilon_1' = 3$, $\tan\delta_1 = 0.0184$, decreasing the length of the metallic posts as a result of the optimization process ($d = 2.391$ cm).

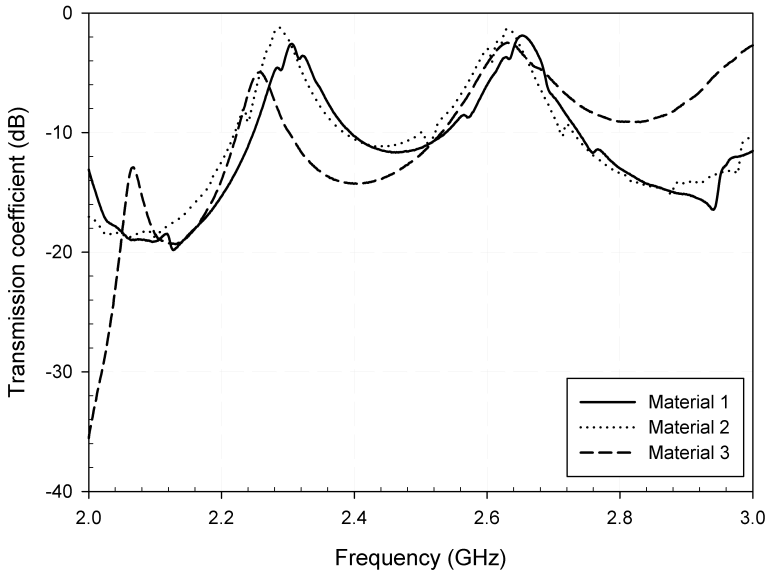

Figure 4.13: Measured transmission coefficient (dB) for the doubly corrugated filter with the materials under test ($\varepsilon'_1 = 7.90$, $\tan\delta_1 = 0.0440$; $\varepsilon'_2 = 8.18$, $\tan\delta_2 = 0.0196$; $\varepsilon'_3 = 5.49$, $\tan\delta_3 = 0.0581$).

the three measured materials is shown in Fig. 4.13, confirming the inability to deal with this kind of materials.

It must be pointed out that some optimization procedures have been employed trying to improve the performance of the filter with these materials by optimizing all the design parameters. The main conclusion is that it is not possible to obtain a doubly corrugated filter with metallic posts which works properly with this kind of materials.

4.2.3 Resistive filters

Two different structures for resistive filters with water were presented in sec. 3.6.1 and sec. 3.6.2. In this section, results when simulating these structures are presented.

4.2.3.1 Resistive filter with water cylinders

First of all, a monomode filter has been simulated in order to obtain the filtering capability of this kind of structures. An optimization procedure has been carried out by varying l, d, D and the number of cylinders, according to Fig. 3.24. Thus, the used parameters are shown in Tab. 4.7. Results for the TE_{10} mode are shown in Fig. 4.14. For the monomode filter, it has been possible to obtain a proper bandstop response when no material is placed inside.

Parameter	Value
Cylinders	4
w (cm)	8.636
a (cm)	4.839
l (cm)	5.739
D (cm)	1.0572
d (cm)	1.7043

Table 4.7: Geometry of the optimized monomode filter with water cylinders.

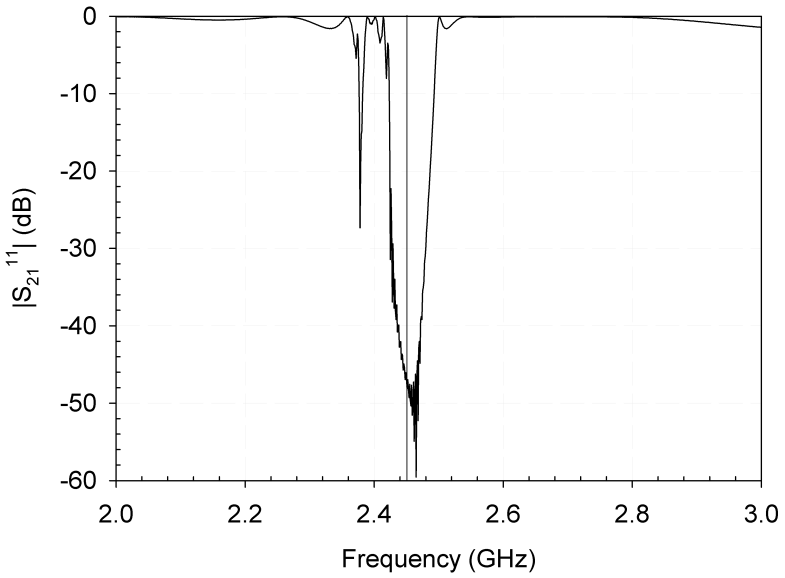

Figure 4.14: S_{21} for the TE_{10} mode for an empty filter with water cylinders.

In the case of a multimode filter, a new optimization procedure has been carried out with a double width empty filter. The optimized parameters are shown in Tab. 4.8. Results for this geometry are shown in Fig. 4.15 for each material depicted in Tab. 3.5 and for the TE_{10} (a) and TE_{20} (b) modes. As it can be seen, the filter works well only for the third material, with high dielectric losses. The rest of scenarios are not reliable for a safe usage of the filter.

4.2.3.2 Resistive filter with water and PTFE corrugations

In this case, the optimization procedure has been applied to a monomode filter by modifying lz, bz and d from Fig. 3.25. The used parameters are shown in Tab. 4.9. Results for the TE_{10} mode are shown in Fig. 4.16. It can be perceived that with this type of filter it is possible to obtain a proper bandstop filter, at least for the fundamental mode and without any material inside the filter. Once it has been

Parameter	Value
Cylinders	4
w (cm)	17.272
a (cm)	4.839
l (cm)	7.6018
D (cm)	1.0529
d (cm)	1.5801

Table 4.8: Geometry of the optimized multimode filter with water cylinders.

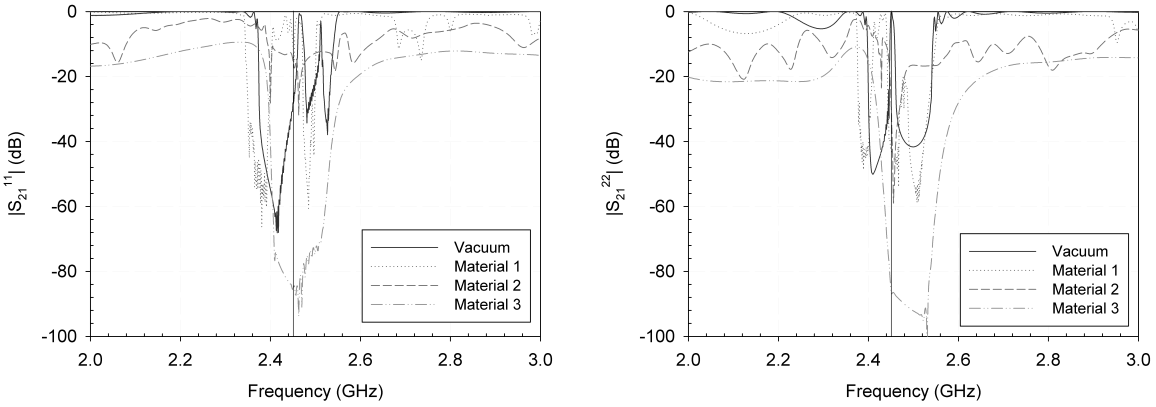

(a) TE_{10} mode **(b)** TE_{20} mode

Figure 4.15: S_{21} for different materials placed inside the multimode filter with water cylinders ($\varepsilon_1' = 2.55$, $\tan\delta_1 = 0.0063$; $\varepsilon_2' = 9$, $\tan\delta_2 = 0.0244$; $\varepsilon_3' = 40$, $\tan\delta_3 = 0.3$).

Parameter	Value
Posts	3×4
w (cm)	8.636
a (cm)	4.839
lx (cm)	2.8787
bx (cm)	1.6
lz (cm)	5.5006
bz (cm)	4.1839
d (cm)	1.8783

Table 4.9: Geometry of the optimized monomode filter with water and PTFE corrugations.

shown that monomode filters can be designed with this type of corrugations, a new optimization procedure has been carried out with a multimode filter.

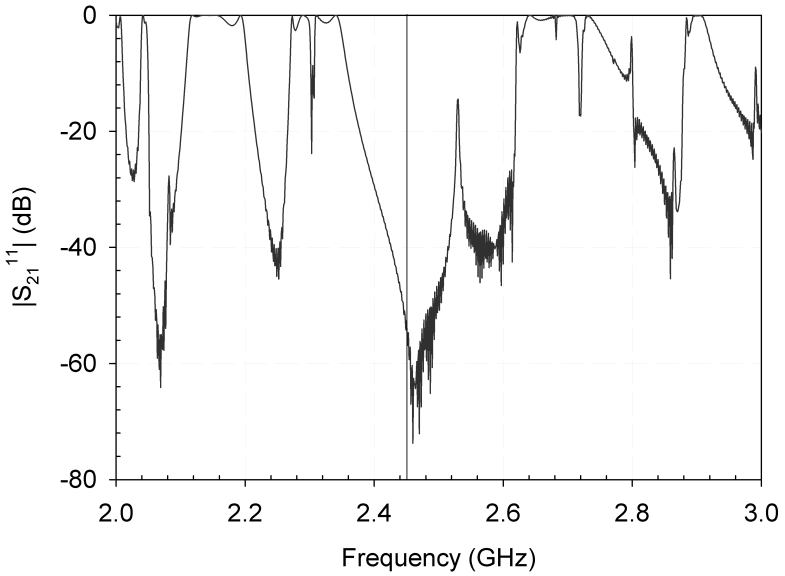

Figure 4.16: S_{21} for the TE_{10} mode for an empty filter with water cylinders.

Parameter	Value
Posts	6×4
w (cm)	17.272
a (cm)	4.839
lx (cm)	2.8787
bx (cm)	1.6
lz (cm)	4.6267
bz (cm)	4.1373
d (cm)	2.3113

Table 4.10: Geometry of the optimized multimode filter with water and PTFE corrugations.

The parameters of the filter used in the simulations are depicted in Tab. 4.10. Results for this geometry are shown in Fig. 4.17, where the magnitude of S_{21} for each material in Tab. 3.5 is represented for the TE_{10} (a) and TE_{20} (b) modes. In this case, although the response presents sharp variations, attenuation levels might be acceptable if power levels are not very high at 2.45 GHz for all materials except for material 2. Several optimization procedures have been carried out in order to obtain a proper response when the material 2 is placed inside the studied filters. However, with the analyzed structures it has been impossible to obtain a good solution for this value of dielectric constant.

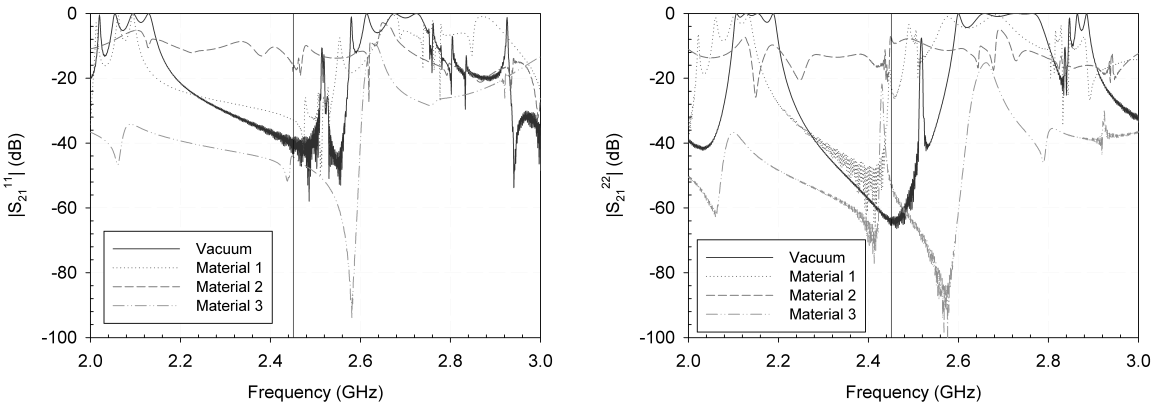

(a) TE_{10} mode **(b)** TE_{20} mode

Figure 4.17: S_{21} for different materials placed inside the multimode filter with water and PTFE corrugations ($\varepsilon'_1 = 2.55$, $\tan\delta_1 = 0.0063$; $\varepsilon'_2 = 9$, $\tan\delta_2 = 0.0244$; $\varepsilon'_3 = 40$, $\tan\delta_3 = 0.3$).

4.3 New proposed filter

In order to solve the problems presented in the previous section, a new kind of filter based on a combination of metallic irises and tuning posts has been designed. In sec. 3.3 it was presented the structure and design parameters of this new filter. In this way, an optimization procedure based on genetic algorithms has been applied by varying the parameters D, d_{iris}, d_{post} and g to obtain the best possible bandstop response when the filter is empty. In this particular case, 50 generations and 30 individuals per generation have been employed in order to minimize the evaluation function in 3.2 applied to the fundamental mode. The final design parameters are shown in Tab. 3.2 according to the geometry shown in Fig. 3.10. Fig. 4.18 shows a comparison between simulation and measurements when no material is placed inside the filter, showing a good agreement.

When introducing the pieces of marble and granite inside the filter, a readjustment of the length of the tuning posts must be done, since the dielectric properties of each material are different. Nevertheless, after an optimization process and a manual tuning process, it is possible to obtain excellent attenuation results at the frequency of interest for the three materials. The flexibility of this tuning process makes possible to obtain different bandstop responses, either a wider stopband with medium attenuation values, as shown in Fig. 4.19, or a more resonant response with higher attenuation, as shown in Fig. 4.20, depending on the requirements of the considered application. The dimensions of all the posts d_{post-i} for each material are shown in Tab. 4.11, Tab. 4.12 and Tab. 4.13. It can be observed that it is not necessary that symmetry is maintained for the posts penetration at each row in order to obtain a good filter response. This will also be corroborated at sec. 4.7.

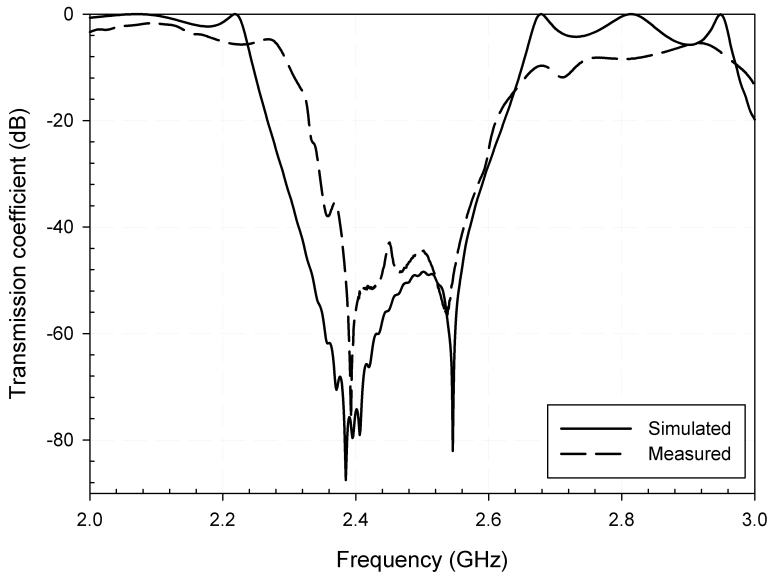

Figure 4.18: Comparison between simulation and measurements for the new filter with no material inside.

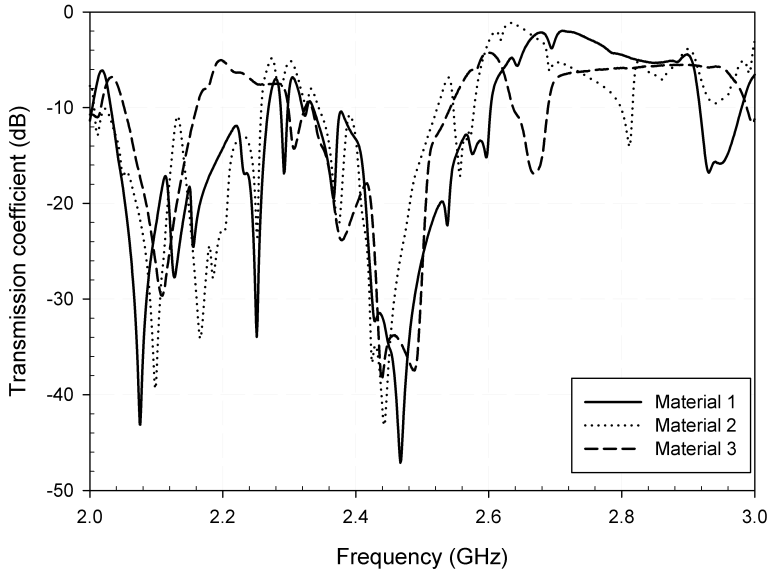

Figure 4.19: Measured transmission coefficient (dB) with a wider stopband for the new proposed filter with the materials under test ($\varepsilon'_1 = 7.90$, $\tan\delta_1 = 0.0440$; $\varepsilon'_2 = 8.18$, $\tan\delta_2 = 0.0196$; $\varepsilon'_3 = 5.49$, $\tan\delta_3 = 0.0581$).

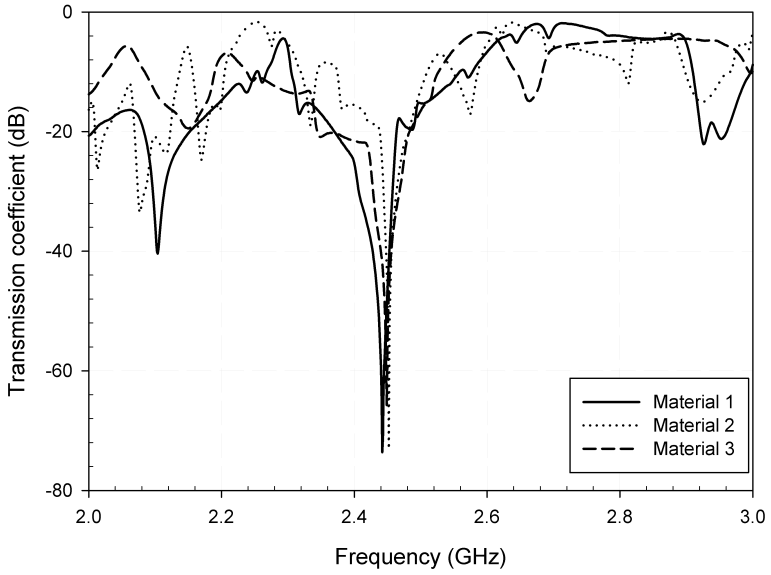

Figure 4.20: Measured transmission coefficient (dB) with high Q for the new proposed filter with the materials under test ($\varepsilon'_1 = 7.90$, $\tan\delta_1 = 0.0440$; $\varepsilon'_2 = 8.18$, $\tan\delta_2 = 0.0196$; $\varepsilon'_3 = 5.49$, $\tan\delta_3 = 0.0581$).

Row / Column	Wider stopband			High Q		
	1	2	3	1	2	3
1	25.06	28.63	27.11	35.58	33.76	32.16
2	26.28	23.35	29.04	31.99	34.74	32.25
3	30.72	32.45	31.30	36.03	34.54	34.05
4	25.27	33.11	23.45	33.53	27.44	34.82

Table 4.11: Dimensions of the posts in mm when the filter is filled with material 1.

Row / Column	Wider stopband			High Q		
	1	2	3	1	2	3
1	26.26	28.76	28.13	26.54	31.32	32.40
2	25.21	22.43	28.54	23.27	31.90	26.79
3	30.67	29.92	30.82	28.07	32.44	27.94
4	24.32	28.84	24.69	22.85	23.38	31.36

Table 4.12: Dimensions of the posts in mm when the filter is filled with material 2.

Row / Column	Wider stopband			High Q		
	1	2	3	1	2	3
1	33.83	33.31	37.06	36.41	35.74	36.82
2	31.30	31.90	33.91	36.47	25.74	36.66
3	33.09	23.63	33.54	34.60	35.67	36.11
4	25.15	26.38	24.38	34.89	27.45	33.01

Table 4.13: Dimensions of the posts in mm when the filter is filled with material 3.

Mat.	Wider stopband		High Q	
	BW below -30 dB (MHz)	Maximum attenuation (dB)	BW below -30 dB (MHz)	Maximum attenuation (dB)
1	64	47.11	3	73.63
2	36	43.19	2	73.04
3	66	38.46	2	65.73

Table 4.14: Summary of bandwith and maximum attenuation results for the new proposed filter.

Mat.	Wider stopband	High Q
	Att. improvement (dB)	Att. improvement (dB)
1	35.52	62.04
2	32.05	61.90
3	24.80	52.07

Table 4.15: Attenuation improvement in dB when comparing the doubly corrugated filter and the new proposed filter.

Tab. 4.14 shows a summary of bandwidth and maximum attenuation results for each case depicted in Fig. 4.19 and Fig. 4.20. As it can be seen, the higher the maximum attenuation, the lower the bandwidth. Nevertheless, the low bandwidth is suitable for the signals produced by typical magnetrons. In any case, one can conclude that with this new filter both the bandwidth and the attenuation can be adjusted depending on the requirements of the application.

All in all, Tab. 4.15 shows the increase of the attenuation at 2.45 GHz achieved with the new filter when comparing to the doubly corrugated filter (Fig. 4.13). As it can be seen, the increase is significant in both cases, so one can conclude that this new proposed filter offers a proper solution to the leakage problem when dealing with this kind of materials.

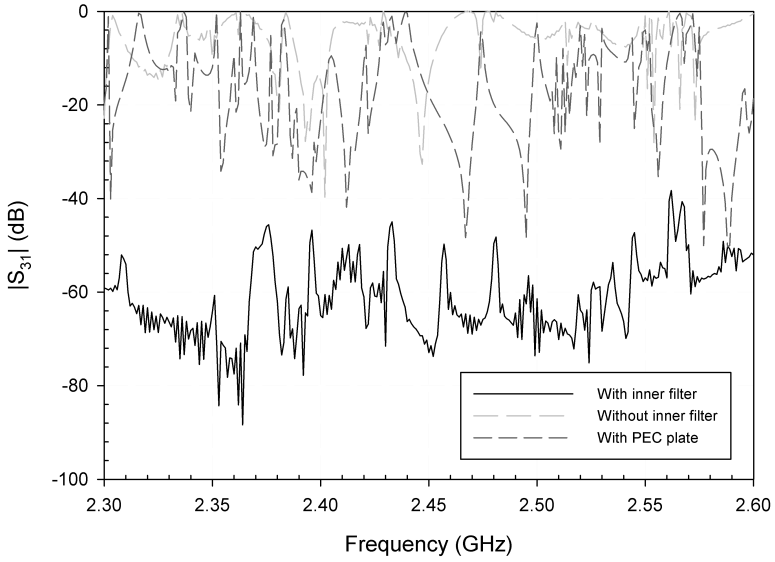

Figure 4.21: Magnitude of the crosscoupling between the pair of ports 1-3 for configuration no. 1 and no material inside.

4.4 Reduction of the crosscoupling in multifed multimode cavities

In sec. 3.4 it was introduced a novel application of doubly corrugated filters in order to reduce the crosscoupling between feeds in a microwave-heating cavity. As it was explained and depicted in Fig. 3.13, the filter is placed in the middle of the cavity held by a metallic plate. Thus, in order to have a detailed vision of the filtering effects and the influence of the PEC plate which holds the filter, we have represented in Fig. 4.21 and Fig. 4.22 the coupling from 2.3 to 2.6 GHz between two of the ports that are in symmetrical positions for each configuration, i.e. ports 1-3 for configuration no. 1 and ports 1-4 for configuration no. 2, respectively.

In these figures, the coupling of the ports is compared with and without the inner filter, and with only the metallic plate. In this case an empty cavity is considered, with no sample inside. From these figures, it can be seen that the filter is working properly at the frequency range of interest and therefore the crosscoupling is reduced at those frequencies. Furthermore, it can be observed that the crosscoupling is not reduced at all when using only the metallic wall. Thus, the crosscoupling reduction is achieved by means of the inner filter and not because of the metallic plate. Similar results are obtained for the other pairs of ports, 2-4 and 2-3, respectively.

A summary of crosscoupling results at 2.45 GHz for each configuration is shown in Tab. 4.16 and Tab. 4.17. From Tab. 4.16 it can be seen a reduction of the crosscoupling between the pairs of ports 1-3, 1-4 (2-3) and 2-4, which are separated by the

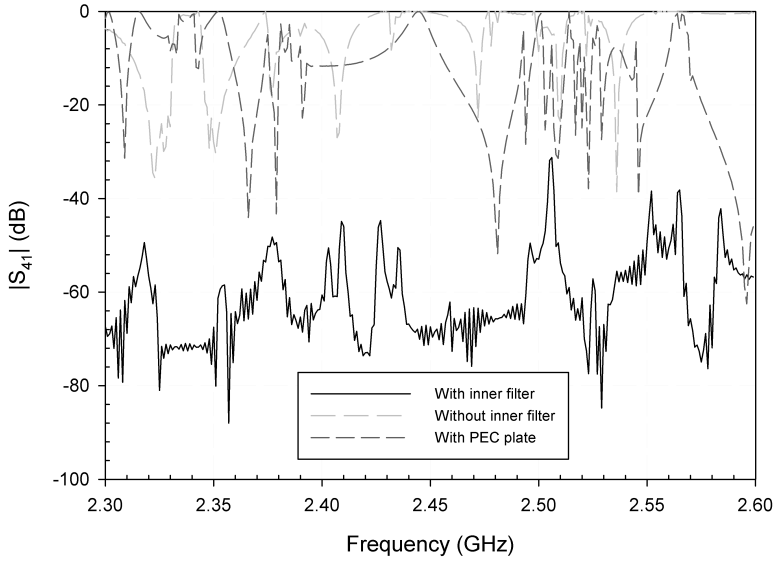

Figure 4.22: Magnitude of the crosscoupling between the pair of ports 1-4 for configuration no. 2 and no material inside.

Material / S-Parameters	$\|S_{21}\|$, $\|S_{43}\|$ (dB)			$\|S_{31}\|$ (dB)		
	No filter	Plate	Filter	No filter	Plate	Filter
Vacuum	-21.62	-30.76	-22.51	-11.12	-17.89	-71.92
$\varepsilon_1' = 2$, $\tan\delta_1 = 0.01$	-15.81	-55.35	-10.78	-4.10	-18.75	-65.54
$\varepsilon_2' = 8.6$, $\tan\delta_2 = 6 \times 10^{-4}$	-29.18	-50.79	-26.43	-11.78	-14.54	-36.21
$\varepsilon_3' = 29.5$, $\tan\delta_3 = 0.2654$	-29.65	-52.31	-32.82	-19.20	-47.28	-98.56
Material / S-Parameters	$\|S_{41}\|$, $\|S_{32}\|$ (dB)			$\|S_{42}\|$ (dB)		
	No filter	Plate	Filter	No filter	Plate	Filter
Vacuum	-21.62	-34.85	-84.24	-26.31	-13.75	-75.13
$\varepsilon_1' = 2$, $\tan\delta_1 = 0.01$	-15.81	-47.66	-71.58	-0.88	-9.99	-74.20
$\varepsilon_2' = 8.6$, $\tan\delta_2 = 6 \times 10^{-4}$	-29.18	-48.85	-47.99	-0.54	-19.55	-32.70
$\varepsilon_3' = 29.5$, $\tan\delta_3 = 0.2654$	-29.65	-45.62	-115.55	-21.95	-32.76	-112.84

Table 4.16: Crosscoupling between feeds for configuration 1 at 2.45 GHz.

filter. Particularly remarkable is the improvement obtained for the materials 1 and 2, which show a big coupling between 1-3 and 2-4 ports when the filter is removed. This is a logical behavior due to the symmetry of the structure, since these pairs of ports excite the same set of resonant modes. It can also be perceived that orthogonal feed placement does not guarantee a total reduction of the crosscoupling, as can be seen for the S_{21} parameter, though results may be still acceptable in some cases.

From Tab. 4.17 it can be seen that the results are even better for the second configuration. Bigger reductions are achieved for the pair of ports that are separated by

Material / S-Parameters	$\|S_{21}\|$, $\|S_{34}\|$ (dB)			$\|S_{31}\|$, $\|S_{24}\|$ (dB)		
	No filter	Plate	Filter	No filter	Plate	Filter
Vacuum	-158.27	-155.99	-72.29	-157.66	-157.20	-104.61
$\varepsilon_1' = 2$, $\tan\delta_1 = 0.01$	-164.32	-168.89	-60.63	-169.95	-165.72	-116.40
$\varepsilon_2' = 8.6$, $\tan\delta_2 = 6 \times 10^{-4}$	-176.02	-172.45	-88.46	-160.43	-165.59	-82.35
$\varepsilon_3' = 29.5$, $\tan\delta_3 = 0.2654$	-198.87	-185.52	-93.48	-185.68	-196.25	-152.66
Material / S-Parameters	$\|S_{41}\|$ (dB)			$\|S_{32}\|$ (dB)		
	No filter	Plate	Filter	No filter	Plate	Filter
Vacuum	-0.38	-4.42	-73.57	-0.54	-16.09	-74.48
$\varepsilon_1' = 2$, $\tan\delta_1 = 0.01$	-8.34	-20.19	-51.73	-6.01	-15.60	-56.90
$\varepsilon_2' = 8.6$, $\tan\delta_2 = 6 \times 10^{-4}$	-0.46	-10.83	-31.57	-0.42	-15.52	-47.33
$\varepsilon_3' = 29.5$, $\tan\delta_3 = 0.2654$	-19.92	-31.14	-100.15	-10.40	-20.51	-101.86

Table 4.17: Crosscoupling between feeds for configuration 2 at 2.45 GHz.

Material	f_1		f_2	
	No filter	Filter	No filter	Filter
Vacuum	0.0910	0.0056	0.0161	0.0057
$\varepsilon_1' = 2$, $\tan\delta_1 = 0.01$	0.4416	0.0835	0.8700	0.0824
$\varepsilon_2' = 8.6$, $\tan\delta_2 = 6 \times 10^{-4}$	0.0687	0.0025	0.8852	0.0028
$\varepsilon_3' = 29.5$, $\tan\delta_3 = 0.2654$	0.0142	5.23×10^{-4}	0.0086	4.40×10^{-4}

Table 4.18: Comparison of crosscouplings for configuration 1 at 2.45 GHz.

the filter. In addition, the crosscoupling between the ports of the same half of the cavity is very low in both cases, with and without filter. Results also show some very low values, less than -150 dB, in some cases when the filter is not used, such as S_{21}, S_{31}, S_{24} and S_{34}. This behavior is due to the high crosscoupling between the other pairs of ports, 1-4 and 2-3. When the filter is used, therefore reducing the crosscoupling between these ports, the energy distributes to the other ports increasing its crosscoupling. In any case, when the filter is used the crosscoupling between all the ports is very low. It must be said that the positions of the ports on each side of the filter have not been optimized and therefore the crosscoupling levels are high in some cases. All in all, configuration 2 is the best option regarding the crosscoupling between all ports.

Moreover, these results confirm the fact of the little influence that the PEC plate has on the crosscoupling reduction, which is mostly achieved by means of the inner corrugated filter.

In order to clarify the results from Tab. 4.16 and Tab. 4.17, the values of f_1 (equation 3.4) and f_2 (equation 3.5) have been depicted in Tab. 4.18 and Tab. 4.19 for each configuration. It can be observed that, in all cases, both values are much smaller when the filter is used.

Material	f_1		f_2	
	No filter	Filter	No filter	Filter
Vacuum	0.9164	1.03×10^{-7}	0.8838	5.67×10^{-8}
$\varepsilon'_1 = 2$, $\tan\delta_1 = 0.01$	0.1465	7.58×10^{-6}	0.2508	3.02×10^{-6}
$\varepsilon'_2 = 8.6$, $\tan\delta_2 = 6 \times 10^{-4}$	0.8991	6.96×10^{-4}	0.9075	1.85×10^{-5}
$\varepsilon'_3 = 29.5$, $\tan\delta_3 = 0.2654$	0.0102	5.46×10^{-10}	0.0911	6.08×10^{-10}

Table 4.19: Comparison of crosscouplings for configuration 2 at 2.45 GHz.

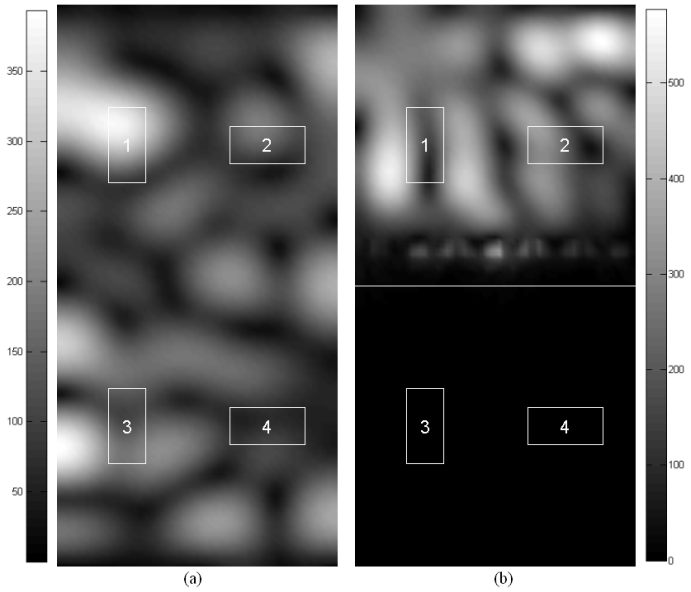

Figure 4.23: Electric field distribution in V/m on the surface ($y = 1.7$ cm) of the plastic sample ($\varepsilon'_1 = 2$, $\tan\delta_1 = 0.01$) caused by port 1 in configuration no. 1 at 2.45 GHz. (a) Without and (b) with inner filter.

It is also interesting to show the electric field distribution in the sample in order to get an idea of the influence of the filter. Thus, in Fig. 4.23 and Fig. 4.24 the magnitude of the electric field caused by port 1 at the surface of the plastic sample has been depicted for the two configurations under study. In both cases, the electric field distributions with and without inner filter are compared. It can be seen clearly the effect of the filter, dividing the cavity into independent sections to reduce the crosscoupling between both sides.

Finally, the influence of the metallic plate that holds the filter is studied in Fig. 4.25. The electric field distribution caused by port 1 at 2.45 GHz is depicted for three scenarios: without filter, with only the metallic plate and with the complete corrugated filter. In all these cases, an empty cavity is considered, although the distribution is represented at $y = 1.7$ cm which corresponds to the surface of the employed samples, in order to compare the results. It can be seen that most of the electric field is able to cross to the other side of the cavity when using only the metallic plate, therefore

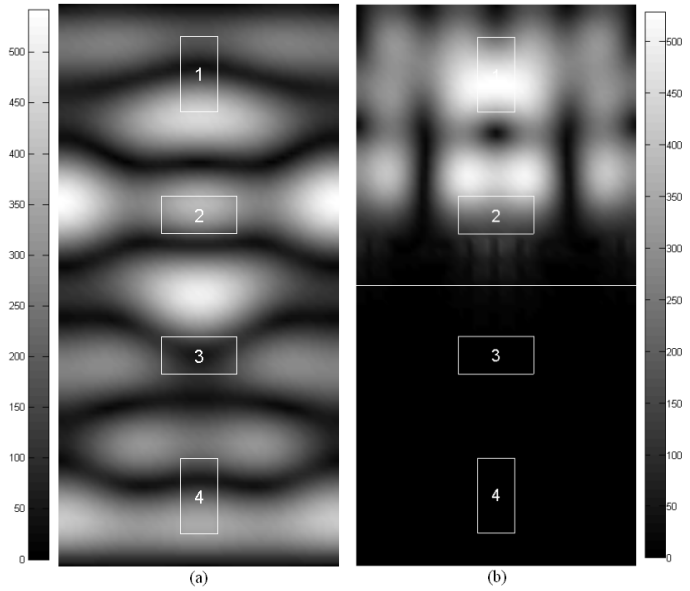

Figure 4.24: Electric field distribution in V/m on the surface ($y = 1.7$ cm) of the plastic sample ($\varepsilon_1' = 2$, $\tan\delta_1 = 0.01$) caused by port 1 in configuration no. 2 at 2.45 GHz. (a) Without and (b) with inner filter.

not reducing the crosscoupling levels. The only way to achieve this reduction is with the inner filter.

4.5 Compact microwave oven with hot and cold compartments for catering purposes

In sec. 3.8 it was described the design of a compact microwave-heating oven for catering purposes. In this section, simulations of the matching of the cavity (Fig. 4.26) and the electric field distribution (Fig. 4.27) are shown.

As it can be seen in both figures, the goals have been successfully achieved, obtaining a good matching at the frequency of interest and a proper separation between the hot and cold compartments thanks to the serrated choke.

4.6 Mutual influence between cavity and filter

In sec. 3.7 it was stated the need for studying the mutual influence between cavity and filter when designing this kind of structures.

Firstly, all the simulations have been performed without placing any material inside the heating cavity. We have compared the matching when the cavity is simulated

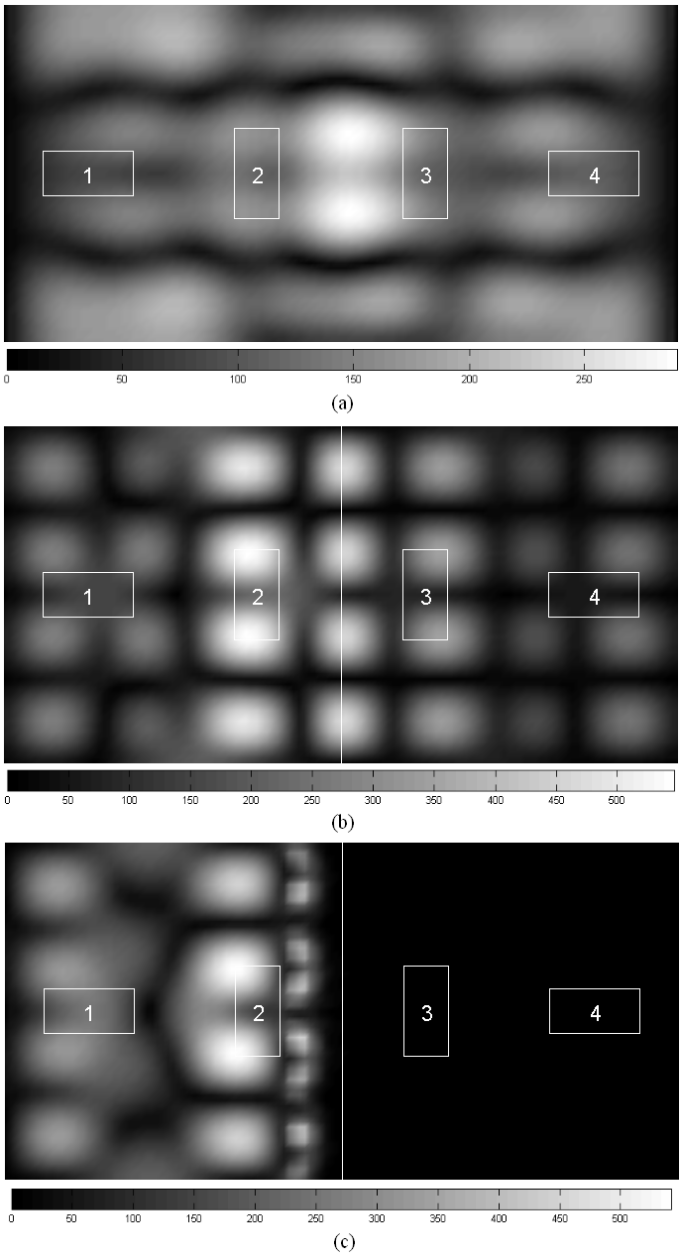

Figure 4.25: Electric field distribution in V/m at $y = 1.7$ cm caused by port 1 in configuration no. 2 at 2.45 GHz, for an empty cavity. (a) Without inner filter. (b) With only the PEC plate. (c) With inner filter.

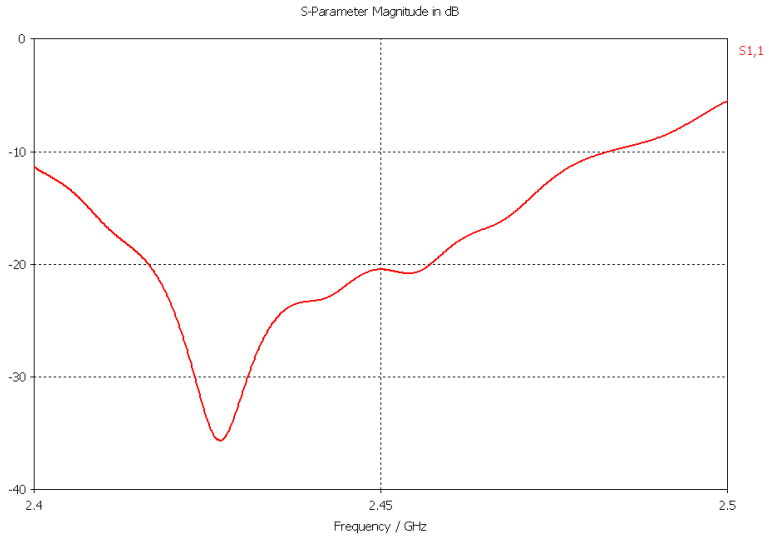

Figure 4.26: Simulation of the S_{11} parameter for the compact microwave oven.

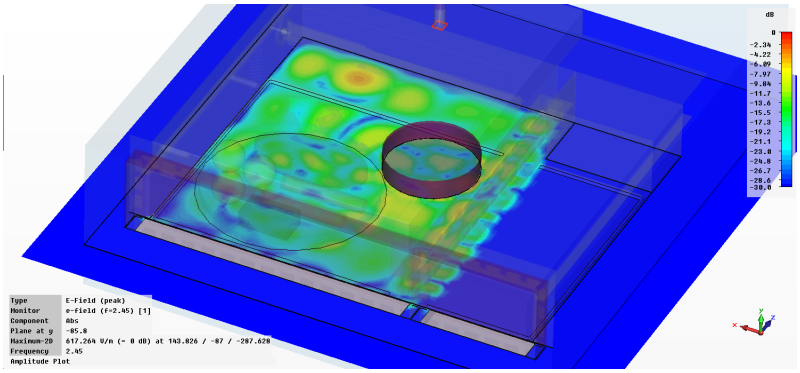

Figure 4.27: Electric field distribution within the compact microwave oven.

separately and when it is connected to the filter: the values of S_{11}^{11} the parameter at 2.45 GHz are -25.19 dB in the first case and -28.34 dB in the second case, so the matching is improved when connecting the filter in this case.

Regarding the transmission coefficient, the parameter of the filter considered separately is compared to the parameter, which is computed by simulating the whole system, for each one of the 5 modes which are propagating through the filter. In Fig. 4.28 it is shown the comparison of these two parameters for the fundamental mode TE_{10}. A summary of results at 2.45 GHz for the rest of the modes is shown in Tab. 4.20. Is must be pointed out that this comparison does not take into account the fact that only the fundamental mode is excited at port 1 and therefore the total energy is divided into the 5 propagating modes. In any case, even taking into account this effect, results are satisfactory.

The second simulated scenario consists of introducing a sheet of marble, with complex permittivity $\varepsilon_r = 9 \ \ j0.22$, as depicted in Fig. 3.26. In this case the S_{11}^{11} param-

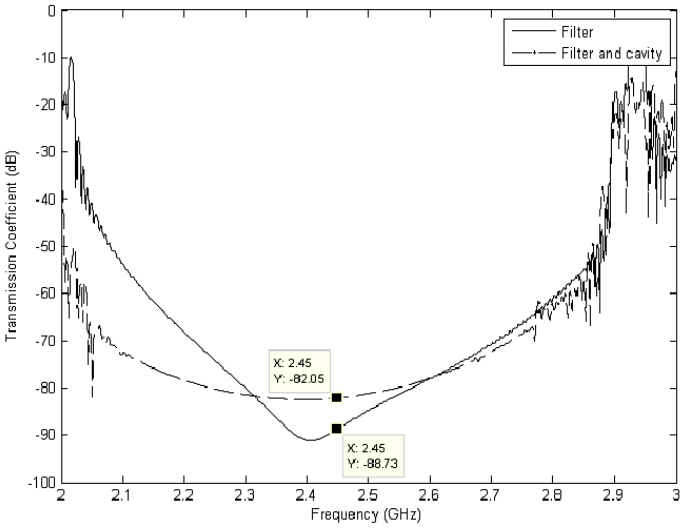

Figure 4.28: Comparison between the S_{21} parameter for the TE_{10} mode considering the filter separately and connected to the cavity.

Mode	Filter	Filter and cavity
TE_{10}	-88.73 dB	-82.05 dB
TE_{20}	-75.07 dB	-85.87 dB
TE_{30}	-78.87 dB	-87.88 dB
TE_{40}	-76.43 dB	-81.60 dB
TE_{50}	-65.12 dB	-90.21 dB

Table 4.20: Comparison between S_{21} parameters for each mode considering the filter separately and attached to the cavity.

eter at 2.45 GHz is -28.23 dB for the cavity and -31.54 dB for the whole system, obtaining again a slight improvement.

Regarding the transmission coefficients, Fig. 4.29 shows a comparison between both scenarios for the TE_{10} mode. In Tab. 4.21 the results for the rest of the modes are summarized.

It is also important to see how the electric field distribution changes when the filter is connected to the heating cavity due to the new modes which are excited because of the filter. In this way, in Fig. 4.30 and Fig. 4.31 the electric field distributions at 2.45 GHz in V/m on the surface of the sheet of marble are shown, when the cavity is simulated independently and when the filter is connected to the cavity, respectively.

The third considered simulation consists of introducing a sheet of wet clay, with complex permittivity $\varepsilon_r = 29.5\ \ j7.84$.

In this simulation the S_{11}^{11} parameter at 2.45 GHz is -25.74 dB for the cavity and

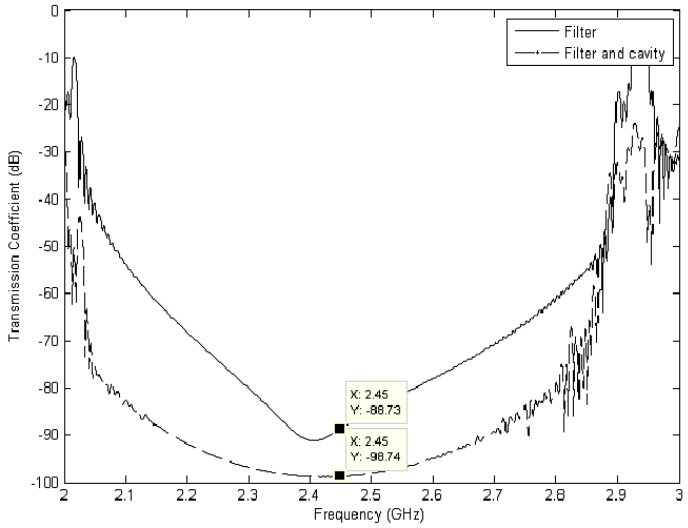

Figure 4.29: Comparison between the S_{21} parameter for the TE_{10} mode considering the filter separately and connected to the cavity, when introducing a sheet of marble inside the cavity.

Mode	Filter	Filter and cavity
TE_{10}	-88.73 dB	-98.74 dB
TE_{20}	-75.07 dB	-88.46 dB
TE_{30}	-78.87 dB	-102.6 dB
TE_{40}	-76.43 dB	-104.2 dB
TE_{50}	-65.12 dB	-105 dB

Table 4.21: Comparison between S_{21} parameters for each mode considering the filter separately and attached to the cavity when introducing a sheet of marble inside the cavity.

-27.53 dB for the whole system obtaining a similar improvement to the previous ones.

In Fig. 4.32 it can be seen a comparison between both scenarios for the TE_{10} mode. In Tab. 4.22 the results for the rest of the modes are shown. Results show that both the attenuation and the matching show good results for this material when simulating both parts together.

Finally, the last performed simulation consists of introducing a sheet of leather with complex permittivity $\varepsilon_r = 15\ \ j1.57$.

In this case the S_{11}^{11} parameter at 2.45 GHz is -25.43 dB for the cavity and -29.19 dB for the whole system, showing again a similar improvement. Regarding the transmission coefficients, in Fig. 4.33 it can be seen a comparison between both scenarios for the TE_{10} mode. Results for the rest of the modes are shown in Tab. 4.23. Again,

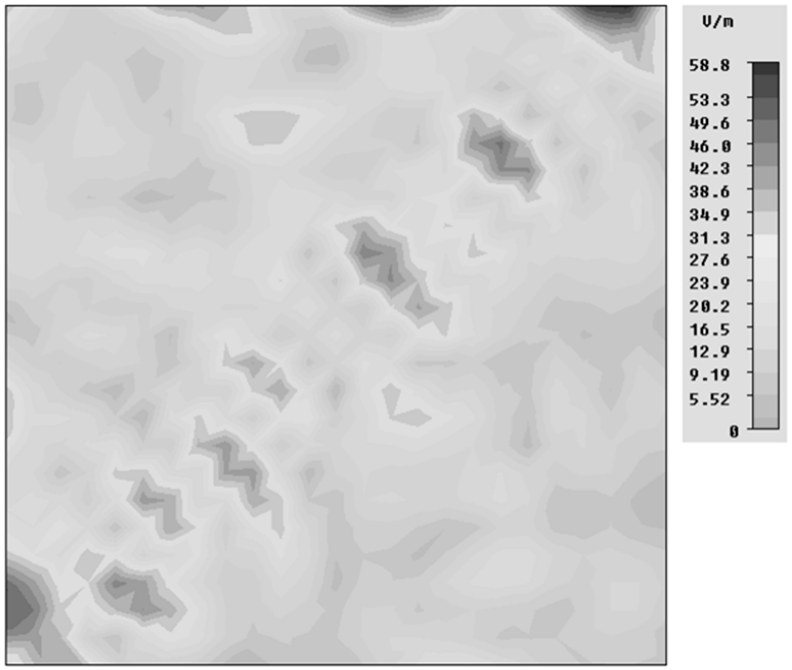

Figure 4.30: Electric field distribution in V/m at 2.45 GHz on the surface of the sheet of marble when the cavity is simulated independently.

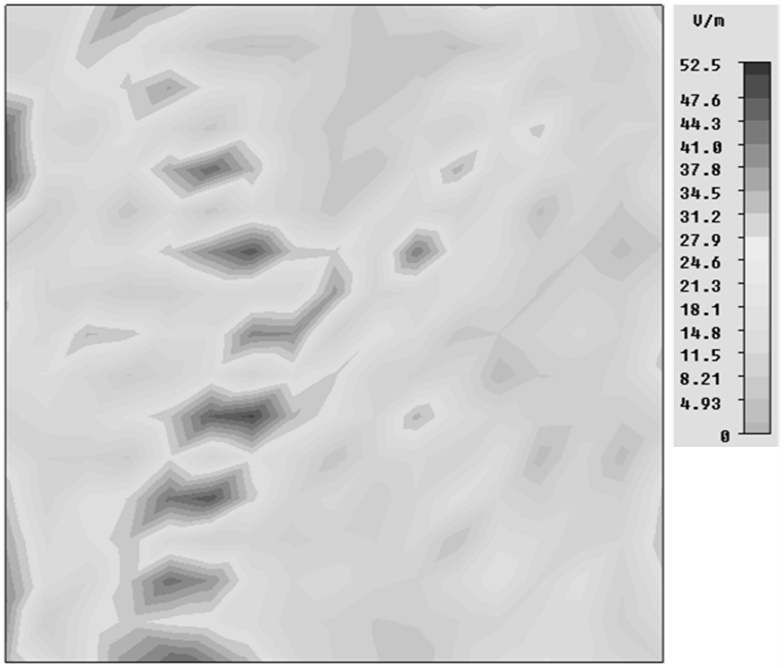

Figure 4.31: Electric field distribution in V/m at 2.45 GHz on the surface of the sheet of marble when cavity and filter are simulated together.

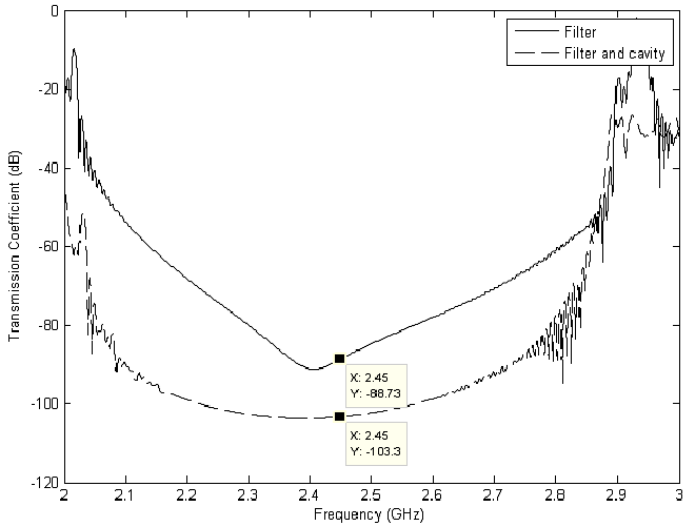

Figure 4.32: Comparison between the S_{21} parameter for the TE_{10} mode considering the filter separately and connected to the cavity, when introducing a sheet of wet clay inside the cavity.

Mode	Filter	Filter and cavity
TE_{10}	-88.73 dB	-103.3 dB
TE_{20}	-75.07 dB	-125.6 dB
TE_{30}	-78.87 dB	-106.6 dB
TE_{40}	-76.43 dB	-107.1 dB
TE_{50}	-65.12 dB	-98.87 dB

Table 4.22: Comparison between S_{21} parameters for each mode considering the filter separately and attached to the cavity when introducing a sheet of wet clay inside the cavity.

Mode	Filter	Filter and cavity
TE_{10}	-88.73 dB	-100.9 dB
TE_{20}	-75.07 dB	-113.15 dB
TE_{30}	-78.87 dB	-116.1 dB
TE_{40}	-76.43 dB	-104.3 dB
TE_{50}	-65.12 dB	-114.4 dB

Table 4.23: Comparison between S_{21} parameters for each mode considering the filter separately and attached to the cavity when introducing a sheet of leather inside the cavity.

results show that both parts of the microwave oven can be designed separately.

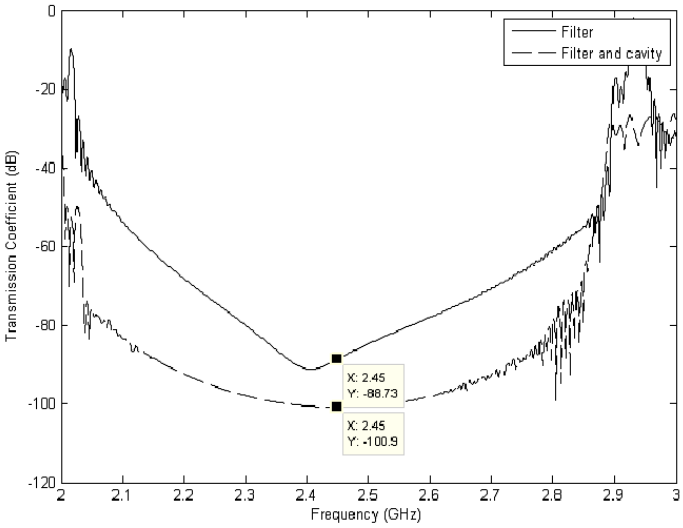

Figure 4.33: Comparison between the S_{21} parameter for the TE_{10} mode considering the filter separately and connected to the cavity, when introducing a sheet of leather inside the cavity.

All in all, a comparative study has been performed to obtain the influence that the fact of designing cavity and filter separately or together has on the performance of an industrial microwave oven. The study has been performed for different processed materials, with different dielectric properties. Results show that when the bandstop filter is designed independently, it can be guaranteed that the filter will continue working properly when connecting it to the heating cavity. Moreover, the electric field distribution on the sample is changed when connecting the filter, so this effect needs to be taken into account although it is beyond the scope of this thesis.

4.7 New self-configurable multimode filter

In sec. 3.5 it was presented a new self-configurable multimode filter prototype with metallic irises and automatically tunable posts (Fig. 3.15) along with a whole measurement setup and the pertinent optimization algorithms. In this section, results when applying the two different optimization schemes, i.e. genetic algorithms and parametric sweeps, are shown and properly explained.

4.7.1 Genetic algorithms

Fig. 4.34 shows the attenuation obtained when the optimization process is started with all post being unscrewed, resembling a hollow rectangular waveguide with irises. A general growing trend can be observed when incrementing the number of optimized

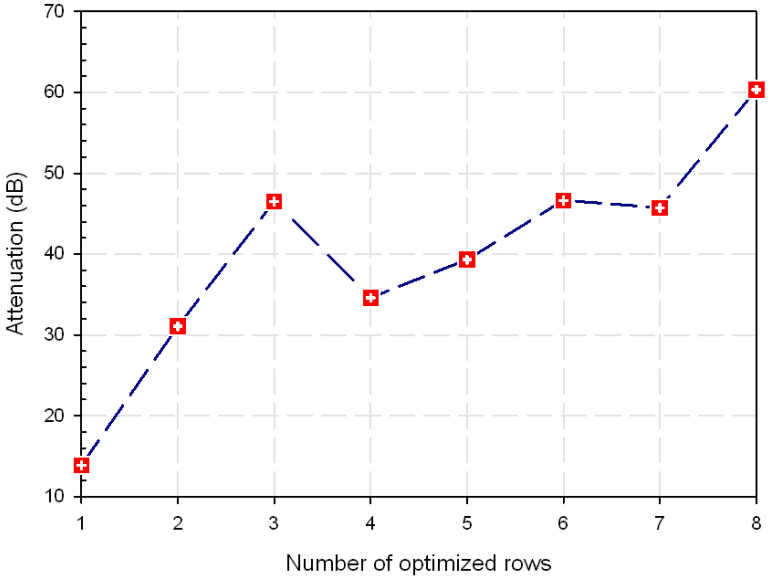

Figure 4.34: Attenuation in dB at 2.45 GHz when using GA starting with unscrewed posts.

rows, which seems logical since the optimization of each row starts from a point in which the attenuation is minimal. From this figure, one can conclude that the isolating effect of the irises on the filtering capabilities of the structure is minimum but, when combined with the tuning screws, good attenuation values can be obtained even for big apertures such as the one used in this work.

It can also be seen that the goal of obtaining an attenuation value greater than 60 dB has been achieved after the optimization of the eighth row, in particular 60.34 dB. In Tab. 4.24, the final penetration of the posts after the optimization process is shown. The penetration of the screws placed at rows 9 and 10 is zero since no optimization was longer necessary for them.

Fig. 4.35 shows the optimization process when the starting point corresponds to a configuration with all the posts introduced 28 mm in the filter. As it can be perceived, the optimization starts from quite a high attenuation value of 52.38 dB since all the posts are introduced in the filter. In this case, the GA finds much more difficult to obtain better solutions due to this highly resonant response, fact that is accentuated when all the posts are totally screwed. In any case, good attenuation values can still be found. In particular when optimizing the sixth row a value of 67.85 dB is obtained.

Sometimes the attenuation is reduced when optimizing the next row, since there is certain inaccuracy when changing the motorized posts from one row to the following one and when setting the optimum penetrations for the current row manually. The bandstop response of the filter is highly resonant and very sensitive to the positions

Input port										
	Col1	Col2	Col3	Col4	Col5	Col6	Col7	Col8	Col9	Col10
Row1	26.61	27.43	27.37	18.35	26.11	20.86	2.19	25.20	13.75	16.39
Row2	22.81	5.41	26.87	24.06	19.46	8.23	26.87	7.12	22.80	15.90
Row3	26.82	13.59	24.28	0.89	10.68	21.13	9.53	14.3	25.34	7.57
Row4	26.81	0	0.31	7.75	5.29	0.94	1.19	24.54	27.02	0.17
Row5	25.36	27.02	23.78	4.79	22.27	18.78	27.37	24.5	20.45	3.86
Row6	7.80	0	19.08	1.36	21.54	19.03	22.04	7.21	17.25	21.10
Row7	0	0.75	1.13	2.22	19.46	18.34	1.19	23.54	13.75	11.40
Row8	23.31	27.05	0.99	18.77	20.46	20.36	9.55	19.95	24.30	24.26
Row9	0	0	0	0	0	0	0	0	0	0
Row10	0	0	0	0	0	0	0	0	0	0
Output port										

Table 4.24: Penetration of the posts in mm when using GA starting with unscrewed posts.

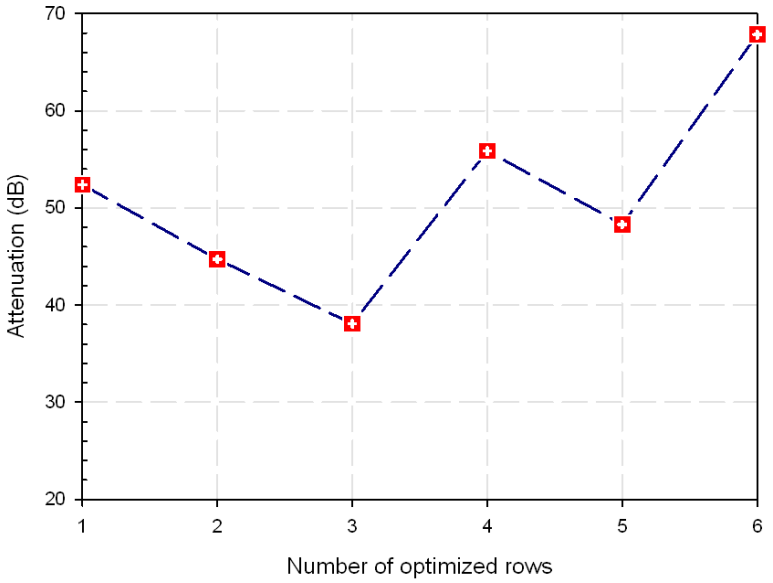

Figure 4.35: Attenuation in dB at 2.45 GHz when using GA starting with screwed posts.

Input port										
	Col1	Col2	Col3	Col4	Col5	Col6	Col7	Col8	Col9	Col10
Row1	7.80	4.22	21.00	1.29	21.93	21.03	22.04	5.21	18.15	21.10
Row2	0	0.25	0.13	0.29	0	1.19	1.19	0	0.33	25.68
Row3	25.36	4.41	27.87	1.89	11.93	21.13	14.17	3.88	7.32	16.39
Row4	25.33	25.89	23.50	18.97	6.63	19.97	5.82	16.16	17.45	17.94
Row5	8.80	4.22	19.00	0.79	21.68	19.03	21.04	7.71	17.25	21.10
Row6	7.80	26.02	22.18	10.98	19.46	1.19	3.33	19.57	22.80	23.26
Row7	28	28	28	28	28	28	28	28	28	28
Row8	28	28	28	28	28	28	28	28	28	28
Row9	28	28	28	28	28	28	28	28	28	28
Row10	28	28	28	28	28	28	28	28	28	28
Output port										

Table 4.25: Penetration of the posts in mm when using GA starting with screwed posts.

of the posts, so slight deviations from the optimum positions when operating with the posts manually may lead to lower attenuation levels. This fact is intended to be minimized in the following version of the prototype by automating the process of changing the stepper motors from one row to the next one. This automation is intended to be achieved by means of a motorized system that is able to move the set of ten stepper motors along the filter in a way that no human interaction is needed.

In Tab. 4.25, the optimum penetration of the posts after the optimization process when using GA starting with screwed posts is shown. Again, the screws of rows 7 to 10 kept their initial penetration values since their optimization was not necessary.

In this way, it seems that the best option is to optimize the filter using the configuration where all posts are screwed since it starts with higher attenuation values and fewer rows are needed to be optimized to achieve the goal. Furthermore, if the oven is continuously working at high power values it would be safer to start with high attenuation values in order to reduce the energy leakage as much as possible from the beginning.

4.7.2 Parametric sweeps

In Fig. 4.36 an example of a parametric sweep of one row is shown. In particular the one corresponding to the third row during the second sweep is shown, although the other rows show similar figures only changing the position of the minimum. As it can be seen, choosing the best position for the posts is very easy just by taking the depth that obtains minimum received power at the output monopole antenna.

Fig. 4.37 represents the attenuation for each of the three sweeps that have been

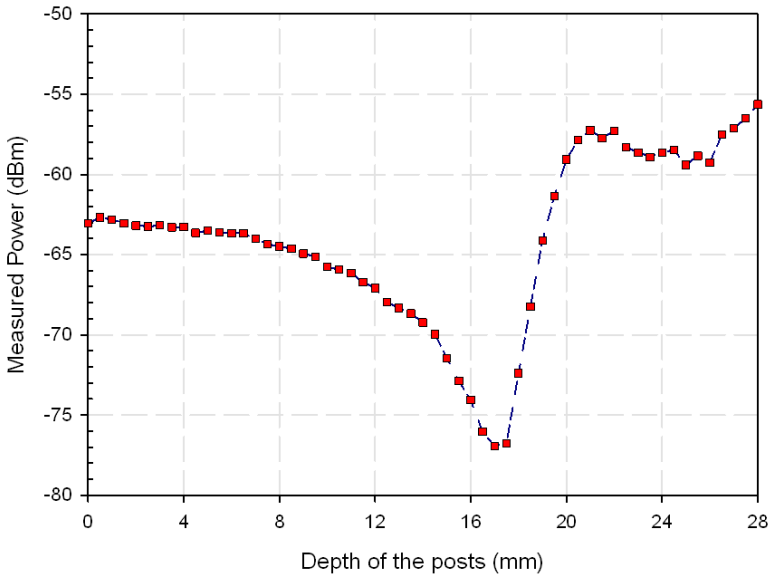

Figure 4.36: Example of a parametric sweep of one row of posts.

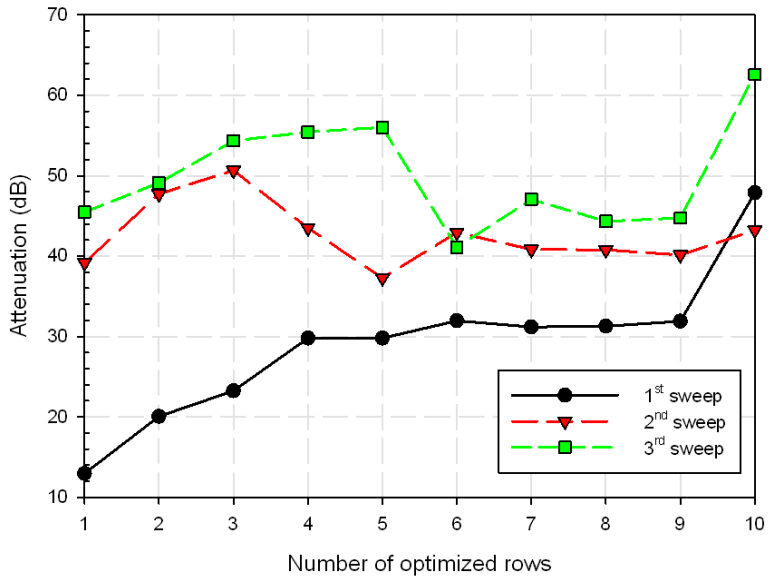

Figure 4.37: Attenuation in dB for the three parametric sweeps.

carried out. It is shown a growing trend in the attenuation when incrementing the number of optimized rows as shown with the GA optimization, but also when performing more sweeps. The second and third sweeps refine the previous solutions obtaining better attenuation results. In fact, after the third sweep a good attenuation value of 62.59 dB is obtained.

Input port			
	1st sweep	2nd sweep	3rd sweep
Row1	26.5	27	0.5
Row2	26.5	26.5	28
Row3	16.5	17	15
Row4	27	28	28
Row5	0	2	5.5
Row6	28	27	28
Row7	0	27.5	28
Row8	0	0.5	23
Row9	8.5	10	9
Row10	15	21.5	10
Output port			

Table 4.26: Penetration of the posts in mm for the three parametric sweeps.

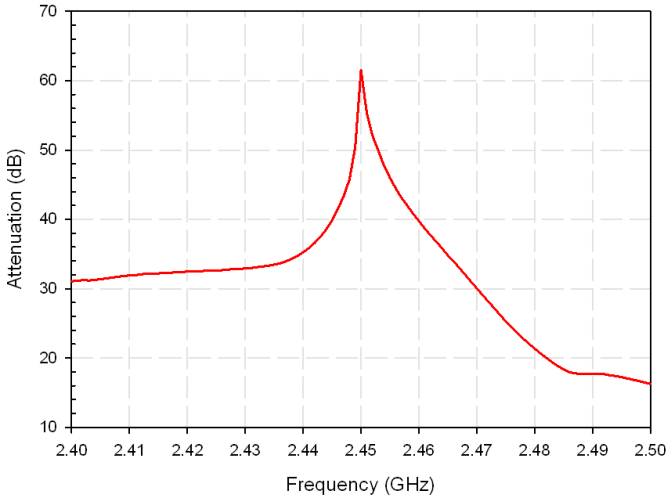

Figure 4.38: Attenuation in dB for the optimum configuration from 2.4 to 2.5 GHz.

The penetration of each row of posts after each sweep is shown in Tab. 4.26.

Once the optimum configuration has been obtained after the third sweep, a measurement of the attenuation from 2.4 to 2.5 GHz has been performed in order to see the bandwidth of the filter. As it can be seen in Fig. 4.38, the filter shows a highly resonant response since the optimization process has been performed at the single frequency of 2.45 GHz. Performing the optimization on a wider frequency range may improve the bandwidth of the filter. Nevertheless, the spectrum of a typical magnetron is quite narrow provided it is well matched and therefore the provided solution could be useful in real industrial applications.

4.7.3 Analysis of results

It must be pointed out that the $TE_{(2k)0}$ modes have not been considered neither in the feeding port nor in the output port, however the flexibility of the manufactured prototype allows us to extend the work to the full multimode approach.

Two different optimization and reconfiguration alternatives such as genetic algorithms and parametric sweeps have been evaluated. Regarding GA, two different alternatives have been assessed, i.e. starting the optimization process from the row nearest to the input port with all posts totally unscrewed or starting with all posts almost totally screwed and then applying a complete GA optimization stage. Results show that the best option is to optimize the filter using the configuration where all posts are totally screwed since it starts with higher attenuation values and fewer rows need to be optimized to achieve the goal. In addition, it is safer to start with high attenuation values in order to reduce the energy leakage as much as possible from the beginning.

Moreover, it has been shown that the asymmetric configurations for the metallic posts obtained by the GA can provide acceptable attenuations, which had not been proved before for this kind of filters.

Regarding the parametric sweep, it has been shown that good attenuation values can be obtained by using this approach. However, it is clear that GA are a better search strategy since the algorithm has more freedom when searching for the solution. In fact, the number of measurements that need to be done in order to achieve the goal is smaller than the case when using parametric sweeps. For instance, the number of total measurements for the GA optimization is 880 for the first scenario and 660 for the second scenario, whereas for the parametric sweep the number of total evaluations is 1710.

Design and optimization times are also remarkably reduced when using the proposed prototype compared to the traditional approach of using simulation software. For instance, the optimization time per row when using the manufactured filter is less than an hour, whereas optimizing one row with a simulator may take several tens of hours due to the large size and complexity of the structure. Finally, although the presented procedure is oriented to laboratory tests, it must be said that the same prototype and procedures with some minor adjustments can be applied to actual industrial microwave-heating ovens.

5 Results on the characterization of the coaxial to waveguide transitions

5.1 Overview

In this chapter, the results regarding the characterization of the coaxial-to-waveguide transitions and its applications are presented.

Firstly, the characterization of the WR-340 coaxial-to-waveguide transitions is shown and results are compared to different calibration algorithms depending on the number of calibration standards. Secondly, the results corresponding to the simultaneous evaluation of the transitions and a device under test are presented. Finally, obtained results when applied the proposed technique to the modelling of printed circuit boards inside metallic enclosures are shown.

5.2 Characterization of WR-340 coaxial-to-waveguide transitions

In sec. 2.5.1 and sec. 3.2 it was introduced a new inverse characterization technique in order to evaluate coaxial-to-waveguide transitions [1]. In this section, the accuracy of the proposed technique is evaluated as a function of the employed standards, and the obtained results are compared to those provided by different well known calibration algorithms.

Fig. 5.1 to Fig. 5.4 show the results for the characterization of transition 1 for both the magnitude and phase of S_{11} and $S_{12} \cdot S_{21}$ product when all short-circuits and lines (t, $l1$, $l2$, $s1$, $s2$, $s3$) (see Fig. 3.1) are used to evaluate the fitness function in (2.24). The results of this new inverse technique are compared to those ones provided by the three cavities method [2], TRL [3, 4], line-reflect-match (LRM) [5] and MultiCAL [6] and StatistiCAL [7] software packages. In the case of MultiCAL and StatistiCAL, the number and type of standards are the same as those used in the proposed calibrating technique. From these results it can be appreciated that all techniques show very good agreement. S_{22} offers very similar results to S_{11}. $S_{12} \cdot S_{21}$

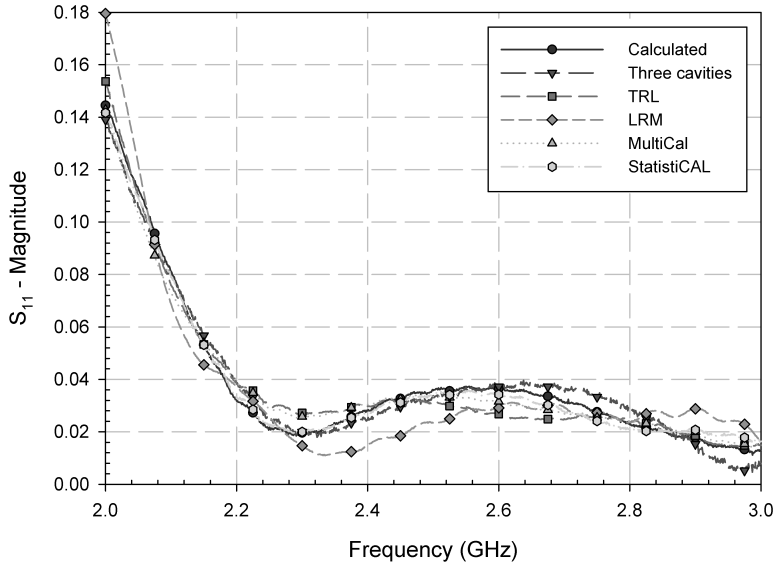

Figure 5.1: S_{11} results for transition 1 (magnitude).

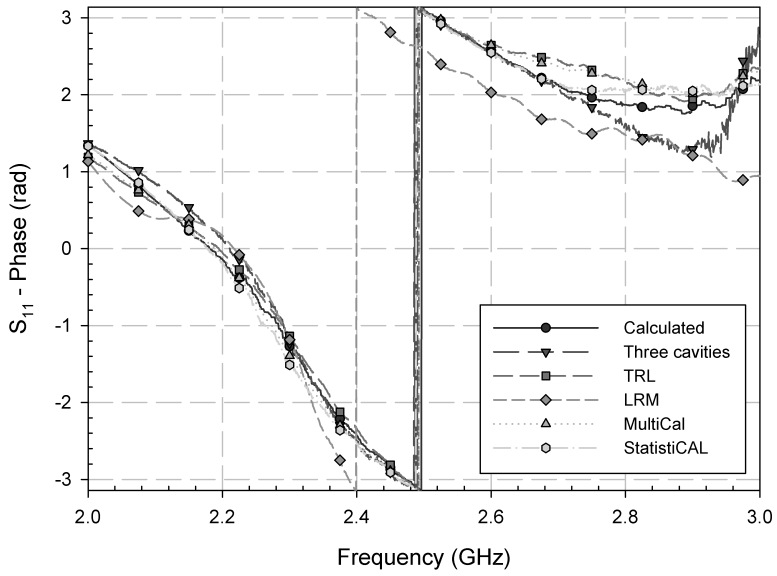

Figure 5.2: S_{11} results for transition 1 (phase).

product has been included in order to be able to compare the results to the three cavities technique described in [2].

From Fig. 5.1 and Fig. 5.2 one can deduce that the main source of error is provided by S_{11} phase uncertainties around 2.9 GHz due to the high degree of matching of the transition at those frequencies. However, this is common to all the used techniques

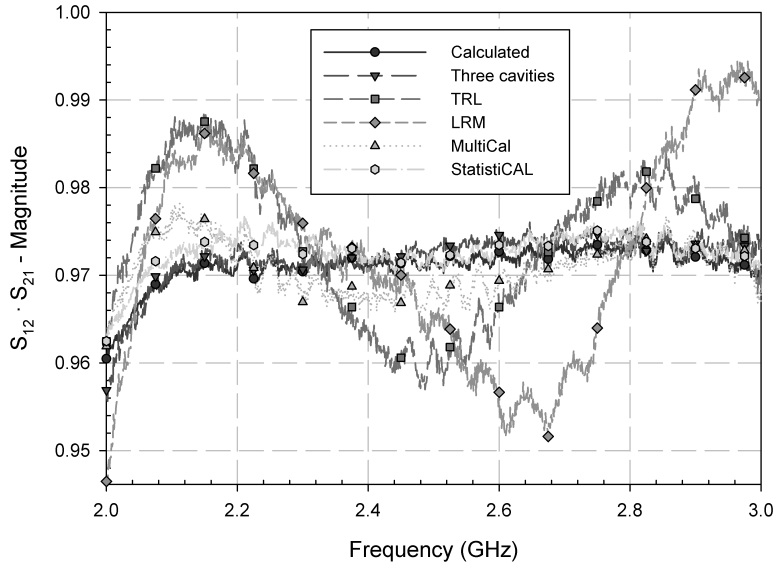

Figure 5.3: $S_{12} \cdot S_{21}$ results for transition 1 (magnitude).

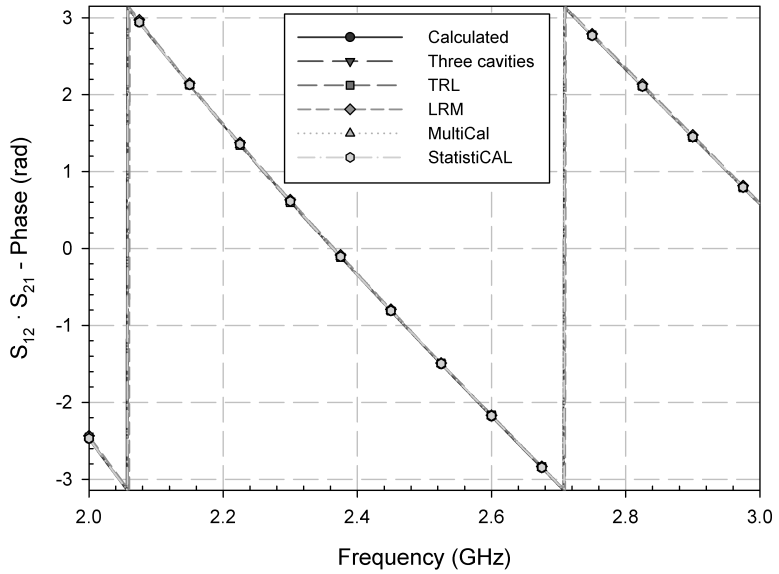

Figure 5.4: $S_{12} \cdot S_{21}$ results for transition 1 (phase).

Scenarios / Error	$\lvert S_{11}\rvert$	S_{11} phase (rad)	$\lvert S_{12} \cdot S_{21}\rvert$	$S_{12} \cdot S_{21}$ phase (rad)
t, $l1$, $l2$, $s1$, $s2$, $s3$	0.0036	0.1682	0.0012	0.0117
t, $l1$, $s1$, $s2$, $s3$	0.0034	0.1501	0.0010	0.0036
t, $l1$, $l2$, $s1$, $s2$	0.0046	0.1640	0.0023	0.0159
t, $l1$, $s1$, $s2$	0.0039	0.1440	0.0030	0.0061
t, $s1$, $s2$, $s3$	0.0025	0.1582	0.0019	0.0032
t, $l1$, $l2$, $s1$	0.0053	0.2293	0.0051	0.0165
t, $l1$, $l2$	0.0053	0.2563	0.0069	0.1612
$s1$, $s2$, $s3$	1.9×10^{-5}	0.0028	1.8×10^{-5}	2.4×10^{-5}
t, $l1$, $s1$	0.0053	0.2540	0.0066	0.0092
t, $s1$, $s2$	0.0060	0.2509	0.0070	0.0089
t, $l1$	0.0058	0.2558	0.0075	0.1925
$s1$, $s2$	0.1453	0.9644	0.1744	0.1771
t, $s1$	0.1983	0.3409	0.0360	6.1159
t	0.3281	0.7659	0.2404	0.2730
$s1$	0.3873	0.9957	0.3727	5.9391

Table 5.1: Average absolute error for different scenarios compared to three cavities technique.

and can be explained as follows: if noise level is near the reflected signal level then the actual value of the imaginary and real part of S_{11} would be poorly estimated whatever the used technique.

Tab. 5.1 shows the frequency average absolute error of the proposed technique when comparing to the three cavities method described in [2] for different standards combinations used during inverse measurement. Both magnitude and phase errors are provided for S_{11} and $S_{12} \cdot S_{21}$. Since there are many possible combinations just some of them have been evaluated.

The inverse technique provides very low absolute error values for S_{11} magnitude and $S_{12} \cdot S_{21}$ magnitude and phase when working with at least 3 different calibration standards. Again in this case the main error source is S_{11} phase due to its high level of matching.

Mixed combinations of shorts and thrus provide very similar results as long as there are enough conditions to obtain a valid solution.

As expected, the calibration with 3 shorts shows the minimum error values since the three cavities technique uses three shorts as calibration standards too [2]. However, very good results can be obtained even with different standards combinations as shown in Tab. 5.1.

When obtaining the transition S-parameters by using only 3 or 2 standards there are some problems to follow the phase of $S_{12} \cdot S_{21}$ function. Finally, from results obtained in Tab. 5.1, it is obvious that if there is not enough information the error

Scenarios / Error	$\lvert S_{11}\rvert$	S_{11} phase (rad)	$\lvert S_{12}\cdot S_{21}\rvert$	$S_{12}\cdot S_{21}$ phase (rad)
t, $l1$, $l2$, $s1$, $s2$, $s3$	0.0044	0.1315	0.0076	0.0107
t, $l1$, $s1$, $s2$, $s3$	0.0039	0.1346	0.0074	0.0102
t, $l1$, $l2$, $s1$, $s2$	0.0042	0.1447	0.0068	0.0105
t, $l1$, $s1$, $s2$	0.0030	0.1469	0.0062	0.0070
t, $s1$, $s2$, $s3$	0.0055	0.1929	0.0081	0.0106
t, $l1$, $l2$, $s1$	0.0048	0.1917	0.0029	0.0110
t, $l1$, $l2$	0.0027	0.0808	0.0109	0.1615
$s1$, $s2$, $s3$	0.0059	0.2563	0.0077	0.0107
t, $l1$, $s1$	0.0032	0.1939	0.0014	0.0026
t, $s1$, $s2$	0.0067	0.2856	0.0117	0.0127
t, $l1$	0.0002	0.0105	0.0122	0.1904
$s1$, $s2$	0.1434	0.7627	0.1797	0.1685
t, $s1$	0.1989	0.4225	0.0427	6.1215
t	0.3287	0.8964	0.2412	0.2794
$s1$	0.3829	0.7940	0.3758	5.9446

Table 5.2: Average absolute error for different scenarios compared to TRL calibration.

increases. This can be observed in the last four cases of Tab. 5.1. In those cases, the solution that minimizes the evaluation function cannot be reached by the proposed optimization algorithm.

Including intermediate restrictions in the cascading procedure for the transition parameters such as $|S_{ij}| \leq 1$ and $|S_{11}|^2 + |S_{12}|^2 \leq 1$ did not vary neither the error values nor convergence speed.

Tab. 5.2 has been obtained by comparing the solution obtained with the proposed technique to the solution obtained using a TRL calibration (t, $s1$, $l1$). The comparison has been carried out for the same set of combinations of standards as in Tab. 5.1. From obtained results it can be perceived that error values decrease when using (t, $s1$, $l1$) with the proposed technique as the same standards than TRL are being employed to obtain the solution. A similar behavior than Tab. 5.1 can be observed for the rest of combinations.

Tab. 5.3 shows the comparison of the results provided by the proposed characterization method and those obtained by using the StatistiCAL software package for different standards' combinations. This software package was not able to provide results when there were not enough calibration standards and consequently some comparisons were not possible. It must be remarked that shorts $s2$ and $s3$ were introduced as loads since StatistiCAL only allows one reflection standard.

From obtained results, it can be observed that errors are very similar to those provided by the comparison to the previous methods. However, StatistiCAL is not able to provide results for some standards combinations whereas the proposed method

Scenarios / Error	$\lvert S_{11}\rvert$	S_{11} phase (rad)	$\lvert S_{12} \cdot S_{21}\rvert$	$S_{12} \cdot S_{21}$ phase (rad)
t, $l1$, $l2$, $s1$, $s2$, $s3$	0.0020	0.0953	0.0016	0.0075
t, $l1$, $s1$, $s2$, $s3$	0.017	0.1301	0.0012	0.0027
t, $l1$, $l2$, $s1$, $s2$	0.0022	0.1112	0.0021	0.0095
t, $l1$, $s1$, $s2$	0.0025	0.1453	0.0018	0.0028
t, $s1$, $s2$, $s3$	0.0022	0.1305	0.0014	0.0035
t, $l1$, $l2$, $s1$	0.0031	0.2278	0.0020	0.0116
t, $l1$, $l2$	0.0009	0.0305	20.9473	2.5445
$s1$, $s2$, $s3$	-	-	-	-
t, $l1$, $s1$	0.0033	0.1932	0.0017	0.0026
t, $s1$, $s2$	0.0033	0.1645	0.0019	0.0071
t, $l1$	0.0002	0.0089	1.0068	2.5687
$s1$, $s2$	-	-	-	-
t, $s1$	-	-	-	-
t	-	-	-	-
$s1$	-	-	-	-

Table 5.3: Average absolute error for different scenarios compared to StatistiCAL software.

shows more flexibility in this field. Additionally for some standards (for instance when using only lines of different lengths) StatistiCAL is not able to properly characterize $S_{12} \cdot S_{21}$.

Therefore, we have observed several advantages of the proposed method versus StatistiCAL. Firstly, this software needs a good initial value to provide accurate results, mainly for phase estimations. In second place, the proposed method is able to handle more standards combinations without the need of an initial estimation for the transition scattering parameters. Additionally, the proposed method shows more flexibility in the error estimation since the evaluation function can be changed. StatistiCAL, however, shows lower computational times to provide the transition characterization. In fact, StatistiCAL showed computation times around 30 seconds in a 2 GHz Intel Core Duo processor.

Finally, Tab. 5.4 provides a comparison between the three cavities method, TRL, LRM, MultiCAL and StatistiCAL. In this case all the standards are employed for the proposed technique, MultiCAL and StatistiCAL. TRL and LRM have been implemented with the calibration standards (t, $s1$, $l1$) and (t, $s1$, $m1$) respectively, being $m1$ the measurements for the termination provided by the calibration kit. Differences for the phase value when using the LRM calibration can be observed in Fig. 5.2 for S_{11} and may be due to the limitations of the employed match as this adapted load behavior is not guaranteed for the entire frequency range under study [8]. The error is lower when comparing with the results provided by StatistiCAL and slightly increases when using MultiCAL. This can be explained by the StatistiCAL

Techniques / Error	$\lvert S_{11}\rvert$	S_{11} phase (rad)	$\lvert S_{12}\cdot S_{21}\rvert$	$S_{12}\cdot S_{21}$ phase (rad)
Three cavities	0.0036	0.1682	0.0012	0.0117
TRL	0.0044	0.1315	0.0076	0.0107
LRM	0.0082	0.4590	0.0102	0.0269
MultiCAL	0.0039	0.1230	0.0026	0.0039
StatistiCAL	0.0020	0.0953	0.0016	0.0075

Table 5.4: Average absolute error for scenario (t, $l1$, $l2$, $s1$, $s2$, $s3$) compared to differente techniques

robustness against noisy measurements [6]. As in the TRL technique there is no redundant information, the error increases slightly with respect to the methods developed at NIST. Similar error results are obtained for the explicit LRM and three cavities techniques.

5.3 Characterization of a DUT

The proposed inverse characterization technique can also be applied to simultaneously evaluate the transitions and a device under test [9]. In this case the unterminating procedure is carried out by minimizing the error between calculations of scattering matrix concatenations that contain the transitions and the DUT as unknown parameters and measurements of several structures that reproduce the calculated scenarios, as explained in sec. 2.5.2 and sec. 3.2.1.

Fig. 5.5 and Fig. 5.6 show the results for the transition 1 for both the magnitude and phase of S_{11} and $S_{12}\cdot S_{21}$ product when all short-circuits and thrus shown in Fig. 3.3 are used to evaluate the fitness function. The results of this inverse technique are compared to those provided by the three cavities method [2] for both transitions.

From these results it can be appreciated that both techniques show good agreement. An absolute average error of 0.0123 has been obtained for the S_{11} magnitude and 0.1318 rad for the phase when comparing with the three cavities method in the frequency range under study. $S_{12}\cdot S_{21}$ provides better results as an absolute average error of 0.0017 has been obtained for the magnitude and 0.1034 rad for the phase. S_{22} offers similar results to S_{11}.

In Fig. 5.7 and Fig. 5.8 results for the S-parameters (magnitude and phase) of the DUT are depicted, respectively. Calculated results with the proposed technique are compared to those experimental results obtained by using the waveguide calibration kit and to those simulated with CST MICROWAVE STUDIO®. To model the PTFE material the values $\varepsilon_r' = 2.05$ and $\tan\delta = 0.0002$ were included in the simulations.

An absolute average error of 0.0077 has been obtained for the S_{11} magnitude and 0.0263 rad for the phase when comparing with the waveguide calibration measurements in the frequency range under study. S_{21} provides an absolute average error

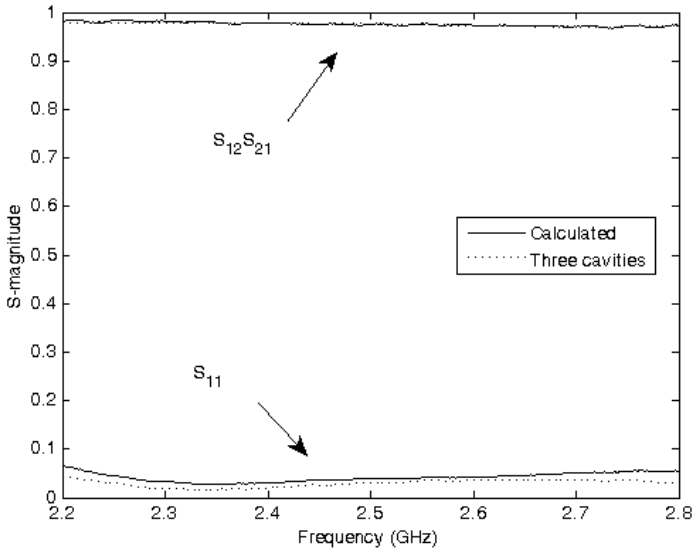

Figure 5.5: *S*-parameter magnitude for coaxial-to-waveguide transition 1.

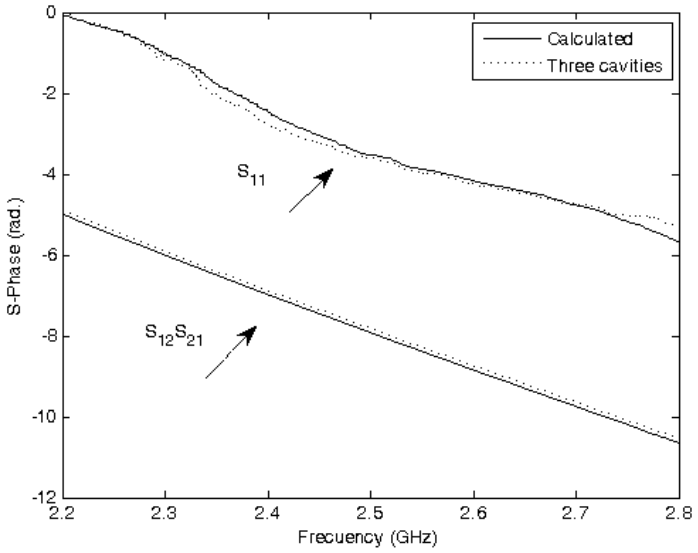

Figure 5.6: *S*-parameter phase for coaxial-to-waveguide transition 1.

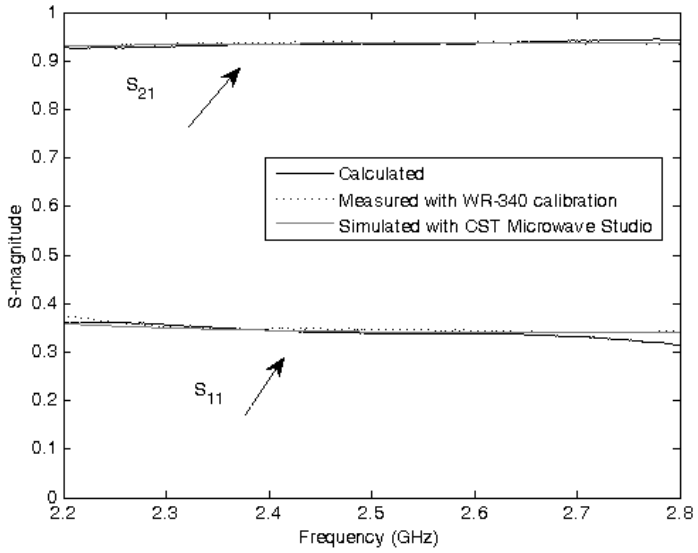

Figure 5.7: *S*-parameter magnitude for the device under test.

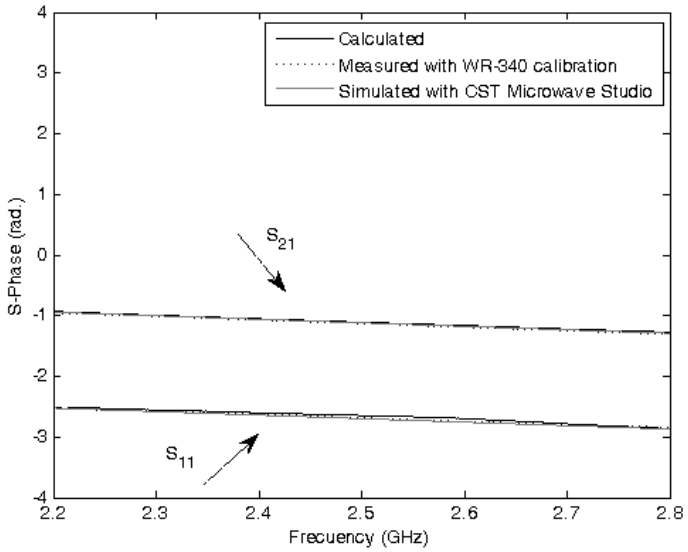

Figure 5.8: *S*-parameter phase for the device under test.

of 0.0039 for the magnitude and 0.0243 rad for the phase. Good agreement can be found for the three techniques (inverse procedure, simulations and DUT experimental measurements with waveguide calibration) showing that the proposed procedure can be successfully employed to obtain the coaxial-to-waveguide transitions and the DUT S-parameters.

5.4 Usage of transition characterization to model PCBs inside a metallic enclosure

In sec. 2.5.3 and sec. 3.2.2 it was described a new two-step procedure for obtaining PCB equivalent models by means of an inverse technique [10]. During the first step, the virtual coaxial-to-waveguide transitions used in the experimental measurements are fully characterized and their complex scattering matrices are obtained. Once the coaxial-to-waveguide transitions are characterized by the de-embedding technique, it is possible to obtain the PCB EM equivalent model by comparing the effects measured in the real enclosure loaded by the PCB and the ones computed in the virtual modeling.

Fig. 5.9 and Fig. 5.10 show the comparison of the S_{21} magnitude and phase obtained for the transition 1 using the proposed inverse technique and the three cavities method [2], respectively. As observed in both figures, both results agree very closely up to 1.25 GHz. Therefore, this comparison validates again the calibration procedure for the coaxial-to-waveguide transitions. It must be clarified that the results have been obtained by assuming a monomode propagation through the virtual waveguide thru, but frequency axis is ranging beyond the cut-off frequency of the second propagating mode (TE_{20}). As it was explained before, this mode is not excited since the coaxial probes are aligned properly at the centre of the cavity as seen in Fig. 3.4, so $TE_{(2m)0}$ modes will not be excited. Similar results were obtained for transition 2 and the rest of scattering parameters of transition 1.

The low levels for the $|S_{21}|$ parameter at lower frequencies lead to slightly different values for both solutions as can be seen in Fig. 5.9. As it was expected, the inverse technique provides higher accuracy and precision than the three cavities method, because that calibration process includes an additional thru measurement. As a consequence, the differences at lower frequencies shown in Fig. 5.9 are also reproduced in Fig. 5.10. This is emphasized by the phase ambiguity due to the low values of $|S_{21}|$.

Fig. 5.11 and Fig. 5.12 show the comparison of the S_{21} magnitude and phase for the empty enclosure scenario and for three different cases: measurements, simulation results obtained by CST MICROWAVE STUDIO® and the results obtained by concatenating the scattering matrices of coaxial-to-waveguide transitions and the waveguide thru. From these data it can be concluded that there is a close matching

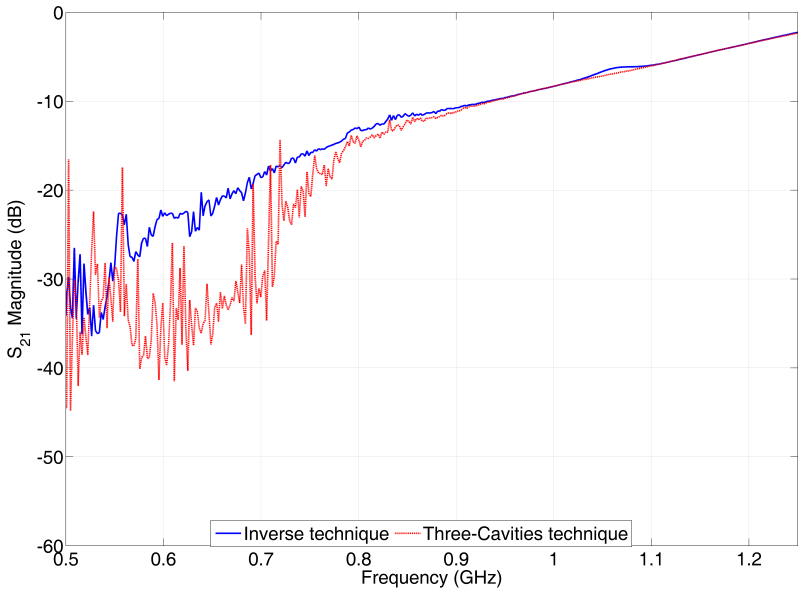

Figure 5.9: Comparison of the $|S_{21}|$ obtained for the transition 1 using the inverse technique and the three cavities method.

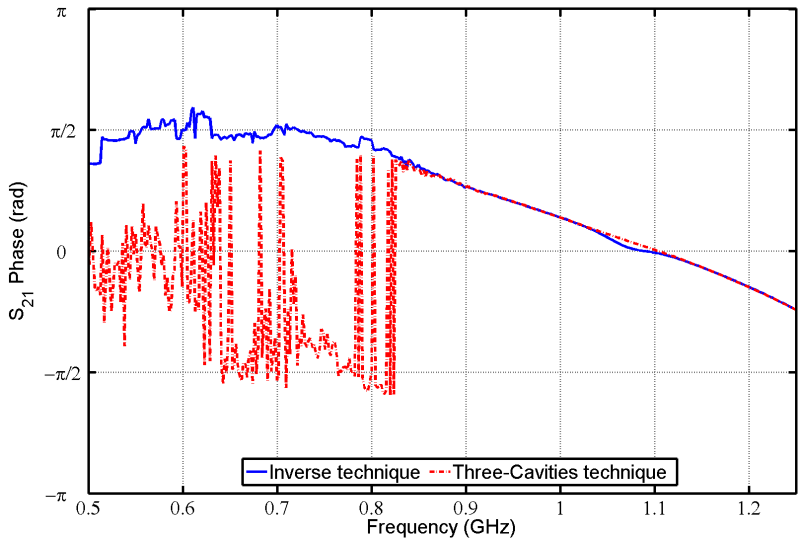

Figure 5.10: Comparison of the phase of S_{21} obtained for the transition 1 using the inverse technique and the three cavities method.

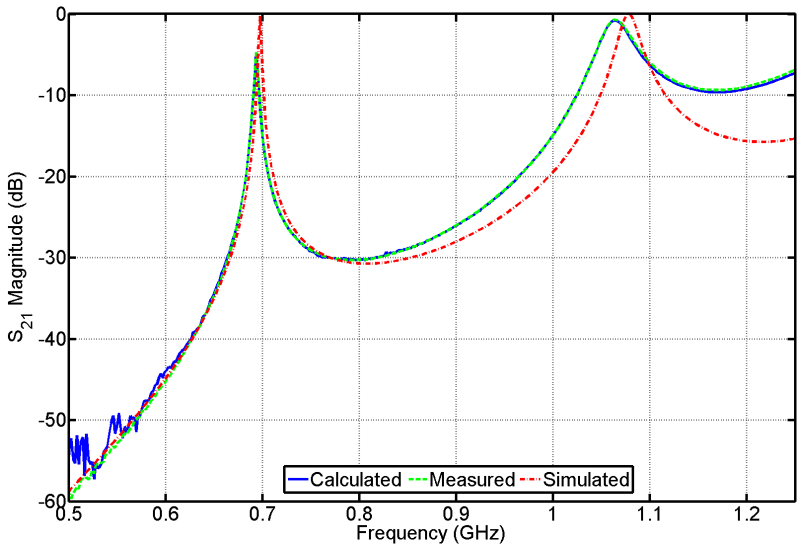

Figure 5.11: $|S_{21}|$ obtained for the empty enclosure.

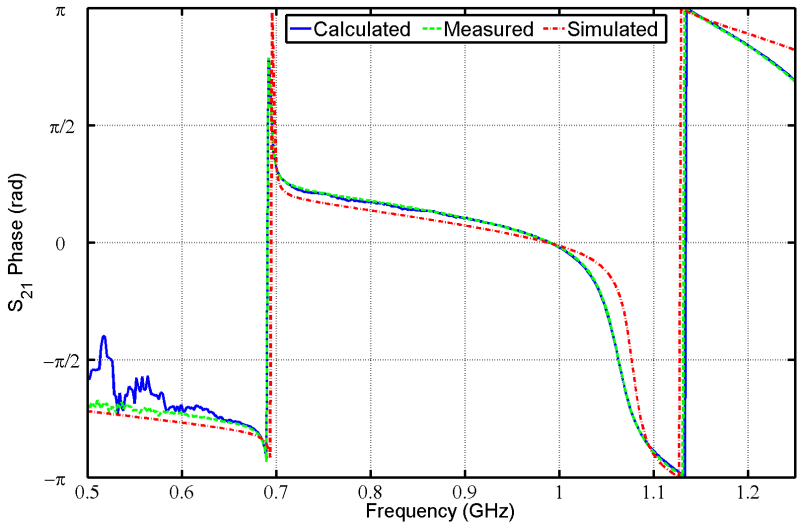

Figure 5.12: Phase of S_{21} obtained for the empty enclosure.

between the proposed method and the measurements as expected, since the measurements of the empty enclosure were employed in the inverse technique calibration process in order to extract the scattering parameters of the transitions used in the calculations. Therefore, this also shows that the proposed calibration technique allows a precise and accurate characterization of the transitions.

Differences between simulations and measurements start at the resonance frequency values and increase gradually with frequency. This is due to the fact that simulations do not properly model the effect of monopoles coupling and therefore, any attempt of deriving an equivalent model based only in simulations would require a very highly detailed model.

	f_{res} (MHz)	Q	$\|S_{21}\|$ (dB)
Calculated	694.03	210.6699	-4.7246
Measured	694.03	210.3262	-4.7101
Simulated	697.54	278.1030	-0.0340

Table 5.5: Empty cavity parameters for the first resonance.

Scenario	Algorithm	d (mm)	ε'_r	σ (S/m)	f_{pcb}
(a)	Sweep	3.778	3.000	0.0000	0.0313
	GA	2.911	4.914	0.0248	0.0315
	Gradient	3.804	2.748	0.0230	0.0335
(b)	Sweep	26.722	3.000	0.0667	0.0809
	GA	18.867	5.968	0.1447	0.0799
	Gradient	15.325	9.197	0.2732	0.0857
(c)	Sweep	30.000	1.000	0.0333	0.0858
	GA	7.119	1.290	0.3000	0.0877
	Gradient	29.996	1.140	0.1584	0.0865

Table 5.6: PCB equivalent models for different scenarios and optimization techniques.

Tab. 5.5 focuses on a comparison for the three traces shown in Fig. 5.11 and considers the quality factor, the resonance frequency and the maximum level for $|S_{21}|$ (dB). The values have been extracted using a quadratic interpolation [11]. Consequently, accurate modelling of the empty enclosure using the inverse technique guarantees the precise extraction of the PCB EM equivalent model.

Three different approaches for evaluating the PCB EM equivalent model performance were carried out: a vast sweep of the three model parameters, the solution obtained by the genetic algorithm and a solution obtained by a gradient based optimization technique. Tab. 5.6 shows the best solutions obtained for each approach stated above, including the evaluation of the fitness function. For the scenarios (a) and (b) the frequency range under evaluation was limited to [650, 750] MHz and [900, 960] MHz respectively, where the best monopole matching was found empirically under the monomode range (see Fig. 5.13 and Fig. 5.14). It can be concluded from these data that the three scenarios depicted in Fig. 3.5 produced different equivalents for the same PCB. In the case of scenario (c), despite the low values of the evaluation function the model was unable to reproduce the behaviour of the PCB inside the cabinet as it will be shown later.

Fig. 5.13 shows the measurement data of $|S_{21}|$ when placing the PCB as depicted in scenario (a). Also in Fig. 5.13, the results obtained for the PCB equivalent model obtained by using GA and the simulations results obtained when simulating the whole structure with CST are depicted. It must be remarked that in this last case, CST used the same optimized values that the proposed technique to calculate the

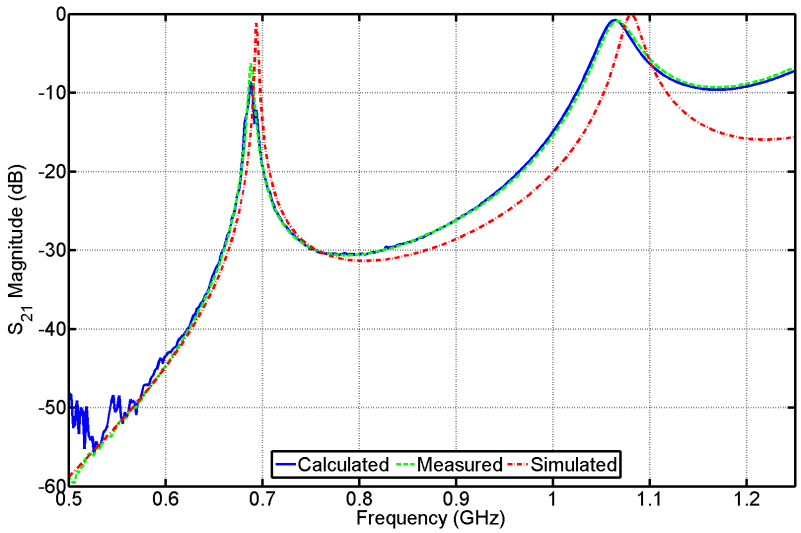

Figure 5.13: $|S_{21}|$ obtained for the scenario (a) with $d = 2.911$ mm, $\varepsilon'_r = 4.9148$ and $\sigma = 0.0248$ S/m for the PCB EM equivalent model versus CST simulations and measurements.

PCB model in order to observe the deviations of both approaches.

From the results, it can be concluded that the PCB model is capable of matching very closely the experimental data. On the contrary, when only using CST MICROWAVE STUDIO® software with the GA optimized data resonant frequencies and quality factors deviations are observed. Again those deviations are due to the effect of the monopole coupling. It must also be emphasized that in the scenario (a), the PCB position inside the cavity is not invasive enough to force a redistribution of the EM field energy within the enclosure. Consequently, resonances and levels for the S_{21} curve vary slightly when compared to the empty cavity situation, so this case could be treated using perturbational techniques. The opposite case is dealt with the scenario (b), where the PCB is placed in the middle of the enclosure where the most of the energy of the TE_{10} mode tends to concentrate when the enclosure is empty. However, besides the invasion of the PCB there is a vertical invariance due to its orientation.

Fig. 5.14 shows $|S_{21}|$ measured data, $|S_{21}|$ calculated by using the proposed technique and GA and the results obtained by simulating the whole structure with CST and the PCB optimized data. From obtained data it can be derived that in this scenario the PCB model and the proposed technique are capable of reproducing the first resonance getting close to the second resonance. When using the PCB model with CST the results are poorer than for the previous case.

Fig. 5.15 shows the $|S_{21}|$ measured data, $|S_{21}|$ obtained with the GA PCB EM equivalent model and the CST simulation for the scenario (c). As in previous cases, CST simulations of the whole structure made use of the same optimized parameters than those used in the proposed technique. From obtained data it can be concluded that

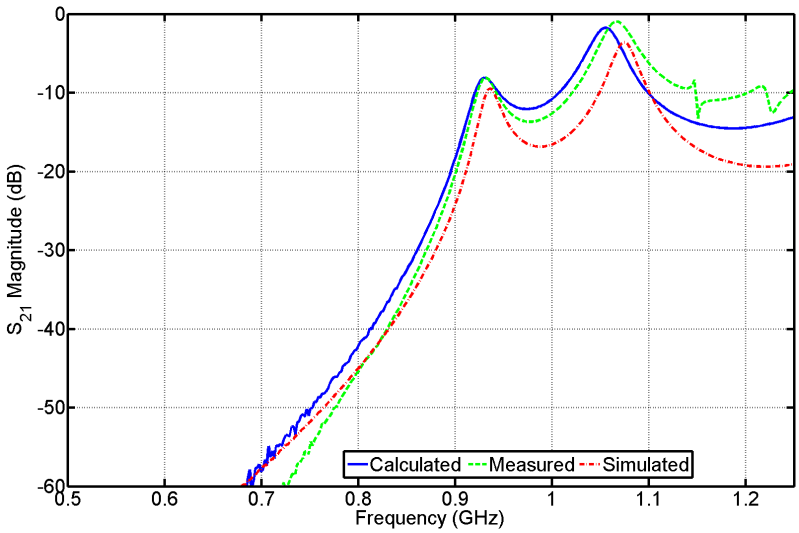

Figure 5.14: $|S_{21}|$ obtained for the scenario (b) with $d = 18.867$ mm, $\varepsilon_r' = 5.9683$ and $\sigma = 0.1447$ S/m for the PCB EM equivalent model versus CST simulations and measurements.

in this case the proposed method to extract the PCB EM equivalent model is not able to produce good results. This is due to the orientation of the PCB, which disrupts the vertical invariance along the y-axis becoming the most invasive scenario and producing higher order modes at the discontinuity that reach to the virtual ports of the central waveguide of Fig. 2.10. As it is known, TE_{10} mode exhibits vertical invariance, referred in this thesis as the y-axis. In the scenario (c) the PCB breaks up this condition as the PCB half fulfils the enclosure in height. To overcome this drawback it would be necessary to use a multimode calibration for both transitions and a multimode modelling for scenario (c). Since a monomode assumption has been used during all calculations the proposed technique is not able to produce good results for the first resonance.

The values of the optimization evaluation function computed by using the sweep algorithm for the scenario (a) are presented in Fig. 5.16 to Fig. 5.18, where it is shown a 2D representation of fpcb by fixing one of the PCB model parameters to its corresponding closest optimized value obtained by the genetic algorithm shown in Tab. 5.6. The same representations for the scenario (b) are shown in Fig. 5.19 to Fig. 5.21. The scale range for Fig. 5.16 to Fig. 5.21 has been fixed in order to appreciate the f_{pcb} behaviour differences of scenarios (a) and (b).

The sweep results obtained for scenario (a) at Fig. 5.16 to Fig. 5.18 show that the fitting function for the error (f_{pcb}) varies smoothly. This slow variation for scenario (a) can be explained by the fact that the PCB EM model is slightly perturbing the cavity electric fields. The stronger variation at these figures is shown in Fig. 5.17 where f_{pcb} is shown versus thickness and dielectric constant. Also in these figures one can perceive that several minima can be found and, therefore, many PCB EM

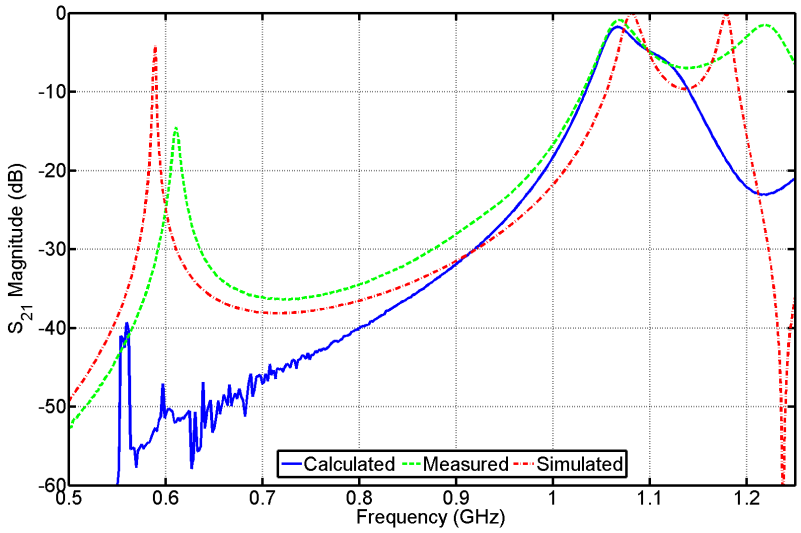

Figure 5.15: $|S_{21}|$ obtained for the scenario (c) with $d = 7.1191$ mm, $\varepsilon'_r = 1.2902$ and $\sigma = 0.3000$ S/m for the PCB EM equivalent model versus CST simulations and measurements.

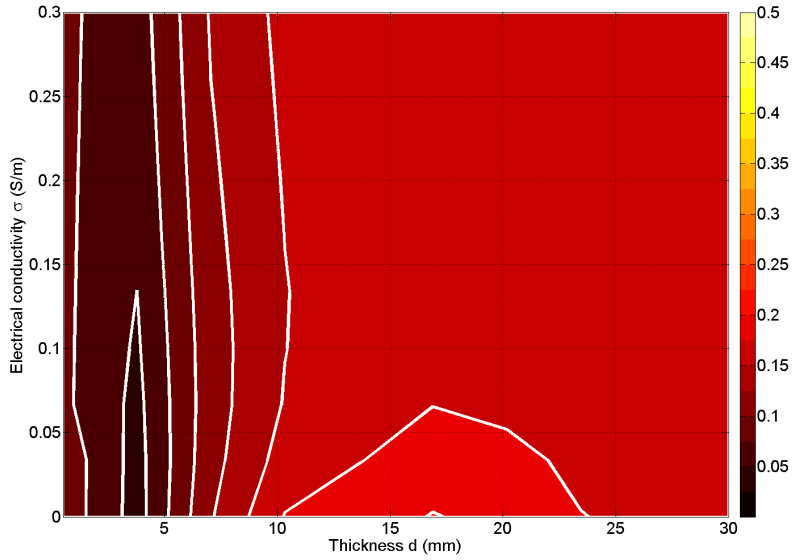

Figure 5.16: Results of the fitness function (f_{pcb}) versus PCB thickness and electrical conductivity for scenario (a). $\varepsilon'_r = 5$.

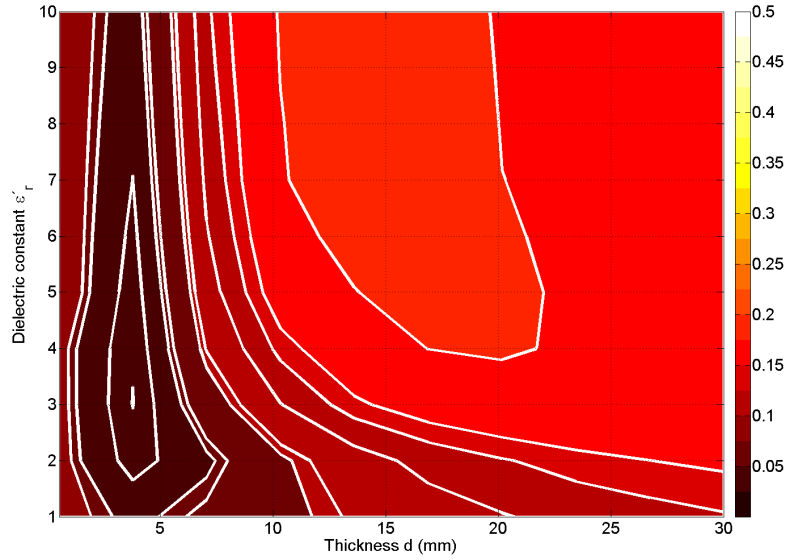

Figure 5.17: Results of the fitness function (f_{pcb}) versus PCB thickness and dielectric constant for scenario (a). $\sigma = 0.0333$ S/m.

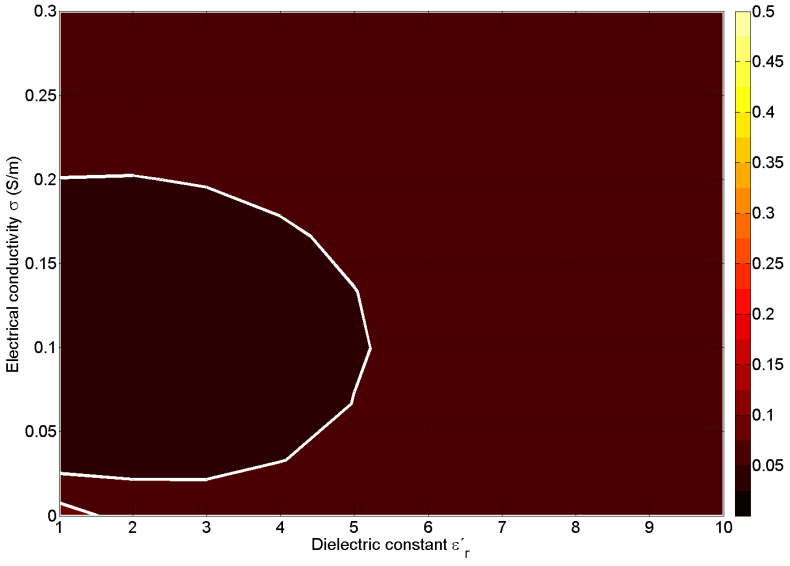

Figure 5.18: Results of the fitness function (f_{pcb}) versus PCB dielectric constant and electrical conductivity for scenario (a). $d = 3.778$ mm.

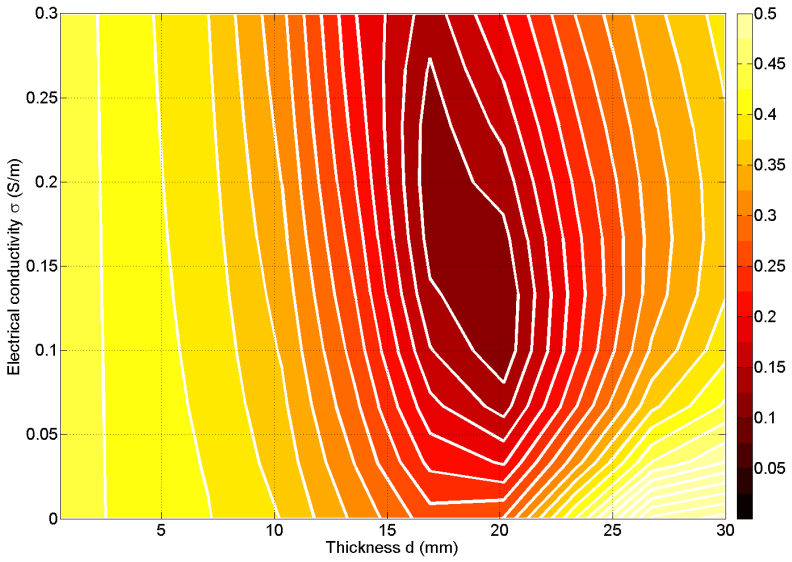

Figure 5.19: Results of the fitness function (f_{pcb}) versus PCB thickness and electrical conductivity for scenario (b). $\varepsilon'_r = 6$.

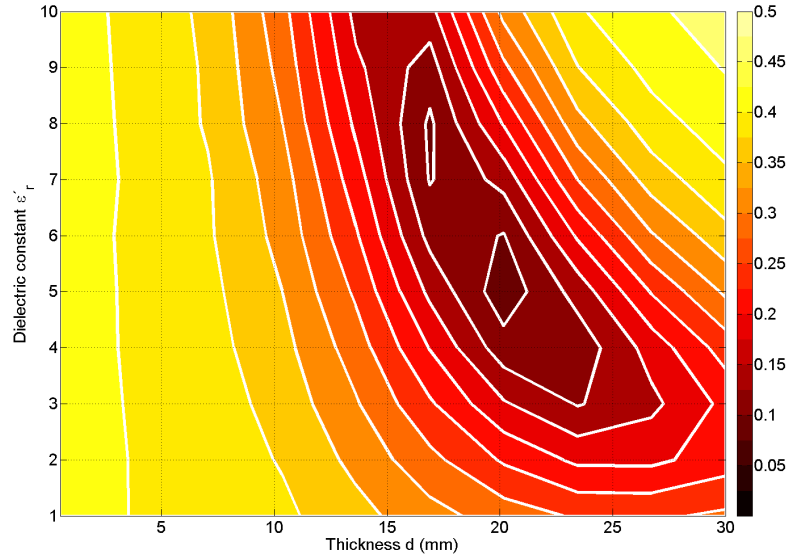

Figure 5.20: Results of the fitness function (f_{pcb}) versus PCB thickness and dielectric constant for scenario (b). $\sigma = 0.1333$ S/m.

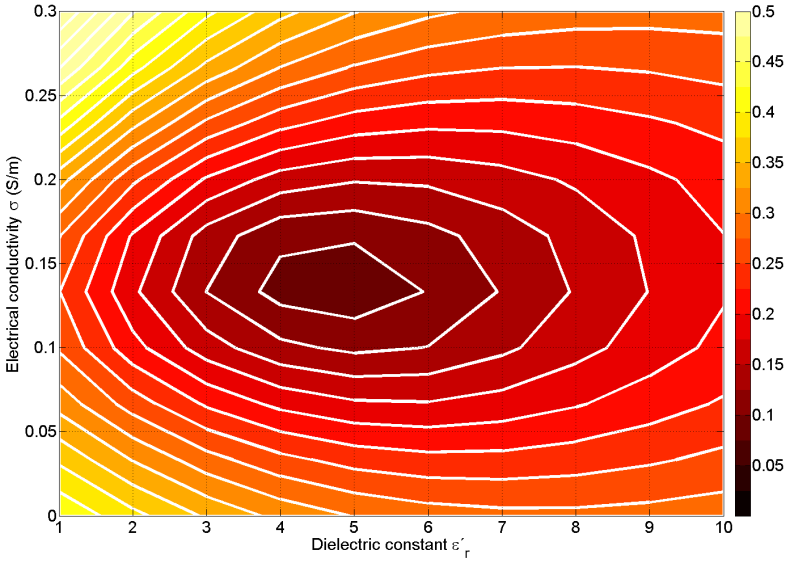

Figure 5.21: Results of the fitness function (f_{pcb}) versus PCB dielectric constant and electrical conductivity for scenario (b). $d = 20.167$ mm.

equivalent models are possible. As a consequence, global minimum search such as GA is important to find the best PCB model.

However, the behaviour of f_{pcb} for scenario (b) is quite different as shown in Fig. 5.19 to Fig. 5.21. In this case, f_{pcb} varies sharply with all variables. Only one area for minimum f_{pcb} values is found at Fig. 5.19 and Fig. 5.21 where this function is depicted for different thickness-electrical conductivity and thickness-dielectric constant pairs.

From obtained results with scenario (b) at Fig. 5.20 it can be derived that several combinations of thickness and dielectric constant values may provide similar values for f_{pcb} and consequently similar PCB EM equivalent models, at least to match the first resonance. This can be explained by the fact that the combination of both variables provides similar electrical volumes within the resonant cavity and, therefore, these combinations provide similar resonant frequencies. Again in the case of scenario (b), results indicate that it is important to use global optimization techniques to find the parameters of the optimized PCB EM model.

Finally, computation times obtained using CST Microwave Studio simulation tool lead to 31 seconds in the case of the trhu for the proposed technique in scenario (b) and 130 seconds for the whole enclosure set up. An Intel Core 2 Quad @ 2.66 GHz with 4 GB RAM was used during the simulations. Time benefits derived from the reduction in the computational domain in optimization processes are clearly justified.

All in all, results show that the proposed method increases the accuracy of the PCB EM equivalent model versus a model extracted only with simulations because

the effect of coaxial probes is not transferred to the PCB model. Simulations or analytical models may obtain very good results, but tolerances in the manufacturing of the device under test due to mechanization processes or soldering may lead to inaccuracies in their results. In this case, the effect can be particularly appreciated in the coupling levels for frequencies above 700 MHz.

Several combinations of thickness, dielectric constant and electrical conductivity values can provide very similar values for the equivalent model fitting. This is due to the fact that the dielectric constant and the dielectric volume of the PCB model establish the resonance frequency within the cavity whereas the electric conductivity and dielectric volume control resonance bandwidth. A strong correlation between the dielectric constant and the thickness of the model can also be observed.

Precise PCB EM equivalent models have been obtained for scenarios (a) and (b) where the perturbation introduced by PCB orientation did not generate an inter-modal energy scattering. It must be remarked that different PCB EM equivalent models were obtained for several PCB configurations within the enclosure. This means that the model is not an approximate geometrical model, but an accurate EM model considering the interactions with the enclosure.

However, for scenario (c) the proposed method failed due to the fact that the main considered hypothesis was monomode propagation at the virtual waveguide thru (TE_{10} in this case). A multimode version of the proposed techniques would be needed to reach a solution in this case.

Although applied to the extraction of the parameters of a PCB model, in a more general manner the technique could easily be applied to the dielectric characterization of materials.

5.5 Conclusions

A new two-tier inverse technique for characterizing coaxial-to-waveguide transitions based on the use of genetic algorithms and the gradient descent method has been described and compared to different well known calibration techniques. Very good results can be obtained by using several calibration standards such as short-circuits or waveguide lines.

Obtained results show that this inverse technique provides very similar results to those obtained by the reference algorithms, and additionally, is able to handle more calibration standards combinations provided that they can be properly included in S parameter cascade calculations.

In this work the studied frequency range has been restricted to the range provided by manufacturer in which the coaxial-to-waveguide transitions are assumed to work properly. This also ensures waveguide monomode conditions. However, wider frequency ranges and higher frequency points could be readily handled by the

proposed technique although this would lead to higher computing times. Moreover, the studied transitions showed non-resonant and well-matched behaviors. Resonant transitions are expected to produce sharper variations both in phase and magnitude values and, consequently, the proposed algorithm would very often use genetic algorithms to predict a reasonable initial point of the transition parameters at many frequency points. As a result, this would lead again to higher computing times than the ones obtained in this work.

Additionally, the proposed inverse technique has been successfully applied to the simultaneous characterization of the transitions and a device under test, and the extraction of PCB equivalent models, showing good results when compared to usual techniques.

Although applied to coaxial-to-waveguide transitions, this inverse technique can be extended to other transition types and, therefore, further research is envisaged in that direction.

Bibliography

[1] A. Lozano-Guerrero, F. J. Clemente-Fernández, J. Monzó-Cabrera, J. L. Pedreño Molina and A. Díaz-Morcillo, "Precise evaluation of coaxial to waveguide transitions by means of inverse techniques," IEEE Trans. Microwave Theory Tech., vol. 58, no. 1, pp. 229-235, Jan. 2010.

[2] J. F. Liang, H. Chang and K. A. Zaki, "Coaxial probe modeling in waveguides and cavities," IEEE Trans. Microw. Theory Tech., vol. 40, no. 12, pp. 2172-2180, Dec. 1992.

[3] G. F. Engen and C. A. Hoer, "Thru-Reflect-Line: an improved technique for calibrating the dual six-port automatic network analyzer," IEEE Trans. Microwave Theory Tech., vol. 27, no. 12, pp. 987-993, Dec. 1979.

[4] M. L. Edwards, "Calibration and Measurements of S-Parameters", Microwave & RF Circuits: Analysis, Design, Fabrication & Measurement, Chapter 7, Sep. 2001.

[5] K. Silvonen, "LMR 16 A self calibration procedure for a leaky network analyzer", IEEE Trans. Microwave Theory Tech., vol. 45, no. 7, pp. 1041-1049. Jul. 1997.

[6] D. F. Williams, C. M. Wang and U. Arz, "An optimal multiline TRL calibration algorithm", IEEE International Microwave Simposium Digest, vol. 3, pp. 1819-1822, June 2003.

[7] D. F. Williams, J. C. M. Wang and U. Arz, "An optimal vector-network-analyzer calibration algoritm," IEEE Trans. Microw. Theory Tech., vol. 51, no. 12, pp. 2391-2401, Dec. 2003.

[8] Waveguide Component Specifications and Design Handbook. Edition #7. Continental Microwave Division.

[9] A. Lozano-Guerrero, J. Monzó-Cabrera, F. J. Clemente-Fernández, J. L. Pedreño-Molina and A. Díaz-Morcillo, "Coaxial to waveguide transitions and device under test characterization by means of inverse techniques," Microwave Opt. Technol. Lett., vol. 52, no. 6, pp. 1294-1297, Jun. 2010.

[10] A. Lozano-Guerrero, J. Monzó-Cabrera, F. J. Clemente-Fernández, J. Fayos-Fernández, J. L. Pedreño-Molina and A. Díaz-Morcillo, "Electronic equivalent models for printed circuit boards inside a metallic enclosure using a coaxial-to-waveguide calibration," IEEE Trans. Electromagn. Compat., vol. 54, no. 4, pp. 931-939, Apr. 2012.

[11] M. P. Robinson and J. Clegg, “Improved determination of Q-factor and resonant frequency by a quadratic curve-fitting method”, IEEE Trans. Electromagn. Compat., vol.47, no. 2, pp. 399-402, May 2005.

6 Conclusions

6.1 Overview

The overall aim of this research was to improve the design and performance of the input and output waveguide bandstop filters for industrial microwave ovens when they are required to work with a continuous flow of the processed material. The motivation of this research came from a real problem experienced in industry when dealing with materials such as marble or granite, since it was observed that traditional filters did not work properly with these materials.

This chapter will summarize the findings of this research work, revisiting the research objectives given in the introductory chapter. First, we will review the contents of this study, outlining the main conclusions that were extracted from each chapter. Recommendations for future research will be discussed in the next section. Additionally, the final section contains a list of published work carried out during the course of candidature for the degree.

6.2 Summary

The first part of this dissertation presented the theoretical background needed for a full understanding of this research. An overview of the simulation and optimization techniques, along with a full description of the coaxial-to-waveguide transitions and bandstop filters employed throughout this thesis were described. The methods related to the analysis and study of this microwave devices were also presented.

In chapter 3 all the simulation and measurement scenarios were explained. Firstly, the measurements involved in the characterization of the coaxial-to-waveguide transitions were properly described, along with its applications to the characterization of a device under test and the modelling of printed circuit boards. Then, the simulation and measurements employed in the assessment of traditional corrugated filters were presented, along with some applications. Additionally, a new self-configurable multimode filter, which is the main contribution of this thesis, was also presented in this chapter.

In chapter 4 both traditional and new waveguide bandstop filters for use in industrial microwave-heating ovens were assessed. Firstly, the limitations of traditional reactive filters, i.e. singly and doubly corrugated filters, were presented, regarding

both the geometry and the dielectric properties of the processed material, showing that there is a wide range of materials which cannot be processed with traditional filters in a safe manner. These constraints were confirmed with simulations and measurements. Additionally, some alternatives based on resistive filters were also evaluated, showing serious limitations as well. Then, a new proposed filter based on irises and metallic posts was properly analyzed and validated, showing good attenuation results for all the problematic materials under study. Several novel applications of bandstop filters, such as the reduction of the crosscoupling or the separation into hot and cold compartments in a heating cavity, were also studied next, showing themselves as very useful for these applications. Finally, the results for the new self-configurable multimode filter based on irisis an automatically tunable posts were presented and properly validated.

In chapter 5 the results regarding the characterization of the coaxial-to-waveguide transitions and its applications were presented. Firstly, the characterization of the WR-340 coaxial-to-waveguide transitions was shown and results were compared to different calibration algorithms depending on the number of calibration standards, showing that this inverse technique provides very similar results to those obtained by the reference algorithms, and additionally, is able to handle more calibration standards combinations provided they can be properly included in S-parameter cascade calculations. Secondly, the results corresponding to the simultaneous evaluation of the transitions and a device under test were presented, showing that the proposed technique can be successfully employed to obtain the coaxial-to-waveguide transitions and the DUT S-parameters. Finally, obtained results when applied the proposed technique to the modelling of printed circuit boards inside metallic enclosures were obtained, showing that precise PCB EM equivalent models can be obtained by using the proposed technique.

6.3 Further work

Following the investigations described in this thesis, the main lines of research that remain open are listed below:

- Multimode characterization of the coaxial-to-waveguide transitions: The methodology proposed in this thesis could be expanded in order to characterize coaxial to waveguide transitions in a multimode range. The bandwidth of standard rectangular waveguides is limited to an octave when monomode conditions are to be maintained. However, in some situations it might be interesting to make use of the expanded transmission capabilities of waveguides when they operate handling several modes: electric permittivity and magnetic permeability measurements using waveguides is restricted to the monomode propagation condition, but overcoming this limitation might be very advantageous for broadening the measurement bandwidth.

- Full multimode evaluation of the self-configurable filter: In the results presented in this thesis, the $TE_{(2k)0}$ modes have not been considered neither in the feeding port nor in the output port, however the flexibility of the manufactured prototype allows us to extend the work to the multimode approach by placing more antennas and replacing the optimization algorithms with multi-objective algorithms, for instance. Moreover, optimizations over a wider frequency range might improve the bandwidth of the filter, so further work could be carried out in this direction.
- Full automation of the self-configurable prototype: The bandstop response of the filter is highly resonant and very sensitive to the positions of the posts, so slight deviations from the optimum positions when operating with the posts manually may lead to lower attenuation levels. This fact could be minimized by automating the process of changing the stepper motors from one row to the next one. This automation could be achieved by means of a motorized system that is able to move the set of ten stepper motors along the filter in a way that no human interaction is needed.

6.4 List of publications

6.4.1 Refereed ISI journals

- A. Lozano-Guerrero, **F. J. Clemente-Fernández**, J. Monzó-Cabrera, J. L. Pedreño Molina and A. Díaz-Morcillo, "Precise evaluation of coaxial to waveguide transitions by means of inverse techniques", IEEE Transactions on Microwave Theory and Techniques, vol. 58, no. 1, Jan. 2010.
- A. Lozano-Guerrero, J. Monzó-Cabrera, **F. J. Clemente-Fernández**, J. L. Pedreño-Molina and A. Díaz-Morcillo, "Coaxial to waveguide transitions and device under test characterization by means of inverse techniques", Microwave and Optical Technology Letters, vol. 52, no. 6, Jun. 2010.
- **F. J. Clemente-Fernández**, J. Monzó-Cabrera, J. L. Pedreño-Molina, A. J. Lozano-Guerrero and A. Díaz-Morcillo, "Analysis of reactive and resistive open waveguide filters for use in microwave-heating applicators", COMPEL: The International Journal for Computation and Mathematics in Electrical and Electronic Engineering, vol. 30, no. 5, pp. 1606-1615, Oct. 2011.
- **F. J. Clemente-Fernández**, J. Monzó-Cabrera, J. L. Pedreño-Molina, A. Lozano-Guerrero, J. Fayos-Fernández and A. Díaz-Morcillo, "A new sensor-based self-configurable bandstop filter for reducing the energy leakage in industrial microwave ovens", Measurement Science and Technology, vol. 23, Jun. 2012.

- **F. J. Clemente-Fernández**, J. Monzó-Cabrera, J. M. Catalá-Civera, J. L. Pedreño-Molina, A. Lozano-Guerrero and A. Díaz-Morcillo, "Waveguide band-stop filter based on irises and double corrugations for use in industrial microwave ovens", Electronics Letters, vol. 48, no.13, pp. 772-774, Jun. 2012.
- A. Lozano-Guerrero, J. Monzó-Cabrera, **F. J. Clemente-Fernández**, J. Fayos-Fernández, J. L. Pedreño-Molina and A. Díaz-Morcillo, "Electronic equivalent models for printed circuit boards inside a metallic enclosure using a coaxial-to-waveguide calibration", IEEE Transactions on Electromagnetic Compatibility, vol. 54, no. 4, Aug. 2012.

6.4.2 Non-ISI Journals

- J. L. Pedreño-Molina, J. Monzó-Cabrera, A. Díaz-Morcillo, A. Lozano-Guerrero and **F. J. Clemente-Fernández**, "MICRODES@: una herramienta software para el diseño automatizado de hornos industriales de microondas", Espacio-Teleco, Revista de la ETSIT-UPCT, vol. 1, pp. 117-122, Mar. 2010.
- **F. J. Clemente-Fernández**, A. Murcia-Andreu, J. Monzó-Cabrera, J. L. Pedreño-Molina, A. Lozano-Guerrero and A. Díaz-Morcillo, "Evaluación de nuevas topologías de filtros doblemente corrugados en guía de onda", Jornada de Introducción a la Investigación de la UPCT, vol. 3, pp. 89-91, May 2010.
- **F. J. Clemente-Fernández**, J. Monzó-Cabrera, J. L. Pedreño-Molina, A. Lozano-Guerrero and A. Díaz-Morcillo, "Diseño y construcción de un sistema de medida de potencia para la configuración de filtros para hornos industriales de microondas", Espacio-Teleco, Revista de la ETSIT-UPCT, vol. 2, pp. 21-29, May 2011.
- **F. J. Clemente-Fernández**, F. Ortega-del-Nido, J. Monzó-Cabrera, J. L. Pedreño-Molina, A. Lozano-Guerrero and A. Díaz-Morcillo, "Efectos mutuos entre aplicadores industriales de microondas y filtros doblemente corrugados", Jornada de Introducción a la Investigación de la UPCT, vol. 4, pp. 100-102, May 2011.
- **F. J. Clemente-Fernández** and Rocío Murcia-Hernández, "Evaluación de una nueva topología de filtro elimina-banda auto-configurable para su uso en hornos industriales de microondas", Jornada de Introducción a la Investigación de la UPCT, vol. 5, pp. 99-101, May 2011.

6.4.3 Papers in international conferences

- **F. J. Clemente-Fernández**, J. Monzó-Cabrera, J. L. Pedreño-Molina, A. Lozano-Guerrero, and Alejandro Díaz-Morcillo, "Analysis of reactive and resistive open waveguide filters for use in microwave-heating applicators", HES-

10 - International Symposium on Heating by Electromagnetic Sources, Padova (Italy), vol. 1, pp. 385-392, 2010.

- A. Lozano-Guerrero, J. Monzó-Cabrera, **F. J. Clemente-Fernández**, J. L. Pedreño-Molina and Alejandro Díaz-Morcillo, "Evaluation of dielectric mode-stirrers for electric field uniformity within multimode microwave ovens", AMPERE 2011 13th International Conference on Microwave and High Frequency Heating, Toulouse (France), vol. 1, pp. 348-351, 2011.
- **F. J. Clemente-Fernández**, J. Monzó-Cabrera, J. L. Pedreño-Molina, A. Lozano-Guerrero and Alejandro Díaz-Morcillo, "Crosscoupling reduction in multifed multimode microwave-heating cavities by means of inner doubly corrugated filters", AMPERE 2011 13th International Conference on Microwave and High Frequency Heating, Toulouse (France), vol. 1, pp. 352-354, 2011.
- **F. J. Clemente-Fernández**, J. Monzó-Cabrera, J. L. Pedreño-Molina, A. Lozano-Guerrero, M. A. García-Fernández, and Alejandro Díaz-Morcillo, "Mutual influence between cavity and filter on the design of industrial microwave ovens", AMPERE 2011 13th International Conference on Microwave and High Frequency Heating, Toulouse (France), vol. 1, pp. 379-381, 2011.
- **F. J. Clemente-Fernández** and Rocío Murcia-Hernández, "Microwaves as energy source in engineering, industrial and medical applications", 4th EMUNI Research Souk, Cartagena (Spain), vol. 1, pp. 395-404, 2012.
- **F. J. Clemente-Fernández**, J. Monzó-Cabrera, J. L. Pedreño-Molina, Rocío Murcia-Hernández, A. Lozano-Guerrero, J. Fayos-Fernández and Alejandro Díaz-Morcillo, "Experimental evaluation of a new self-configurable waveguide bandstop filter for use in continuous-flow microwave ovens", 2nd Global Conference on Microwave Energy Applications, Long Beach (USA), 2012.
- **F. J. Clemente-Fernández**, J. Monzó-Cabrera, J. L. Pedreño-Molina, Rocío Murcia-Hernández, A. Lozano-Guerrero, J. Fayos-Fernández and Alejandro Díaz-Morcillo, "Limitations of doubly corrugated bandstop filters for use in continuous microwave-heating processes", 2nd Global Conference on Microwave Energy Applications, Long Beach (USA), 2012.
- A. Lozano-Guerrero, J. Monzó-Cabrera, **F. J. Clemente-Fernández**, J. Fayos-Fernández, Rocío Murcia-Hernández, J. L. Pedreño-Molina and Alejandro Díaz-Morcillo, "Optimization of microwave cavities and stirrer dimensions to improve the power efficiency in industrial ovens", 2nd Global Conference on Microwave Energy Applications, Long Beach (USA), 2012.
- J. Fayos-Fernández, J. Monzó-Cabrera, **F. J. Clemente-Fernández**, A. Lozano-Guerrero, Rocío Murcia-Hernández, J. L. Pedreño-Molina and Alejandro Díaz-Morcillo, "Evaluation of the heating pattern of a microwave oven as a linear combination of heating patterns of several planar waves", 2nd Global Conference on Microwave Energy Applications, Long Beach (USA), 2012.

- A. Lozano-Guerrero, J. Monzó-Cabrera, **F. J. Clemente-Fernández** and Alejandro Díaz-Morcillo, "Discretization of rotating stirrers positions in microwave ovens to obtain equivalent reflection coefficient models", HES-13 - International Symposium on Heating by Electromagnetic Sources, Padova (Italy), vol. 1, pp. 199-205, 2013.
- **F. J. Clemente-Fernández**, J. Monzó-Cabrera, J. L. Pedreño-Molina and A. Lozano-Guerrero, "Constraints of traditional chokes for use in industrial microwave-heating ovens and alternatives to cope with its issues", HES-13 - International Symposium on Heating by Electromagnetic Sources, Padova (Italy), vol. 1, pp. 531-536, 2013.

6.4.4 Books

- J. Monzó-Cabrera, A. Díaz-Morcillo, J. L. Pedreño-Molina, J. M. Catalá-Civera, A. Lozano-Guerrero and **F. J. Clemente-Fernández**, Aplicaciones industriales del calentamiento asistido por microondas. Spain: Universidad Politécnica de Cartagena, 2009.

6.4.5 Patents

- J. L. Pedreño-Molina, J. Monzó-Cabrera, A. Díaz-Morcillo, A. Lozano-Guerrero and **F. J. Clemente-Fernández**, "Filtro autoconfigurable para hornos microondas de procesado en línea, proceso de filtrado autoconfigurable para hornos de microondas de procesamiento en línea y horno microondas de procesamiento en línea", ES Patent 2334549, Jul. 05, 2010.
- J. Monzó-Cabrera, J. L. Pedreño-Molina, A. Díaz-Morcillo, A. Lozano-Guerrero, **F. J. Clemente-Fernández**, J. Díaz-García, J. M. Baños-Tudela and P. A. Méndez-Hernández, "Filtro multimodo de microondas abierto en tecnología de guía de onda mediante la combinación de postes e iris para hornos de calentamiento por microondas", ES Patent 2337756, Sep. 14, 2011.
- J. Geheniau, J. Monzó-Cabrera, **F. J. Clemente-Fernández** and M. Verhelst, "A compact microwave oven", BE Patent 201200275, Apr. 26, 2012.